A COMPUTATIONAL STUDY ON THE CONTROL OF SELF-SUSTAINED SHOCK OSCILLATION AROUND A SUPERCRITICAL AIRFOIL IN TRANSONIC FLOW

by

Md. Mahbub Alam

A thesis submitted to the Department of Mechanical Engineering in partial fulfillment of the requirements for the degree
of
MASTER OF SCIENCE IN MECHANICAL ENGINEERING

Under the supervision of

Dr. A. B. M. Toufique Hasan

Assistant Professor

Department of Mechanical Engineering
Bangladesh University of Engineering and Technology

BANGLADESH UNIVERSITY OF ENGINEERING AND TECHNOLOGY,
DHAKA – 1000, BANGLADESH

2012

The thesis titled "A Computational Study on the Control of Self-sustained Shock Oscillation around a Supercritical Airfoil in Transonic Flow" Submitted by Md. Mahbub Alam, Roll no: 0409102061P, Session: April, 2009 has been accepted as satisfactory in partial fulfillment of the requirement for the degree of MASTERS OF SCIENCE IN MECHANICAL ENGINEERING on 14/10/2012.

BOARD OF EXAMINARS

1. ______________________________ Chairman

Dr. A. B. M. Toufique Hasan
Assistant Professor
Department of Mechanical Engineering
Bangladesh University of Engineering and Technology (BUET)

2. ______________________________ Member

Dr. Md. Quamrul Islam
Professor
Department of Mechanical Engineering
Bangladesh University of Engineering and Technology (BUET)

3. ______________________________ Member

Dr. Mohammad Ali
Professor
Department of Mechanical Engineering
Bangladesh University of Engineering and Technology (BUET)

4. ______________________________ Member (Ex-officio)

Dr. Md. Ehsan
Professor and Head
Department of Mechanical Engineering
Bangladesh University of Engineering and Technology (BUET)

5. ______________________________ Member (External)

Dr. A. K. M. Sadrul Islam
Professor
Department of Mechanical and Chemical Engineering
Islamic University of Technology (IUT)
Board Bazar, Gazipur.

CANDIDATE'S DECLARATION

It is hereby declared that this thesis or any part of it has not been submitted elsewhere for the award of any degree or diploma or publication.

Md. Mahbub Alam

Student ID: 0409102061

ACKNOWLEDGEMENT

First of all, I want to express my warm gratitude to Almighty God for everything I have achieved so far. I would like to express my profound gratitude to my thesis supervisor, Dr. A. B. M. Toufique Hasan, for his continuous support and guidance throughout this study. I am really grateful to him for giving me the opportunity to learn about computational study and aerodynamics.

My special thanks to Dr. Md. Ehsan Professor and Head of Department of Mechanical Engineering of BUET for the heartiest cooperation throughout the completion of my master’s degree from his department.

I also would like to thank all others who are directly or indirectly related to this thesis by sharing their ideas, suggestions and finally supporting me.

TABLE OF CONTENTS

LIST OF FIGURES viii

LIST OF TABLES xii

SYMBOLIC NOMENCLATURE xiii

ABSTRACT xiv

CHAPTER 1: INTRODUCTION 1

1.1 Transonic Flow 1

1.2 Critical Mach Number 3

1.3 Shock buffet 4

1.4 Supercritical airfoil 5

1.5 Comparison between conventional and supercritical airfoil 7

1.6 NASA SC(2) 0714 airfoil profile 9

1.7 NASA SC(2) 0714 airfoil specification 10

1.8 Objective 11

CHAPTER 2: LITERATURE REVIEW 12

CHAPTER 3: COMPUTATIONAL METHOD 19

3.1 Computational Study 19

3.1.1 Concepts of CFD 20

3.1.2 Techniques for Numerical Discretization 21

3.1.3 Discretization Using The Finite-Volume Method 23

3.2 Turbulence Modeling 25

3.2.1 Classes of turbulence models 25

3.2.2 RANS Equation Averaging 26

3.2.3 *k*-*ω* Model Overview 27

3.2.4 Shear-Stress Transport *k*-*ω* Model Overview 27

3.3 Governing Equations for Turbulence Modeling 28

3.4 Descretization of Flow Domain 33

3.4.1 Create Geometry 33

3.4.2 Meshing 34

3.5 Boundary Condition 37

3.6 Overview of Flow Solver 38

3.6.1 Discretization Scheme 38

3.6.2 Pressure-Velocity Coupling Method 39

3.6.3 Explicit and Under-Relaxation Factors 39

3.6.4 Operating Condition 40

3.6.5 Computational Condition 40

3.6.6 FMG Initialization 41

3.6.7 Monitoring Solution Convergence 41

3.6.8 Time Step Size 41

CHAPTER 4: RESULTS AND DISCUSSION 43
4.1 Validation 43
4.2 Sequential Mach contour: 44
4.2.1 Case: Angle of Attack 2° 44
4.2.2 Case: Angle of Attack 3° 45
4.2.3 Case: Angle of Attack 4° 48
4.2.4 Case: Angle of Attack 5° 51
4.2.5 Case: Angle of Attack 6° 54
4.2.6 Case: Angle of Attack 7° 57
4.3 Lift and Drag Coefficient 61
4.4 Pressure Coefficient Distribution along the Airfoil 64
4.4.1 Case : Angle of Attack 2° 65
4.4.2 Case : Angle of Attack 3° 65
4.4.3 Case : Angle of Attack 4° 67
4.4.4 Case : Angle of Attack 5° 69
4.4.5 Case : Angle of Attack 6° 71
4.4.6 Case : Angle of Attack 7° 73
4.5 Pressure History on Upper Surface of Airfoil 75
4.5.1 Case : Angle of Attack 3° 75
4.5.2 Case : Angle of Attack 4° 78

4.5.3 Case : Angle of Attack 5° 81

4.5.4 Case : Angle of Attack 6° 84

4.5.5 Case : Angle of Attack 7° 87

4.6 Root Mean Square of Pressure Distribution 91

4.7 Shock position 94

4.7.1 Case : Angle of Attack 2° 94

4.7.2 Case : Angle of Attack 3° 95

4.7.3 Case : Angle of Attack 4° 96

4.7.4 Case : Angle of Attack 5° 97

4.7.5 Case : Angle of Attack 6° 98

4.7.6 Case : Angle of Attack 7° 99

4.8 Shock control with bump 100

4.8.1 Mach contour 101

4.8.2 Lift and drag coefficient 105

4.8.3 Pressure coefficient 108

4.8.4 Shock location 109

CHAPTER 5: CONCLUSION AND RECOMMENDATION 110

5.1 Conclusion 110

5.2 Recommendation 112

REFERENCE 113

LIST OF FIGURES

Figure 1.1: Flow development on two dimensional airfoil as M_∞increases beyond M_c 3

Figure 1.2: Flow fields around supercritical and conventional airfoils. 7

Figure 1.3: Profile of NASA SC(2)-0714 supercritical airfoil 9

Figure 1.4: Graph of C_l vs C_d (a) and C_l vs Angle of Attack (b) for different Reynolds number of NASA SC(2) 0714 airfoil. 10

Figure 3.1: Airfoil case grid…………………………………………………..24

Figure 3.2: Airfoil surface with vertex data points 33

Figure 3.3: Far-field boundary around airfoil 33

Figure 3.4: Mesh generation around airfoil 34

Figure 3.5: Grid independence test at 2° and 7° angle of attack for M_∞ = 0.77 35

Figure 3.6: Enlarge view of mesh generation around airfoil 36

Figure 3.7: Time step size sensitivity test for M_∞ = 0.77, α = 3° 42

Figure 4.1: Distribution of pressure coefficient along the airfoil surfaces; (a) M_∞ = 0.72, α = 2.5^o; (b) M_∞ = 0.74, α = 2.0^o and (c) M_∞ = 0.74, α = 3.0^o. 43

Figure 4.2: Contours of Mach number for M_∞= 0.77, α = 2°... 44

Figure 4.3(a): Contours of Mach number (with filled) during one cycle of flow oscillation, for M_∞= 0.77, α = 3°.. 46

Figure 4.3(b): Contours of Mach number (with line) during one cycle of flow oscillation, for M_∞ = 0.77, α = 3°.. 47

Figure 4.4(a): Contours of Mach number (with filled) during one cycle of flow oscillation, for M_∞ = 0.77, α = 4°.. 49

Figure 4.4(b): Contours of Mach number (with line) during one cycle of flow oscillation, for M_∞ = 0.77, α = 4°.. 50

Figure 4.5(a): Contours of Mach number (with filled) during one cycle of flow oscillation, for M_∞= 0.77, α = 5°.. 52
Figure 4.5(b): Contours of Mach number (with line) during one cycle of flow oscillation, for M_∞ = 0.77, α = 5°.. 53
Figure 4.6(a): Contours of Mach number (with filled) during one cycle of flow oscillation, for M_∞= 0.77, α = 6°.. 55
Figure 4.6(b): Contours of Mach number (with line) during one cycle of flow oscillation, for M_∞= 0.77, α = 6°.. 56
Figure 4.7(a): Contours of Mach number (with filled) during one cycle of flow oscillation, for M_∞ = 0.77, α = 7°.. 58
Figure 4.7(b): Contours of Mach number (with line) during one cycle of flow oscillation, for M_∞ = 0.77, α = 7°.. 59
Figure 4.8: Evolution of lift coefficient C_l at M_∞ = 0.77; for (a) α = 2°, (b) α = 3°, (c) α = 4°, (d) α = 5°, (e) α = 6°, (f) α = 7°... 61
Figure 4.9: Evolution of drag coefficient C_d at M_∞ = 0.77; (a) α = 2°, (b) α = 3°, (c) α = 4°, (d) α = 5°, (e) α = 6°, (f) α = 7°.. 62
Figure 4.10: C_p distribution on upper and lower surface of airfoil for M_∞ = 0.77, α = 2°... 65
Figure 4.11: C_p distribution during one cycle of flow oscillation, on upper and lower surface of airfoil for M_∞ = 0.77, α = 3°... 66
Figure 4.12: C_p distribution during one cycle of flow oscillation, on upper and lower surface of airfoil for M_∞= 0.77, α = 4°... 68
Figure 4.13: C_p distribution during one cycle of flow oscillation, on upper and lower surface of airfoil for M_∞ = 0.77, α = 5°... 70

Figure 4.14: C_p distribution during one cycle of flow oscillation, on upper and lower surface of airfoil for M_∞ = 0.77, α = 6°.. 72

Figure 4.15: $C_p$distribution during one cycle of flow oscillation, on upper and lower surface of airfoil for M_∞= 0.77, α = 7°.. 74

Figure 4.16: Non dimensional static pressure time histories at different points on the upper surface of the airfoil for the conditions M_∞= 0.77, α = 3°. 77

Figure 4.17: Non dimensional static pressure time histories at different points on the upper surface of the airfoil for the conditions M_∞= 0.77, α = 4° 80

Figure 4.18: Non dimensional static pressure time histories at different points on the upper surface of the airfoil for the conditions M_∞= 0.77, α = 5° 83

Figure 4.19: Non dimensional static pressure time histories at different points on the upper surface of the airfoil for the conditions M_∞ = 0.77, α = 6°. 86

Figure 4.20: Non dimensional static pressure time histories at different point on the upper surface of the airfoil for the conditions M_∞ = 0.77, α = 7° 89

Figure 4.21: Non-dimensional root mean square of static pressure, $Prms/p_0$ distribution along the airfoil upper surface for different angles of attack and M_∞ = 0.77.. 91

Figure 4.22: Shock wave location along the upper surface for M_∞ = 0.77, α = 2° 94

Figure 4.23: Unsteady shock wave movement during (a) 1st half cycle, (b) 2nd half cycle; of an oscillation along the upper surface for M_∞ = 0.77, α = 3°............................ 95

Figure 4.24: Unsteady shock wave movement during (a) 1st half cycle, (b) 2nd half cycle; of an oscillation along the upper surface for the conditions M_∞ = 0.77, α = 4° 96

Figure 4.25: Unsteady shock wave movement during (a) 1st half cycle, (b) 2nd half cycle; of an oscillation along the upper surface for the conditions M_∞ = 0.77, α =5° 97

Figure 4.26: Unsteady shock wave movement during (a) 1st half cycle, (b) 2nd half cycle; of an oscillation along the upper surface for the conditions $M_\infty = 0.77$, $\alpha = 6°$ 98

Figure 4.27: Unsteady shock wave movement during (a) 1st half cycle, (b) 2nd half cycle; of an oscillation along the upper surface for the conditions $M_\infty = 0.77$, $\alpha = 7°$ 99

Figure 4.28: Bump geometry and shape on airfoil. 100

Figure 4.29: Contours of Mach number with bump for $M_\infty = 0.77$, $\alpha = 3°$. 101

Figure 4.30: Contours of Mach number with bump for $M_\infty= 0.77$, $\alpha = 4°$. 102

Figure 4.31: Contours of Mach number with bump for $M_\infty = 0.77$, $\alpha = 5°$. 103

Figure 4.32: Contours of Mach number with bump for $M_\infty= 0.77$, $\alpha = 6°$. 103

Figure 4.33: Contours of Mach number with bump for $M_\infty = 0.77$, $\alpha = 7°$. 104

Figure 4.34: Evolution of lift coefficient C_l with bump at $M_\infty= .77$; (a) $\alpha = 3°$, (b) $\alpha = 4°$, (c) $\alpha = 5°$, (d) $\alpha = 6°$, (e) $\alpha = 7°$ 105

Figure 4.35: Evolution of drag coefficient C_d with bump at $M_\infty = .77$; (a) $\alpha = 3°$, (b) $\alpha = 4°$, (c) $\alpha = 5°$, (d) $\alpha = 6°$, (e) $\alpha = 7°$. 106

Figure 4.36: C_p distribution on upper and lower surface of airfoil with bump for $M_\infty= 0.77$, $\alpha = 3°$, $\alpha = 4°$, $\alpha = 5°$, $\alpha = 6°$ and $\alpha = 7°$ 108

Figure 4.37: Steady shock wave location on upper surface of airfoil with bump for $M_\infty = 0.77$, $\alpha = 3°$, $\alpha = 4°$, $\alpha = 5°$, $\alpha = 6°$ and $\alpha = 7°$ 109

LIST OF TABLES

Table 3.1: Coordinates of far-field boundary around airfoil... 34

Table 4.1: Comparison of C_l and C_d with different angle of attack for M_∞= 0.77............ 63

Table 4.2: Comparison of frequency of oscillation with different angle of attack for M_∞= 0.77.. 90

Table 4.3: Location and width of bump with different angle of attack forM_∞= 0.77 100

Table 4.4: Comparison of C_l and $C_d$without bump and with bump for different angle of attack at M_∞= 0.77. 107

SYMBOLIC NOMENCLATURE

α:	Angle of Attack
M_∞:	Free Stream Mach Number
C_l:	Lift Coefficient
C_d:	Drag Coefficient
f:	Oscillation Frequency
t:	Time
T:	Time Period
C_p:	Pressure Coefficient
x:	Airfoil chord distance from leading edge
c:	Chord length of the airfoil
P:	Static Pressure
P_0::	Atmospheric Pressure
$Prms$:	Root Mean Square of Pressure
ρ :	Density of air
v_∞:	Free stream air velocity
Re:	Reynolds number
μ:	Absolute viscosity of air
T_∞:	Ambient temperature

ABSTRACT

Transonic flow around supercritical airfoil involves shock induced oscillation at certain free stream Mach number and angle of attack due to the interaction of shock wave with airfoil boundary layer. This interaction consequences fluctuating lift and drag coefficient, aero acoustic noise and vibration, intense drag rise, high cycle fatigue failure (HCF), buffeting and so on. Moreover, the unsteady pressure fluctuations generated by the shock motions are highly undesirable from structural integrity and aircraft maneuverability point of view. The aerodynamic characteristics of the present problem have been solved by numerical computation. A commercial finite volume CFD package has been used for this computation. The computational domain has been discretized into a structured mesh by using a commercial preprocessing tool. The transonic flow around a supercritical airfoil is governed by the unsteady compressible Reynolds-averaged Navier-Stokes equation together with the energy equation. Two additional equations of k-ω SST turbulence model have been included to model the turbulence in the flow field. The results obtained from the numerical computation have been validated with the experimental results. Maintaining same flow parameters computational analysis has been done at free stream Mach number 0.77 and angle of attack from 2° to 7°. Mach contour, lift and drag coefficient, pressure coefficient and pressure history at different points over the airfoil has been captured and analyzed. To suppress the self-excited shock oscillation effectiveness of bump based passive control technique around the airfoil in transonic interval flows has been numerically analyzed and found its effectiveness.

CHAPTER 1

INTRODUCTION

When an aircraft flies at transonic speed range (0.8 < M_∞ < 1.2), airfoil faces shock wave due to the compressibility effect and aerodynamic behavior of air. This phenomenon leads to reduced lift coefficient and imposes overstress on airfoil surface which eventually limits aircraft speed. To delay the shock induced boundary layer separation and to further extend the flight envelope, a special design airfoil was invented - known as supercritical airfoil. At certain range of angle of attack and Mach number, the shock starts to oscillate over the airfoil surface known as Shock Induced Oscillation (SIO). This unsteady phenomenon is also observed in other aeronautical applications such as on turbine cascade, compressor blades, fans, diffusers and so on.

1.1 Transonic Flow

When an airplane is in motion at subsonic speeds, the air is treated as though it was incompressible. As airplane speed increases, however, the air loses its assumed incompressibility and the error in estimating, for example, drag becomes greater and greater.

The Mach number is a measure to indicate whether the aircraft will flow through its assumed incompressibility or not. It is the ratio of the airplane speed to the speed of sound. For Mach numbers less than one is known as subsonic flow, for Mach numbers greater than one, supersonic flow, and for Mach numbers greater than 5, the name is hypersonic flow. Additionally, transonic flow pertains to the range of speeds in which flow patterns change from subsonic to supersonic or vice versa, about Mach 0.8 to 1.2. Transonic flow presents a special problem area as neither equations describing subsonic flow nor those describing supersonic flow may be accurately applied to the regime. The sudden loss of lift, increases in drag and rapid movement in centre of pressure are similar in flight to those experienced at the stall and this flight regime became known as the shock stall.

To appreciate why the aerofoil characteristics begin to change so dramatically we recall the properties of shock waves the first appearance of which signals the start of the change. Across the shock wave, which is the only mechanism for a finite pressure increase in supersonic flow, the pressure rise is large and sudden. More over the shock wave is a process accompanied by an entropy change which manifests itself as an immediate rise in drag, i.e. an irreversible conversion of mechanical energy to heat (which is dissipated) takes place and sustaining this loss results in the drag. The drag increase is directly related to the strengths of the shock waves which in turn depend on the magnitude of the supersonic regions ahead. Another contribution to the drag will occur if the boundary layer at the foot of the shock separates as a consequence of accommodating the sudden pressure rise.

The question arises as to whether one may impart the ability to fly at near-sonic velocities with the same available engine thrust before encountering large wave drag. There are a number of ways of delaying the transonic wave drag rise. These include

(1) Use of thin airfoils;

(2) Use of a forward or backward swept wing;

(3) Low-aspect-ratio wing;

(4) Removal of boundary layer and vortex generators; and

(5) Supercritical and area-rule technology.

These airfoils have critical Mach numbers very close to one (hence the term supercritical) thereby delaying and reducing the large increase in drag due to wave drag.

1.2 Critical Mach Number

When the air flows past a body, or vice versa, e.g. a symmetrical aerofoil section at low incidence, the local airspeed adjacent to the surface just outside the boundary layer is higher or lower than the free-stream speed depending on whether the local static pressure is less or greater than the ambient. In such a situation, the value of the velocity somewhere on the aerofoil exceeds that of the free stream. Thus the free stream flow speed rises the Mach number at a point somewhere adjacent to the surface reaches sonic conditions before the free stream. The value of the free-stream Mach number *(M_∞),* at which the flow somewhere on the surface first reaches M_∞=1 is called the 'critical Much number' (figure 1.1). Below that critical Mach number the flow is subsonic throughout.

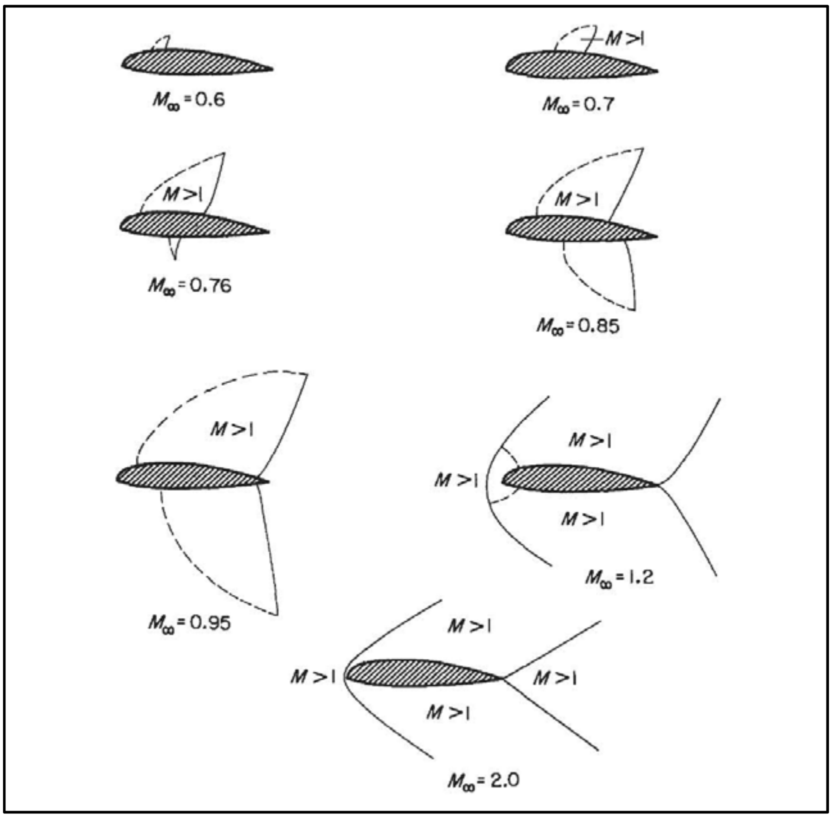

Figure 1.1: Flow development on two dimensional airfoil as M_∞ increases beyond M_c

As M_∞ is increased progressively beyond M_∞ a limited region in which the flow is supersonic develops from the point where the flow first became sonic and grows outwards and downstream, terminating in a shock wave that is at first approximately normal to the surface. As M_∞ increases the shock wave becomes stronger, longer and moves rearwards. At some stage, at a value of $M_\infty > M_c$, the velocity somewhere on the lower surface approaches and passes the sonic value, a supersonic region terminating in a shock wave appears on the lower surface, and that too grows stronger and moves back as the lower supersonic region increases.

Eventually at a value of M_∞ close to unity the upper and lower shock waves reach the trailing edge. In their rearward movement the shock waves approach the trailing edge in general at different rates, the lower typically starting later and ahead of the upper, but moving more rapidly and overtaking the upper before they reach the trailing edge. When the free-stream Mach number has reached unity a bow shockwave appears at a small stand-off distance from the rounded leading edge. For higher Mach numbers the extremes of the bow and trailing waves incline rearwards to approach the Mach angle.

1.3 Shock buffet

At transonic and supersonic speeds, there is a substantial increase in the total drag of the airplane due to fundamental changes in the pressure distribution. This drag increase encountered at these high speeds is called ‘wave drag’. For transonic flow, the wave drag increase is greater than would be estimated from a loss of energy through the shock. In fact, the shock wave interacts with the boundary layer so that a separation of the boundary layer occurs immediately behind the shock. This condition accounts for a large increase in drag that is known as shock-induced (boundary-layer) separation.

Often, in transonic flow, the flow is unsteady, and the shock waves on the body surface may jump back and forth along the surface, thus disrupting and separating the flow over the wing surface. This sends pulsing, unsteady flow back to the tail surfaces of the airplane. The resulting phenomena is known as buffeting and vibration of both wing and tail controls.

The flow physics regarding buffeting is that the movement of the shock leads to the formation of pressure waves which propagate downstream within the separated flow region. On reaching the trailing edge, the disturbance generates upstream-moving waves, which interact with the shock wave and impart energy to maintain the limit cycle. Unlike the downstream waves, the upstream-moving waves travel in the region outside the separated boundary layer.

1.4 Supercritical airfoil

An airfoil considered unconventional when tested in the early 1970s by NASA at the Dryden Flight Research Center is now universally recognized by the aviation industry as a wing design that increases flying efficiency and helps lower fuel costs. Called the supercritical airfoil, the design has led to development of the supercritical wings (SCW) now used worldwide on business jets, airliners and transports, and numerous military aircraft.

A concerted effort within the National Aeronautics and Space Administration (NASA) during the 1960's and 1970's was directed toward developing practical airfoils with two-dimensional transonic turbulent flow and improved drag divergence Mach numbers while retaining acceptable low-speed maximum lift and stall characteristics and focused on a concept to develop the supercritical airfoil.

The early phase of this effort was successful in significantly extending drag-rise Mach numbers beyond those of conventional airfoils such as the National Advisory Committee for

Aeronautics (NACA) 6-series airfoils. These early supercritical airfoils (denoted by the SC(phase 1) prefix), however, experienced a gradual increase in drag at Mach numbers just preceding drag divergence (referred to as drag creep). This gradual buildup of drag was largely associated with an intermediate off-design second velocity peak (an acceleration of the flow over the rear upper-surface portion of the airfoil just before the final recompression at the trailing edge) and relatively weak shock waves above the upper surface.

Improvements to these early, phase 1 airfoils resulted in airfoils with significantly reduced drag creep characteristics. These early, phase 1airfoils and the improved phase 1 airfoils were developed before adequate theoretical analysis codes were available and resulted from iterative contour modifications during wind-tunnel testing. The process consisted of evaluating experimental pressure distributions at design and off-design conditions and physically altering the airfoil profiles to yield the best drag characteristics over a range of experimental test conditions. The insight gained and the design guidelines that were recognized during these early phase 1 investigations, together with transonic, viscous, airfoil analysis codes developed during the same time period, resulted in the design of a matrix of family-related supercritical airfoils (denoted by the SC(phase 2) prefix).

1.5 Comparison between conventional and supercritical airfoil

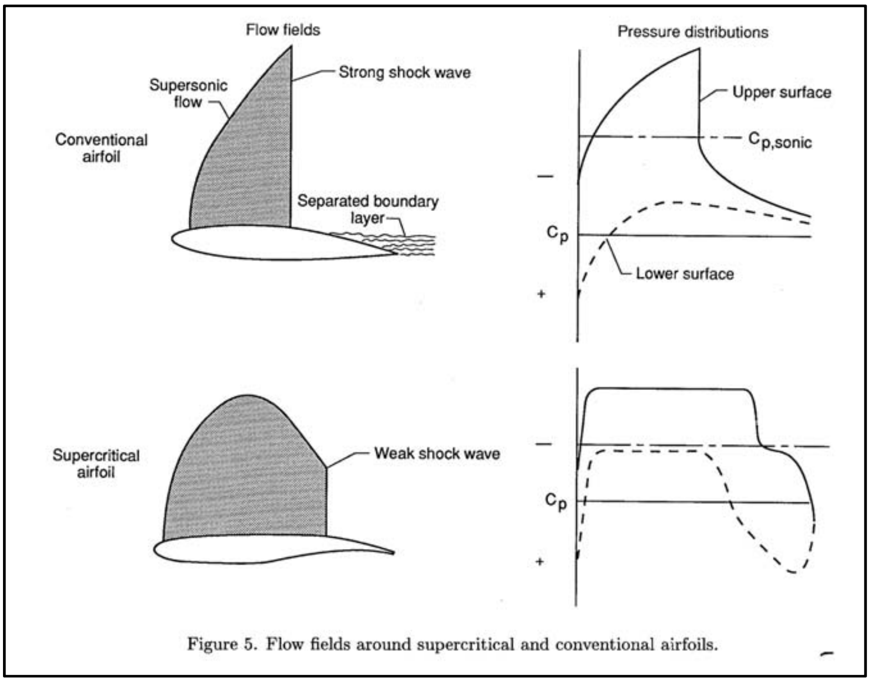

Figure 1.2: Flow fields around supercritical and conventional airfoils.

Conventional wings are rounded on top and flat on the bottom. The supercritical wing is flatter on the top, rounded on the bottom, and the upper trailing edge is accented with a downward curve to restore lift lost by flattening the upper surface. At speeds in the transonic range just below and just above the speed of sound the supercritical wing delays the formation of the supersonic shock wave on the upper wing surface and reduces its strength, allowing the aircraft to fly faster with less effort.

A comparison of supercritical flow phenomena for a conventional airfoil and the NASA supercritical airfoils shown in figure 1.2 As an airfoil approaches the speed of sound, the velocities on the upper surface become supersonic because of the accelerated flow over the upper surface, and there is a local field of supersonic flow extending vertically from the airfoil and immersed in the general subsonic field. On conventional airfoils this pocket of accelerating supersonic flow is terminated near mid-chord by a more or less pronounced shock wave with attendant wave losses. This shock wave is followed immediately by a decelerating flow to the trailing edge. The pressure rise through the shock wave may, when superimposed on the adverse pressure gradient at the trailing edge, cause separation of the boundary layer with further increases in drag as well as buffeting and stability problems.

The surface pressure distribution and flow field shown at the bottom of figure 1.2 are representative of those obtained for NASA supercritical airfoils. The upper-surface pressure and related velocity distributions are characterized by a shock location significantly aft of the mid-chord, an approximately uniform supersonic velocity from about 5 percent chord to the shock, a plateau in the pressure distribution downstream of the shock, a relatively steep pressure recovery on the extreme rearward region, and a trailing-edge pressure slightly more positive than ambient pressure. The lower surface has roughly constant negative pressure coefficients corresponding to subcritical velocities over the forward region and a rapid increase in pressure rearward of the mid-chord to a substantially positive pressure forward of the trailing edge.

To give some idea of the practical benefit of the supercritical airfoil, US Air Force and NASA researchers under the auspices of the Transonic Aircraft Technology (TACT) program modified a basic F-111 bomber and replaced the existing NACA 64-210 wing airfoil with a supercritical shape of equal thickness. In so doing, they managed to increase the drag divergence Mach number by 16%, from Mach 0.76 to Mach 0.88. This example illustrates how significant the use of supercritical airfoils can be in improving the performance of aircraft cruising in the transonic regime

1.6 NASA SC(2) 0714 airfoil profile

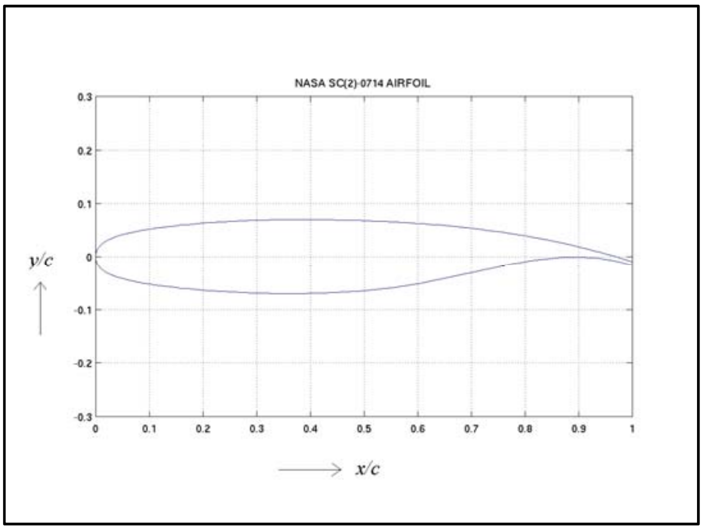

Figure 1.3: Profile of NASA SC(2)-0714 supercritical airfoil

Figure 1.3 shows a NASA SC(2)–0714 Supercritical airfoil profile which has a flat-on-top "upside-down" look. As air moves across the top of a supercritical airfoil it does not speed up nearly as much as over a curved upper surface. This delays the onset of the shockwave and also reduces aerodynamic drag associated with boundary layer separation. Lift that is lost with less curvature on the upper surface of the wing is regained by adding more curvature to the upper trailing edge.

The disadvantage of this approach is that aft-loaded wings shift the center of lift back which necessitates moving the wings forward. This design tradeoff results in larger pitching moments, the need for larger and heavier control surfaces, and the need for stronger and heavier wing structures.

1.7 NASA SC(2) 0714 airfoil specification

Thickness	:	14.0% c
Camber	:	1.5% c
Trailing edge angle	:	3.9^{o}
Lower flatness	:	1.9% c
Leading edge radius	:	3.0% c
Max C_l	:	1.435
Max C_l angle	:	15°
Max L/D	:	25.804
Max L/D angle	:	0°
Stall angle	:	3.5°
Zero-lift angle	:	-5.0°

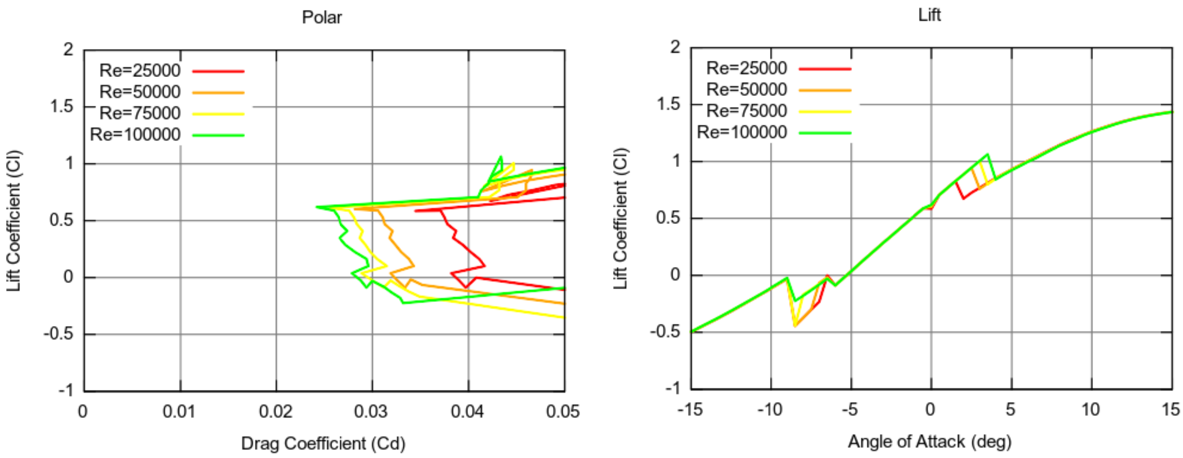

(a) (b)

Figure 1.4: Graph of C_l vs C_d (a) and C_l vs Angle of Attack (b) for different Reynolds number of NASA SC(2) 0714 airfoil. (Source: www.worldof krauss.com/foils/270).

1.8 Objective

The specific objectives and outcome of the research work are as follows:

(a) To develop a computational model to predict the self-sustained shock oscillation around a supercritical airfoil NASA SC(2)-0714 in transonic flows.

(b) To investigate the self-sustained shock oscillation at varying angles of attack from 2° to 7°.

(c) To predict the suppression of self-excited shock oscillation around the supercritical airfoil using bump.

The goal of the present research is to evaluate the bump based passive means for the control of self-sustained shock oscillation around a supercritical airfoil through numerical computation.

CHAPTER 2

LITERATURE REVIEW

In case of high speed aerodynamics such as in transonic and supersonic flows; unsteady interaction of shock waves with boundary layers becomes complex and generates the self sustained shock oscillation in the flow field [1-2]. Attempts have been made to formulate a model to predict the unsteady shock motion, but so far a satisfactory explanation of the mechanism of self-sustained shock oscillation and a method to estimate the frequency about which the shock wave oscillates are still lacking. A mechanism to estimate frequency of self-sustained shock motion observed in transonic shock boundary-layer interaction has been described in [3] where is was showed that the time it takes a disturbance to propagate from the shock to the trailing edge plus the additional time it takes for an upstream traveling wave generated at the trailing edge to reach the shock agree quite closely with the period of shock oscillation measured from unsteady force spectra beyond the buffet onset boundary.

Shock wave/boundary layer interactions (SBLI) can significantly affect the performances of various high-speed aircraft, such as wings of transport and inlets of military jets. Two primary applications include reducing drag penalties incurred by either operating an aircraft at increased speed (increase drag divergent Mach number), or flying at a higher lift coefficient without buffeting [4-5] (increase buffeting boundary).

Periodic shock motions on airfoils at transonic flow conditions had been observed experimentally [6-8] for more than a decade. They have also been detected from numerical solutions of the Navier-Stokes equations [9] and recently by an unsteady viscous-inviscid interaction method [10]. For a limited range of Mach number buffet onset was well-studied for the shock buffet of 18% thick circular arc airfoil. The studies of Gilan [11] and Rumsey et at. [12] on 18% thick circular arc airfoil and that of McDevitt et al. [13] on 14% thick-circular arc non-lifting airfoil are good examples of this phenomenon. Buffet onset for NACA 0012 has been simulated well by Singh [14] and it is seen to be in good agreement with the experimental data.

Steady interactive boundary layer and Navier-Stokes solutions of the NACA 0012 airfoil have been previously published [15-16] and compared with the steady data of [17]. Shock buffet interactive boundary layer computations for the same airfoil have been shown in previous publications with a time accurate integral boundary layer and the classical transonic small disturbance (TSD) equation [18] and a TSD using an Euler-like stream wise flux and a steady integral boundary layer [19]. The interactive boundary layer approach has given shock buffet onset for the NACA 0012 airfoil that compares well with the onset of [20]. Ref [19 and 21] encourages one to pursue further investigation with this method. Although it is generally accepted that the boundary layer assumption is violated in many problems of this type, the interactive boundary layer method does make possible a broader study of the problem due to its efficiency. That is done by interactive boundary layer method using the CAP-TSD (Computational Aero elasticity Program) potential code with a modified stream wise flux [22] and an unsteady compressible boundary layer solved in finite difference form. Results are presented for several variations of the k-ω turbulence model.

Recently, numerical prediction of shock induced oscillations (SIO) over OAT15A and BAC3-11 airfoils was performed [23-24]. Compared to the non-lifting and conventional airfoils, the study of lifting supercritical airfoils is at a lesser extent. An attempt on the buffeting flow over BGK NO. 1 supercritical airfoil was taken in recent past [25]. The shear stress transport form of the model is used to compute details of the shock buffet of the NASA SC(2)-0714 airfoil [26]. Comparisons with the experimental shock buffet data at high Reynolds numbers of [26] are shown at several Reynolds numbers; this represents the first numerical study of the effect of turbulent boundary layer Reynolds number scaling on shock buffet onset. Previous unsteady thin-layer Navier-Stokes shock buffet results for a conventional and supercritical airfoil using the Baldwin-Lomax model and flux differences using artificial smoothing were shown by other authors in references [27-28]. Thin-layer Navier-Stokes computations are shown [29] using the Menter k-ω shear stress transport (SST) and the Spalart-Allmaras (SA) turbulence models. Thin-layer Navier-Stokes results with a steady separated shock are shown that compare well with the steady interactive boundary layer results; these are followed with thin-layer Navier-Stokes computations in the shock buffet onset regions of the two airfoils.

Rivers and Walls [30] determines the capability of a state-of-the-art, upwind, thin-layer Navier-Stokes flow solver to predict steady-state Reynolds number effects for flow over a two- dimensional NASA SC(2)-0714 supercritical airfoil. The study demonstrated that the computational solutions could be significantly influenced by the computational treatment of the trailing-edge region of a blunt trailing- edge airfoil. The study also demonstrated the necessity of matching computational and experimental flow conditions. To order to capture turbulence modeling correctly, previous research like [31−33] has revealed that the accuracy of the numerical calculations is mainly dictated by the accuracy of the turbulence model. Almost all of the simulations are concerned with two-dimensional calculations. A complete study (turbulence models, numerical schemes) of URANS calculations concerning the OAT15A supercritical airfoil has been recently performed by Brunet [34]. His study shows that URANS calculations are able to predict quite well the main properties of the flow (rms, pressure distribution) but often need to increase the angle of attack in the calculation compared to the experimental value. And DES has been developed to handle massive separated flows that rapidly develop strong instabilities associated with large-scale structures. Nevertheless, not very many publications [35] are devoted to DES of thin-layer separation, especially when shock/boundary layer interactions occur.[36]. Deck [37] assessed the capability of DES to capture the buffet phenomenon at the experimental angle of attack and analyze unsteady features of the flow to discuss the mechanisms of buffet onset.

Moreover, the control of the self-sustained shock oscillation around an airfoil is getting intense interest for the last several years. Stanewsky [38] widely provided various conventional and novel means of boundary layer and flow control applied to moderate-to-large aspect ratio wings, delta wings and bodies with the specific objectives of drag reduction, lift enhancement, separation suppression and the improvement of air-vehicle control effectiveness. In principle, flow control techniques have one or more of the following objectives: suppression of flow breakdown and buffet, reduction of viscous drag and wave drag. Control techniques which fulfill all of these objectives have not yet been developed. As a result, many active and passive control techniques are being investigated. Passive and active shock and boundary layer control were thoroughly investigated in the EU-projects EUROSHOCK I and II-Drag reduction by shock and boundary layer control [39]. Active shock control using suction, blowing as well as zero-mass flux oscillatory blowing are introduced in aerodynamic applications [40-41]. Djayapertapa and Allen [42] showed a flight control system during trailing edge flap motion to actively control during shock oscillation and shown that active control is still effective when there is free-play in the control surface hinge. Qin et al. [43] shows the effectiveness of a number of active devices for the control of shock waves on transonic aerofoils using numerical solutions of the Reynolds-averaged Navier-Stokes equations. The numerical simulations highlight the benefits and drawbacks of the various control devices for transonic aerodynamic performance and identify the key design parameters for optimization. Currently, micro-blowing as flow control technique is proposed [44].

Beyond these, there are some passive control techniques which are economically more viable such as local geometrical changes of the aerofoil profile by a local bump near the foot of the shock termed as shock control bump, micro ramp and so on [45-47]. Other passive control techniques are by implementing a porous surface at the foot of the shock [48-49], and local slots and grooves [50].

The shock control bump aims to replace the normal transonic shock with near isentropic compression or break it up into multiple weaker shocks, e.g. a λ-shock structure, which significantly weakens the shock strength and hence the wave drag. A number of studies have shown that appropriately designed two-dimensional bumps are very effective in reducing wave drag, and can substantially improve aircraft performance, as investigated. However, two-dimensional bumps are only effective over a narrow operational range. This drawback could be overcome by the introduction of an adaptive device [51-52] but this would imply a further increase of system weight that might erode the benefit of the potential drag reduction. Thus, alternative shock control devices, which are potentially beneficial over a wider range of operating conditions have been proposed, e.g. slots, grooves and three-dimensional bumps [53-54] have investigated the aerodynamic performance of an array of three-dimensional bumps placed upon a constant section wing with a natural laminar flow aerofoil profile (RAE5243). Their preliminary results suggested that it is possible for appropriately designed three-dimensional bumps to be as effective as two-dimensional bumps while also overcoming the limitations of two-dimensional bumps under off design conditions Parallel experimental studies by Holden et al. [53] on various three-dimensional bump shapes installed on the wind tunnel wall have clearly demonstrated the ability of three-dimensional bumps to bifurcate a shock wave. A fully 3D design of a contour bump for a transonic wing by RANS computations was performed with a cooperation between DLR, ONERA and Airbus Germany [55].The bump design was verified by the wind tunnel tests on a half model in the ONERA S2MA facilities.Significant effect of bump location and height on RAE5243 aerofoil has been numerically investigated in [56].

Yun et al. [57] investigate supercritical Airfoil RAE2822 superimposed with different shock control bumps under the transonic conditions Based on improving the airfoil's lift-drag ratio, the study shows that, (1) the best bump crest position is at the position close to 50% of bump chord, which is almost independent of free stream or pre-shock Mach numbers, but the bump height is highly coupled with the crest position, which means that the higher the bump is, the more obviously the crest position affects the airfoil lift-drag ratio, and it becomes more evident with the increase of free stream or pre-shock Mach numbers; (2) in case that the lift-drag ratio of airfoil with bump is higher than basic airfoil, almost all the optimum distances between bump crest and shock wave are close to 30% of bump chord; (3) almost all the lift-drag ratios of airfoil with bump increase as bump chord length increases, of which this trend becomes more evident as bump height increases; (4) with the increase of the bump height, almost all the lift-drag ratios of airfoil with bump decrease at low free stream or pre-shock Mach numbers. When the Mach numbers are higher, the lift-drag ratio of airfoil increases as the increase of the bump height, and particularly, the trend tends to be visible when the Mach numbers are at a high level.

For most modern large aircrafts, the supercritical wing with high aspect ratio is widely used. The flow structure of the most area on the wing (far away from the wing tip and root) is quite similar to typical 2D airfoil. Therefore this paper focuses on the supercritical airfoil and its parameter variations under different free stream conditions. Two dimensional wind tunnel experimental data involving NASA SC(2)-0714 supercritical airfoils with steady and pitching conditions were presented in [26] by Bartels and Edwards. The experiments were carried out at NASA Langley 0.3-Meter Transonic Cryogenic Tunnel where it was promising to produce shock buffet behavior on the airfoil and store them.

The general objective of the present research is computational study to investigate the self-sustained shock oscillation around a supercritical airfoil NASA SC(2)-0714 using Shear-

Stress Transport k-ω Model. Further, to implement a bump over the shock foot region as a passive means of flow control device. The transonic flows around a supercritical airfoil using this passive means will be investigated through numerical computation.

CHAPTER 3

COMPUTATIONAL METHOD

3.1 Computational Study

The equations of fluid dynamics which have been known for over a century are solvable for only a limited number of flows. The known solutions are extremely useful in helping to understand fluid flow but rarely can they be used directly in engineering analysis or design. The engineer has traditionally been forced to use other approaches.

In the most common approach, simplifications of the equations are used. These are usually based on a combination of approximations and dimensional analysis; empirical input is almost always required. In fluid flow analysis, there may require several dimensionless parameters for their specification and it may be impossible to set up an experiment which correctly scales the actual flow.

In other cases, experiments are very difficult if not impossible. For example, the measuring equipment might disturb the flow or the flow may be inaccessible. As technological improvement and competition require more careful optimization of designs or, when new high technology applications demand prediction of flows for which the database is insufficient, experimental development may be too costly and time consuming. Finding a reasonable alternative is essential.

An alternative method came with the birth of electronic computers. Although many of the key ideas for numerical solution methods for partial differential equations were established more than a century ago, they were of little use before computers appeared. Once the power of computers had been recognized, interest in numerical techniques increased dramatically.

3.1.1 Concepts of CFD

Solution of the equations of fluid dynamics on computers has become so important that it now occupies the attention of perhaps all researchers in fluid mechanics. The field is known as Computational Fluid Dynamics (CFD). The ultimate goal of the field of computational fluid dynamics (CFD) is to understand the physical events that occur in the flow of fluids around and within designated objects. These events are related to the action and interaction of phenomena such as dissipation, diffusion, convection, shock waves, slip surfaces, boundary layers and turbulence.

CFD provides numerical approximation to the equations that govern fluid motion. Application of the CFD to analyze a fluid problem requires the following steps. First, the mathematical equations describing the fluid flow are written. These are usually a set of partial differential equations. These equations are then discretized to produce a numerical analogue of the equations. The domain is then divided into small grids or elements. Finally, the initial conditions and the boundary conditions of the specific problem are used to solve these equations. The solution method can be direct or iterative. In addition, certain control parameters are used to control the convergence, stability, and accuracy of the method.

3.1.2 Techniques for Numerical Discretization

In order to solve the governing equations of the fluid motion, first their numerical analogue must be generated. This is done by a process referred to as discretization. In the discretization process, each term within the partial differential equation describing the flow is written in such a manner that the computer can be programmed to calculate. There are various techniques for numerical discretization. Here we will introduce three of the most commonly used techniques, namely:

(1) The finite difference method,

(2) The finite element method and

(3) The finite volume method.

Spectral methods are also used in CFD, method of generating a numerical analog of a differential equation is by using fourier series or series of Chebyshev polynomials to approximate the unknown functions. However, most commercial CFD codes use the finite-volume or finite-element methods which are better suited for modeling flow past complex geometries.

Broadly, the strategy of CFD is to replace the continuous problem domain with a discrete domain using a grid. In the continuous domain, each flow variable is defined at every point in the domain. For instance, the pressure p in the continuous 1D domain shown in the figure below would be given as

$$p = p(x),\ 0 < x < 1$$

In the discrete domain, each flow variable is defined only at the grid points. So, in the discrete domain shown below, the pressure would be defined only at the N grid points.

$$pi = p(xi),\ i = 1, 2, \ldots, N$$

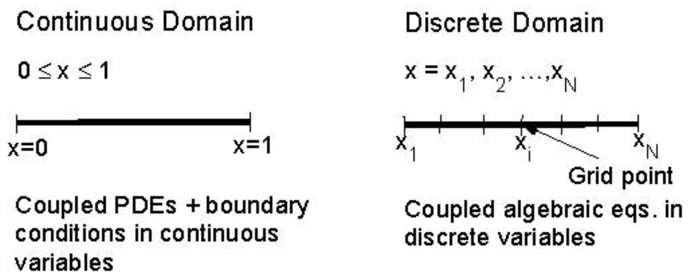

In a CFD solution, one would directly solve for the relevant flow variables only at the grid points. The values at other locations are determined by interpolating the values at the grid points. The governing partial differential equations and boundary conditions are defined in terms of the continuous variables p, V etc. One can approximate these in the discrete domain in terms of the discrete variables p_i, V_i etc. The discrete system is a large set of coupled, algebraic equations in the discrete variables. Setting up the discrete system and solving it (which is a matrix inversion problem) involves a very large number of repetitive calculations and is done by the digital computer. This idea can be extended to any general problem domain.

3.1.3 Discretization Using The Finite-Volume Method

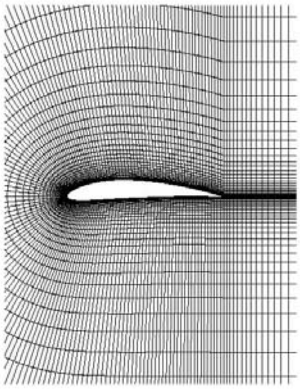

Figure 3.1: Airfoil case grid

The above figure (figure 3.1) shows the grid used for solving the flow over an airfoil. Looking closely at the airfoil grid, it is seen that it consists of quadrilaterals. In the finite-volume method, such a quadrilateral is commonly referred to as a "cell" and a grid point as a "node". In 2D, one could also have triangular cells. In 3D, cells are usually hexahedral, tetrahedral, or prisms. In the finite-volume approach, the integral form of the conservation equations are applied to the control volume defined by a cell to get the discrete equations for the cell. The integral form of the continuity equation for steady, incompressible flow is

$$\int_S \vec{V}.n'dS = 0 \tag{1}$$

The integration is over the surface S of the control volume and n' is the outward normal at the surface. Physically, this equation means that the net volume flow into the control volume is zero. Consider the rectangular cell shown below.

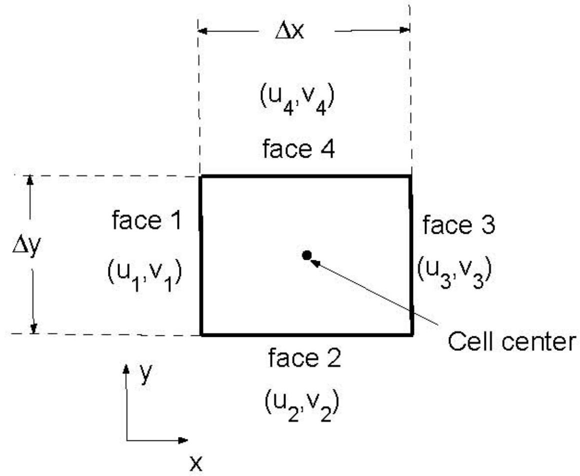

The velocity at face i is taken to be $V_i = u_i \hat{i} + v_i \hat{j}$. Applying the mass conservation equation (1) to the control volume defined by the cell gives

$$u_1\Delta y - v_2\Delta x + u_3\Delta y + v_4\Delta x = 0$$

This is the discrete form of the continuity equation for the cell. It is equivalent to summing up the net mass flow into the control volume and setting it to zero. So it ensures that the net mass flow into the cell is zero i.e. that mass is conserved for the cell. Usually the values at the cell centers are stored. The face values u_1, v_2 etc. are obtained by suitably interpolating the cell-center values at adjacent cells.

Similarly, one can obtain discrete equations for the conservation of momentum and energy for the cell. One can readily extend these ideas to any general cell shape in 2D or 3D and any conservation equation.

3.2 Turbulence Modeling

Turbulence modeling is a key issue in most CFD simulations. Virtually all fluid dynamics engineering applications are turbulent and hence require a turbulence model.

3.2.1 Classes of turbulence models

Nowadays turbulent flows may be computed using several different approaches. Either by solving the Reynolds-averaged Navier-Stokes equations with suitable models for turbulent quantities or by computing them directly. The main approaches are summarized below.

(1) RANS-based models

(A). Linear eddy-viscosity models

(I) Algebraic models

(II) One equation models

(III) Two equation models

(A). k-ϵ models

1. Standard k-ϵ models

2. Realisable k-ϵ models

3. RNG k-ϵ models

4. Near-wall treatment

(B). k-ω models

1. Wilcox's k-ω models

2. Wilcox's modified k-ω models

3. SST k-ω model

4. Near-wall treatment

(B). Non-linear eddy viscosity models and algebraic stress models

(C). Reynolds stress transport models

(2). Large eddy simulations (LES)

(3). Detached eddy simulations (DES) and other hybrid models

(4). Direct numerical simulations (DNS)

3.2.2 RANS Equation Averaging

In Reynolds averaging, the solution variables in the instantaneous (exact) Navier-Stokes equations are decomposed into the mean (ensemble-averaged or time-averaged) and fluctuating components. For the velocity components:

$$u_i = \overline{u_i} + u'_i$$

where $\overline{u_i}$ and u'_i are the mean and fluctuating velocity components (i = 1; 2; 3).Likewise, for pressure and other scalar quantities:

$$\varphi = \bar{\varphi} + \varphi'$$

Where φ denotes a scalar such as pressure, energy, or species concentration.Substituting expressions of this form for the flow variables into the instantaneous continuity and momentum equations and taking a time (or ensemble) average (and dropping the overbear on the mean velocity, $\overline{u}$yields the ensemble-averaged momentum equations.

They can be written in Cartesian tensor form as:

$$\frac{\delta\rho}{\delta t} + \frac{\delta}{\delta x_i}(\rho u_i) = 0 \ldots\ldots\ldots\ldots\ldots\ldots\ldots\ldots\ldots\ldots\ldots\ldots\ldots\ldots\ldots\ldots\ldots\ldots\ldots\ldots\ldots\ldots\ldots, \ldots\ldots\ldots (1)$$

$$\frac{\delta}{\delta t}(\rho u_i) + \frac{\delta}{\delta x_j}(\rho u_i u_j) = -\frac{\delta p}{\delta x_j} + \frac{\delta}{\delta x_j}\left[\mu\left(\frac{\delta u_i}{\delta x_j} + \frac{\delta u_j}{\delta x_i} - \frac{2}{3}\partial_{ij}\frac{\delta u_l}{\delta x_l}\right)\right] + \frac{\delta}{\delta x_j}\left(-\rho\overline{u'_i u'_j}\right) \ldots\ldots (2)$$

Above equations are called Reynolds-averaged Navier-Stokes (RANS) equations. They have the same general form as the instantaneous Navier-Stokes equations, with the velocities and other solution variables now representing ensemble-averaged (or time-averaged) values. Additional terms now appear that represent the effects of turbulence. These Reynolds stresses, $-\rho\overline{u'_i u'_j}$ must be modeled in order to close Equation (2).

3.2.3 *k-ω* Model Overview

The *k-ω* model is one of the most commonly used turbulence models. It is a two equation model that means, it includes two extra transport equations to represent the turbulent properties of the flow. This allows a two equation model to account for history effects like convection and diffusion of turbulent energy.

The first transported variable is turbulent kinetic energy, *k*. The second transported variable in this case is the specific dissipation ,*ω*. It is the variable that determines the scale of the turbulence, whereas the first variable ,*k.* determines the energy in the turbulence.

3.2.4 Shear-Stress Transport *k-ω* Model Overview

The shear-stress transport (SST) *k-ω* model was developed by Menter to effectively blend the robust and accurate formulation of the *k-ω* model in the near-wall region with the free-stream independence of the *k-ω* model in the far field. To achieve this, the *k-ϵ* model is converted into a *k-ω* formulation. The SST *k-ω* model is similar to the standard *k-ω* model, but includes the following refinements:

- The standard *k-ω* model and the transformed *k-ω* model are both multiplied by a blending function and both models are added together. The blending function is designed to be one in the near-wall region, which activates the standard *k-ω* model, and zero away from the surface, which activates the transformed *k-ϵ* model.

- The SST model incorporates a damped cross-diffusion derivative term in the ω equation.
- The definition of the turbulent viscosity is modified to account for the transport of the turbulent shear stress.
- The modeling constants are different.

These features make the SST *k-ω* model more accurate and reliable for a wider class of flows (e.g., adverse pressure gradient flows, airfoils, transonic shock waves) than the standard *k-ω* model. Other modifications include the addition of a cross-diffusion term in the ω equation and a blending function to ensure that the model equations behave appropriately in both the near-wall and far field zones.

3.3 Governing Equations for Turbulence Modeling

The flow in this study is considered to be viscous, compressible, turbulent and unsteady. Governing equations for the present numerical simulations are the conservation of mass, conservation of momentum and energy equations written in 2-D coordinate system. Two additional transport equations of *k-ω* SST (Shear Stress Transport) turbulence model are included to model the turbulence in the flow field. The governing equation can be written in the following vector form:

$$\frac{\partial \boldsymbol{U}}{\partial t} + \frac{\partial \boldsymbol{E}}{\partial x} + \frac{\partial \boldsymbol{F}}{\partial y} = \frac{\partial \boldsymbol{R}}{\partial x} + \frac{\partial \boldsymbol{S}}{\partial y} + \boldsymbol{H} \tag{1}$$

Here $\boldsymbol{U}$is the conservative flux vector. $\boldsymbol{E}$ and $\boldsymbol{F}$ are the inviscid flux vectors and $\boldsymbol{R}$ and $\boldsymbol{S}$ are the viscous flux vectors in the x and y directions, respectively. $\boldsymbol{H}$ is the source terms corresponding to turbulence. The flux vector and the inviscid flux terms are:

$$\boldsymbol{U} = \begin{bmatrix} \rho \\ \rho u \\ \rho v \\ E_t \\ \rho k \\ \rho\omega \end{bmatrix}, \boldsymbol{E} = \begin{bmatrix} \rho u \\ \rho u^2 + P \\ \rho uv \\ u(E_t + P) \\ \rho uk \\ \rho u\omega \end{bmatrix}, \boldsymbol{F} = \begin{bmatrix} \rho v \\ \rho uv \\ \rho v^2 + P \\ v(E_t + P) \\ \rho uk \\ \rho v\omega \end{bmatrix} \tag{2}$$

Here, $E_t$is the total energy, and it can be expressed as:

$$E_t = \rho C_P T + \frac{1}{2}\rho(u^2 + v^2) \tag{3}$$

In above equations, $\rho$is the density, C_P is the specific heat, T is the temperature, u- and v- are the velocity components in x- and y- directions, respectively. k is turbulence kinetic energy and ω is specific dissipation rate.P is the pressure and it is assumed to follow the ideal gas equation. The viscous term in Eq. (1) are:

$$\boldsymbol{R} = \begin{bmatrix} 0 \\ \tau_{xx} \\ \tau_{xy} \\ \alpha \\ \left(\mu + \frac{\mu_t}{\sigma_k}\right)\frac{\partial k}{\partial x} \\ \left(\mu + \frac{\mu_t}{\sigma_\omega}\right)\frac{\partial \omega}{\partial x} \end{bmatrix}, \boldsymbol{S} = \begin{bmatrix} 0 \\ \tau_{xy} \\ \tau_{yy} \\ \beta \\ \left(\mu + \frac{\mu_t}{\sigma_k}\right)\frac{\partial k}{\partial y} \\ \left(\mu + \frac{\mu_t}{\sigma_\omega}\right)\frac{\partial \omega}{\partial y} \end{bmatrix} \tag{4}$$

Where

$$\alpha = u\tau_{xx} + v\tau_{xy} - q_x \tag{5}$$

$$\beta = u\tau_{xy} + v\tau_{yy} - q_y \tag{6}$$

The stress terms in Eq. (4) can now be written as follows:

$$\tau_{xx} = \frac{2}{3}\mu\left(2\frac{\partial u}{\partial x} - \frac{\partial v}{\partial y}\right) \tag{7}$$

$$\tau_{xy} = \mu\left(\frac{\partial u}{\partial x} + \frac{\partial v}{\partial y}\right) \tag{8}$$

$$\tau_{yy} = \frac{2}{3}\mu\left(2\frac{\partial v}{\partial y} - \frac{\partial u}{\partial x}\right) \tag{9}$$

Under equilibrium conditions, Fourier's law is used to relate the heat transfer rates q_x and q_y with the temperature gradient:

$$q_x = -K\frac{\partial T}{\partial x} \tag{10}$$

$$q_y = -K\frac{\partial T}{\partial y} \tag{11}$$

The thermal conductivity, K can be related to the molecular viscosity, μ using kinetic theory of gases:

$$K = \frac{\mu c_P}{\mathrm{Pr}} \tag{12}$$

Here Pr is the Prandtl number and assumed to be 0.71.

The turbulent viscosity μ_t is calculated as follows:

$$\mu_t = \frac{\rho k}{\omega}\frac{1}{\max\left[\frac{1}{\alpha^*}, \frac{SF_2}{a_1\omega}\right]} \tag{13}$$

The coefficient α^* damps the turbulent viscosity causing a low-Reynolds-number correction.It is given by

$$\alpha^* = \alpha_\infty^*\left(\frac{\alpha_0^* + \mathrm{Re}_t/R_k}{1 + \mathrm{Re}_t/R_k}\right) \tag{14}$$

Where, Turbulent Reynolds number, $\mathrm{Re}_t = \frac{\rho k}{\mu\omega}$

Model constants $R_k = 6$, $\alpha_0^* = \frac{\beta_i}{3}$, $\beta_i = 0.072$, $a_1 = 0.31$

In the high-Reynolds-number form of the *k-ω* model, $\alpha^* = \alpha_\infty^* = 1$

Again from eq. (13) model constant, $a_1 = 0.31$ and *S* is the modulus of mean rate of strain tensor. The blending function F_2 is given below:

$$F_2 = \tan(\emptyset_2^2) \tag{15}$$

$$\emptyset_2 = \max\left[2\frac{\sqrt{k}}{0.09\omega y}, \frac{500\mu}{\rho y^2\omega}\right] \tag{16}$$

Where *y* is the distance to the next surface

The values of turbulent Prandtl numbers for k and ω are respectively σ_k and σ_ω which are given by

$$\sigma_k = \frac{1}{F_1/\sigma_{k,1} + (1 - F_1)/\sigma_{k,2}} \tag{17}$$

$$\sigma_\omega = \frac{1}{F_1/\sigma_{\omega,1} + (1 - F_1)/\sigma_{\omega,2}} \tag{18}$$

Where, model constants are $\sigma_{k,1} = 1.176, \sigma_{k,2} = 1.0, \sigma_{\omega,1} = 2.0, \sigma_{\omega,2} = 1.168$, and the blending function F_1 is given by

$$F_1 = \tan(\emptyset_1^4) \tag{19}$$

$$\emptyset_1 = \min\left[\max\left(\frac{\sqrt{k}}{0.09\omega y}, \frac{500\mu}{\rho y^2 \omega}\right), \frac{4\rho k}{\sigma_{\omega,2} D_\omega^+ y^2}\right] \tag{20}$$

$D_\omega^+$is the positive portion of the crossdiffusion termD_ω

$$D_\omega = 2(1 - F_1)\rho\sigma_{\omega,2}\frac{1}{\omega}\left(\frac{\partial k}{\partial x} + \frac{\partial k}{\partial y}\right)\left(\frac{\partial \omega}{\partial x} + \frac{\partial \omega}{\partial y}\right) \tag{21}$$

$$D_\omega^+ = \max\left[2\rho\frac{1}{\sigma_{\omega,2}}\frac{1}{\omega}\left(\frac{\partial k}{\partial x} + \frac{\partial k}{\partial y}\right)\left(\frac{\partial \omega}{\partial x} + \frac{\partial \omega}{\partial y}\right), 10^{-10}\right] \tag{22}$$

The turbulent source term $\boldsymbol{H}$ in Eq. (1) is:

$$\boldsymbol{H} = \begin{bmatrix} 0 \\ 0 \\ 0 \\ 0 \\ G_k - Y_k \\ G_\omega - Y_\omega + D_\omega \end{bmatrix} \tag{23}$$

In the above equation, G_k is the generation of turbulence kinetic energy due to mean velocity gradients. $G_\omega$represents generation of ω.$Y_k$is the dissipation of turbulent kinetic energy, k due to turbulence and Y_ω is the dissipation of ω. These functions are determined as follows:

$$G_k = \min(\mu_t S^2, 10\rho\beta^* k\omega) \tag{24}$$

Where

$$\beta^* = \beta_i^*[1 + \zeta^* F(M_t)] \tag{25}$$

$$\beta_i^* = \beta_\infty^* \left[\frac{4/15 + \left(\mathrm{Re}_t/R_\beta\right)^4}{1 + \left(\mathrm{Re}_t/R_\beta\right)^4} \right] \tag{26}$$

Here, $\zeta^* = 1.5$, $R_\beta = 8, \beta_\infty^* = 0.09, \mathrm{Re}_t = \frac{\rho k}{\mu\omega}$ and

Compressibility function,

$$F(M_t) = \begin{cases} 0 & \text{for} M_t \le M_{t0} \\ M_t^2 - M_{t0}^2 & \text{for } M_t > M_{t0} \end{cases} \tag{27}$$

Where, $M_t^2 = \frac{2k}{a^2}$, $a = \sqrt{\gamma RT}, M_{t0} = 0.25$

Again from eq. (23):

$$Y_k = \rho\beta^* k\omega \tag{28}$$

$$G_\omega = \frac{\alpha}{v_t} G_k where\ \alpha = 1.0 \tag{29}$$

$$Y_\omega = \rho\beta\omega^2 \tag{30}$$

Where,

$$\beta = \beta_i \left[1 - \frac{\beta_i^*}{\beta_i} \zeta^* F(M_t) \right] \tag{31}$$

$$\beta_i = F_1 \beta_{i,1} + (1 - F_1)\beta_{i,2} \tag{32}$$

$$\beta_{i,1} = 0.075,\ \beta_{i,2} = 0.0828$$

The governing equations are discretized spatially using a Finite volume method of second order scheme. For the time derivatives, an implicit multistage time stepping scheme, which is advanced from time t to $t+\Delta t$ with a second order Euler backward scheme for physical time and implicit pseudo-time marching scheme for inner iteration, is used. A time step size of 10^{-4} is sufficient for this type of unsteady computation.

3.4 Descretization of Flow Domain

3.4.1 Create Geometry

To specify the NASA SC(2) 0714 supercritical airfoil geometry, list of vertices along the surface was drawn by ICEM input in a preprocessing tool and these vertices were joined to create two edges, corresponding to the upper and lower surfaces of the airfoil shown in figure 3.2. Airfoil chord *c* is 0.1524 m.

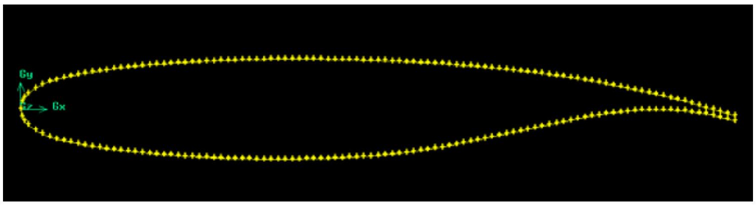

Figure 3.2: Airfoil surface with vertex data points

Top and bottom wall type boundary was created at 10*c* from the airfoil surfaces. The upstream and downstream pressure far-field boundary was created at 10*c* and 21*c* distance as shown in the following figure .33. This spacing was considered sufficient to apply free steam conditions on the outer boundaries

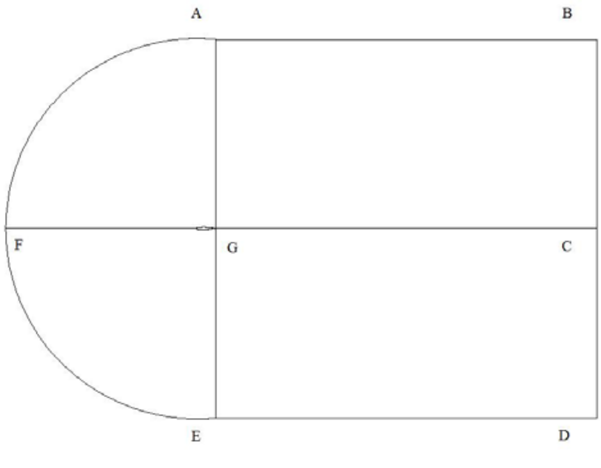

Figure 3.3: Far-field boundary around airfoil

Coordinates of the far-field boundaries are shown in table 3.1:

Table 3.1: Coordinates of far-field boundary around airfoil.

Label	x-coordinate	y-coordinate
A	c	10c
B	21c	10c
C	21c	0
D	21c	-10c
E	c	-10c
F	-10c	0
G	c	0

3.4.2 Meshing

The matter of grid generation is a significant consideration in CFD. The generation of an appropriate grid of mesh is one thing; the solution of the governing flow equations over such a grid is quite another thing.

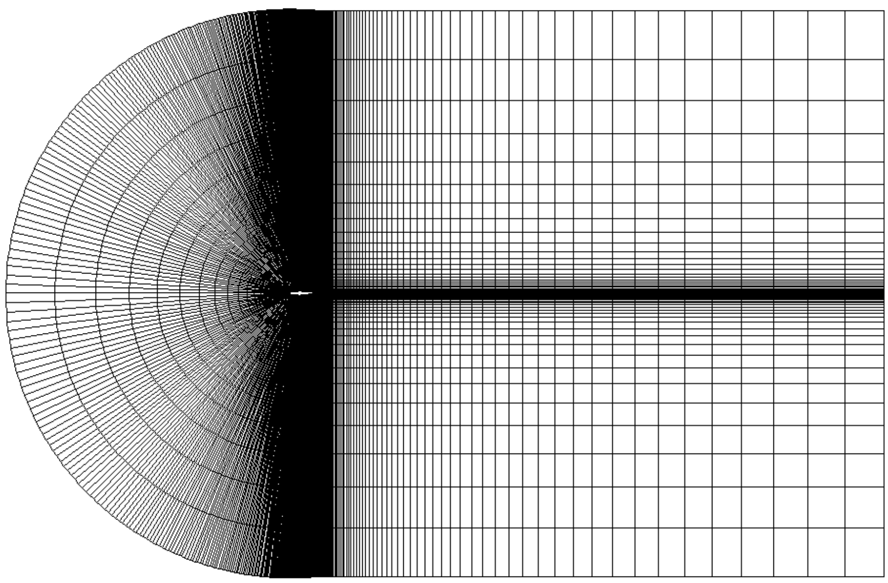

Figure 3.4: Mesh generation around airfoil

As seen from figure 3.4 that quadrilateral cells were used for this simple geometry because they can be stretched easily to account for different flow gradients in different directions. In the present case, the gradients normal to the airfoil wall are much greater than those tangents to the airfoil. Consequently, the cells near the surface have high aspect ratios. For viscous flow over the airfoil, finely spaced grid was constructed to calculate the details of the flow near the airfoil.

The total number of grid is 51000 which give a grid independent solution.

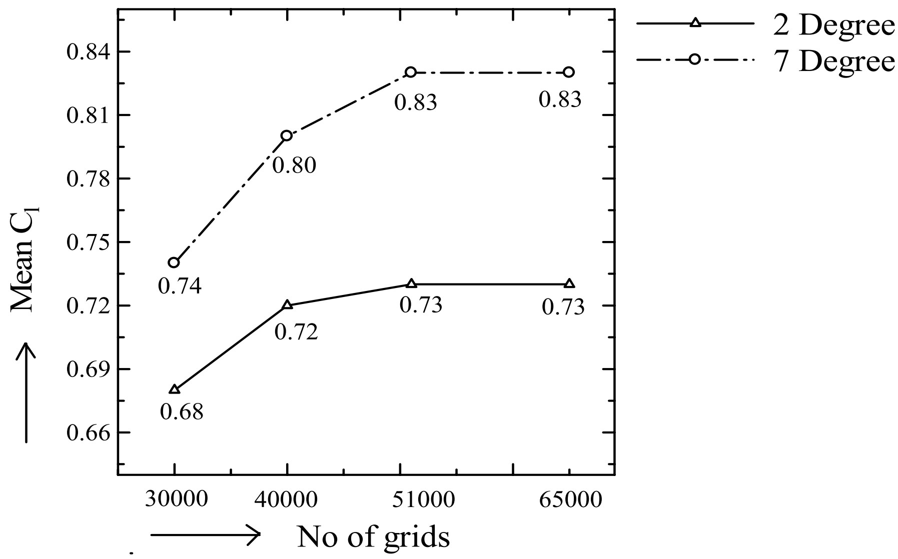

Figure 3.5: Grid independence test at 2° and 7° angle of attack for M_∞= 0.77

Grid independence test shown in figure 3.5 indicates that there is a variation of value of mean C_l among 30000, 40000 and 51000 grid number for 2° and 7° angle of attack. But for 51000 and 65000 grid number shows similar mean C_l value of 0.73 for 2° angle of attack and 0.83 for 7° angle of attack. In order to avoid computational complexity for 65000 grids, 51000 grids were chosen for computational domain.

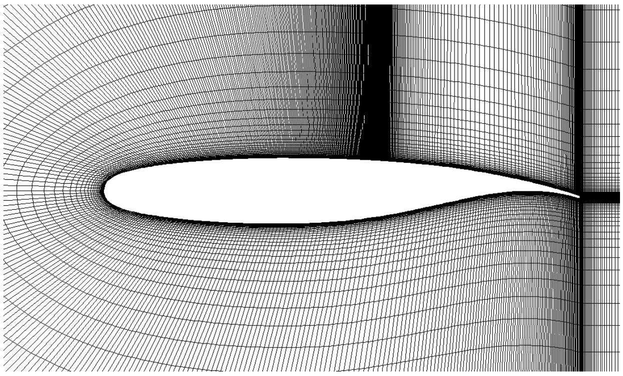

Figure 3.6: Enlarge view of mesh generation around airfoil

Mesh was generated finely around mid chord to capture shock behavior correctly (figure 3.6). As the value of wall y^+ in the wall-adjacent cells dictates how wall shear stress is calculated, grid points were selected finely around the airfoil surface to correspond wall y^+ value less than 1.The values of wall y^+ are dependent on the resolution of the grid and the Reynolds number of the flow, and are defined only in wall-adjacent cells.

3.5 Boundary Condition

For the present case, inlet and exit boundary of the domain was chosen as Pressure far-field boundary. This boundary was used to model a free-stream compressible flow at infinity, with free-stream Mach number and static conditions specified.

In some situations, it is appropriate to specify a uniform value of the turbulence quantity at the boundary where inflow occurs. In most turbulent flows, higher levels of turbulence are generated within shear layers than enter the domain at flow boundaries, making the result of the calculation relatively insensitive to the inflow boundary values. For this reason turbulence specification method was used.

To specify turbulent quantities in terms of the turbulent Intensity and Viscosity Ratio was chosen for k-ω model. The turbulence intensity is defined as the ratio of the root-mean-square of the velocity fluctuations to the mean flow velocity. A turbulence intensity of 1% or less is generally considered low and turbulence intensities greater than 10% are considered high. Turbulence intensity was selected 1% and 5%, respectively for inlet and outlet zone. The turbulent viscosity ratio is directly proportional to the turbulent Reynolds number. At the free-stream boundaries of most external flows turbulent viscosity ratio is fairly small. Typically, the turbulence parameters were set between 1 to 10. Turbulent viscosity ratio was selected 5 and 10, respectively for inlet and outlet zone in the present numerical study.

3.6 Overview of Flow Solver

CFD allows to choose one of the two numerical methods:

- Pressure-based solver
- Density-based solver

The pressure-based approach was developed for low-speed incompressible flows, while the density-based approach was mainly used for high-speed compressible flows. However, recently both methods have been extended and reformulated to solve and operate for a wide range of flow conditions beyond their traditional or original intent.

In both methods the velocity field is obtained from the momentum equations. In the density-based approach, the continuity equation is used to obtain the density field while the pressure field is determined from the equation of state. On the other hand, in the pressure-based approach, the pressure field is extracted by solving a pressure or pressure correction equation which is obtained by manipulating continuity and momentum equations. Using either method, the present CFD tool will solve the governing integral equations for the conservation of mass and momentum, and for energy and other scalars such as turbulence and chemical species. During our numerical analysis we used pressure based solver. To use the pressure-based solver, retain the default selection of Pressure Based Solver.

3.6.1 Discretization Scheme

The present CFD tool provides Standard, PRESTO! Linear, Second order, Body Force Weighted schemes for Pressure Interpolation Scheme where Second Order was selected for this case. Again for Density, Momentum, Turbulent Kinetic Energy, Specific Dissipation Rate, Energy equations have First Order Upwind, Second Order Upwind, QUICK and Third-Order MUSCL. schemes. For all cases Second Order Upwind schemes were selected.

When the flow is aligned with the grid (e.g., laminar flow in a rectangular duct modeled with a quadrilateral or hexahedral grid) the first-order upwind discretization is acceptable. When the flow is not aligned with the grid (i.e., when it crosses the grid lines obliquely), however, first-order convective discretization increases the numerical discretization error (numerical diffusion). For triangular and tetrahedral grids, since the flow is never aligned with the grid, generally more accurate results are obtained by using the second-order discretization. For quad/hex grids, better results using the second-order discretization is obtained, especially for complex flows.

3.6.2 Pressure-Velocity Coupling Method

The present CFD tool provides four segregated types of algorithms: SIMPLE, SIMPLEC, PISO, and Fractional Step (FSM). These schemes are referred to as the pressure-based segregated algorithm. Steady-state calculations will generally use SIMPLE or SIMPLEC, while PISO is recommended for transient calculations. In present CFD tool, using the Coupled algorithm enables full pressure-velocity coupling, hence it is referred to as the pressure-based coupled algorithm. This solver offers some advantages over the pressure-based segregated algorithm. The pressure-based coupled algorithm obtains a more robust and efficient single phase implementation for steady-state flows. For choosing Coupled, Courant number had to be specified. For the present numerical study it was set at 10.

3.6.3 Explicit and Under-Relaxation Factors

The Relaxation Factor field defines the explicit relaxation of variables between sub-iterations. The relaxation factors can be used to prevent the solution from diverging. They are left at their default values, unless divergence is detected. If the solution diverges, the solution is stabilized by lowering the relaxation factors.

3.6.4 Operating Condition

Operating pressure is significant for low-Mach-number compressible flows because of its role in avoiding round off error problems Operating pressure is less significant for higher-Mach-number compressible flows. The pressure changes in such flows are much larger than those in low-Mach-number compressible flows, so there is no real problem with round off error and there is no real need to use gauge pressure. The criteria for choosing a suitable operating pressure are based on the Mach-number regime of the flow and the relationship that is used to determine density. Due transonic regime and density according to ideal gas law operating pressure was set to zero.

3.6.5 Computational Condition

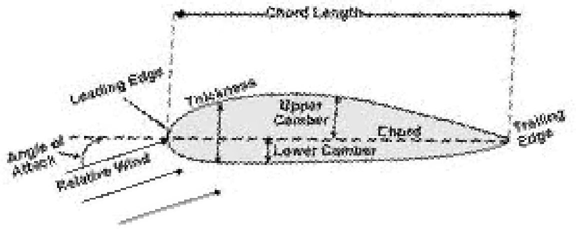

Following computational conditions were set up for the computational analysis:

M_∞= 0.77.

α= 2°, 3°, 4°, 5°, 6° and 7°.

At atmospheric condition, T_∞= 300k, P_0= 101325 Pa,

For air, ρ= 1.176674 kg/m^3, μ= 1.7894*10^{-5} N.s/m^2, v_∞=267.2575 m/s for M_∞=0.77, c=0.1524 m.

$Re = \frac{\rho v_\infty c}{\mu}$ = 2.68 X 10^6.

3.6.6 FMG Initialization

The Full Multi Grid (FMG) initialization can provide initial and approximate solution at a minimum cost to the overall computational expense. FMG initialization utilizes the FAS Multi grid technology to obtain the initial solution. Starting from a uniform solution the FMG initialization procedure constructs the desirable number of geometric grid levels using Full-Approximation Storage (FAS) Multigrid. To begin the process, the initial solution is restricted all the way down to the coarsest level. The FAS multigrid cycle is then applied until a given order of residual reduction is obtained or the maximum number of cycles is reached. The solution is then interpolated one grid level up and the FAS multigrid cycle is applied again between the current level all the way down to the coarsest level. This process will repeat until the finest level is reached.

3.6.7 Monitoring Solution Convergence

At the end of each solver iteration, the residual sum for each of the conserved variables is computed and stored, thus recording the convergence history. This history is also saved in the data file. On a computer with infinite precision, these residuals will go to zero as the solution converges. On an actual computer, the residuals decay to some small value and then stop changing. For the present case all residual value was set to .00001 for continuity, x velocity, y velocity, energy, turbulent kinetic energy and specific dissipation rate.

3.6.8 Time Step Size

The sampling was done with time step size 0.0001 second with total time step 10000. In order to verify time step size affectivity time step sensitivity test was done.

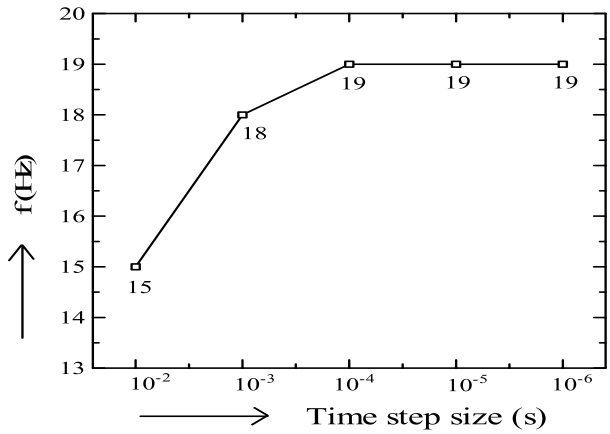

Figure 3.7: Time step size sensitivity test for $M_\infty = 0.77$, $\alpha = 3°$

Time step size sensitivity test for 3° angle of attack shown in figure 3.7 indicates that there is a variation of value of frequency of oscillation among 10^{-2}, 10^{-3} and 10^{-4} second time step size. But time step size 10^{-4}, 10^{-5} and 10^{-6} second shows similar frequency of oscillation 19.04 Hz. In order to avoid computational complexity for 10^{-5} and 10^{-6} second time step size, 10^{-4} second time step size were chosen for iteration.

CHAPTER 4

RESULTS AND DISCUSSION

4.1 Validation

Before going to the detail discussion of the present problem, the computational results have been validated with the available experimental data. Computational validation has been performed by comparing pressure coefficients over the supercritical airfoil for three different conditions (a) M_∞ = 0.72, α = 2.5^o; (b) M_∞ = 0.74, α = 2.0^o and (c) M_∞ = 0.74, α = 3.0^o. Experimental results are obtained from ref [26].

Figure 4.1 shows the distribution of pressure coefficient, C_p along the airfoil surfaces obtained both from the experiments and the computations for different buffet conditions. The open square symbols are the experimental data and the closed circles are the computational results. In general the trend of C_p are same along the airfoil surfaces both from experiment and the computations. The positions of the shock wave are also at the identical positions for both experimental and computational cases. However, for M_∞ = 0.72, α = 2.5^o, computational results are showing larger pressure drop than the experimental values on the upper surface of the airfoil as shown in the Fig 3 (a). However, a good relation exists between the experiment and present computational results for other conditions as shown in Figs. 3(b) and 3(c).

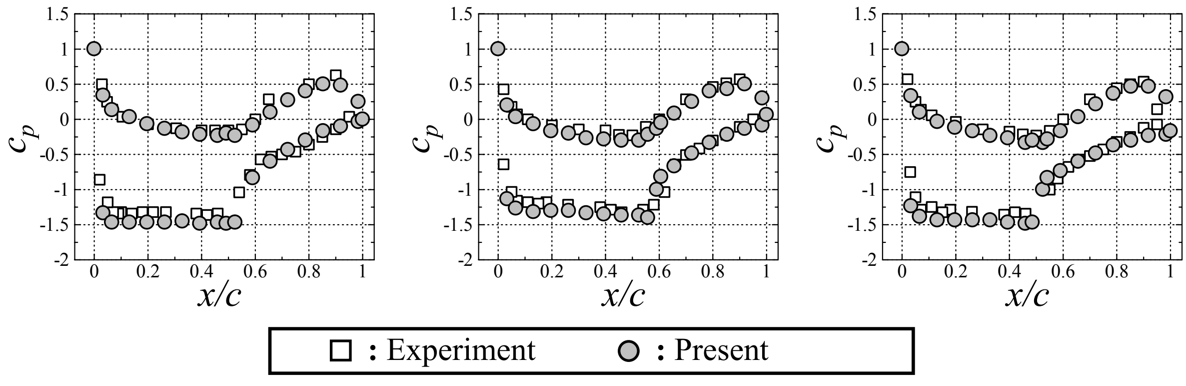

(a) (b) (c)

Figure 4.1: Distribution of pressure coefficient along the airfoil surfaces; (a) M_∞ = 0.72, α = 2.5^o; (b) M_∞ = 0.74, α = 2.0^o and (c) M_∞ = 0.74, α = 3.0^o.

4.2 Sequential Mach contour:

For free stream Mach number 0.77 and angle of attack 2°, 3°, 4°, 5°, 6°, 7° following Mach contours have been found in a 2D analysis of NASA SC(2)-0714 supercritical airfoil.

4.2.1 Case: Angle of Attack 2°

During Mach contour study for M_∞ = 0.77and α = 2° (figure 4.2) normal shock is observed along mid chord position of airfoil. Free stream Mach number 0.77 is gradually increased and forms supersonic region of Mach contour. At last local Mach number 1.40 is reached just in front of normal shock with small region. Behind the shock wave to trailing edge subsonic region is found for pressure wave and wake. For this case steady behavior of the shock is observed hence no shock movement. Type 1 shock – boundary layer interaction is detected proposed by Mundell and Mabey [59]. Attached flow region all over the upper surface is observed.

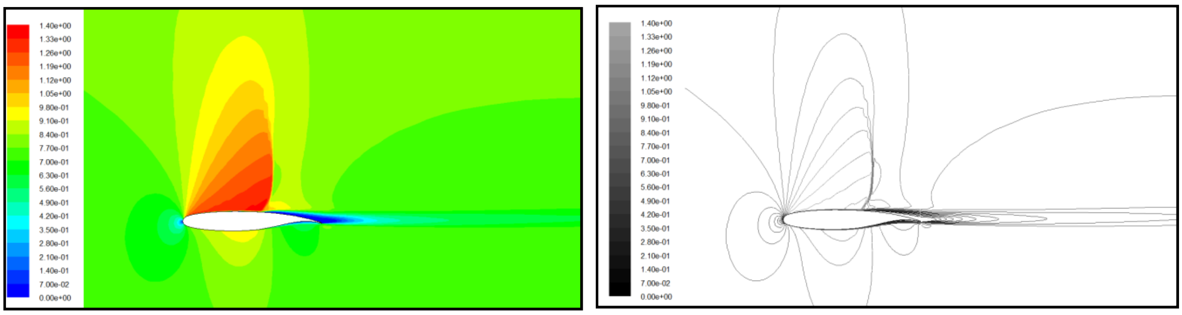

Figure 4.2: Contours of Mach number for M_∞= 0.77, α = 2°

4.2.2 Case: Angle of Attack 3°

For Mach contour investigation with $M_{\infty} = 0.77$ and $\alpha = 3°$ (figure 4.3 (a)) local Mach number 1.45 is reached in front of shock wave which was found 1.40 for $\alpha = 2°$. At this case shock buffet is observed with small displacement which can be assured with fluctuated lift and drag coefficient. From Mach contour in one cycle of flow oscillation it is observed that from $t = 0/10\ T$ to $t = 1/10\ T$ the supersonic region of Mach contour is wide but from $t = 2/10\ T$ to$t = 7/10\ T$ it becomes narrow again from $t = 8/10\ T$ to $t = 10/10\ T$ it becomes wide. Type 1 shock – boundary layer interaction with attached flow region throughout the upper surface is detected proposed by Mundell and Mabey [59]. No signification formation of vortex is observed during this time period (figure 4.3 (b)).

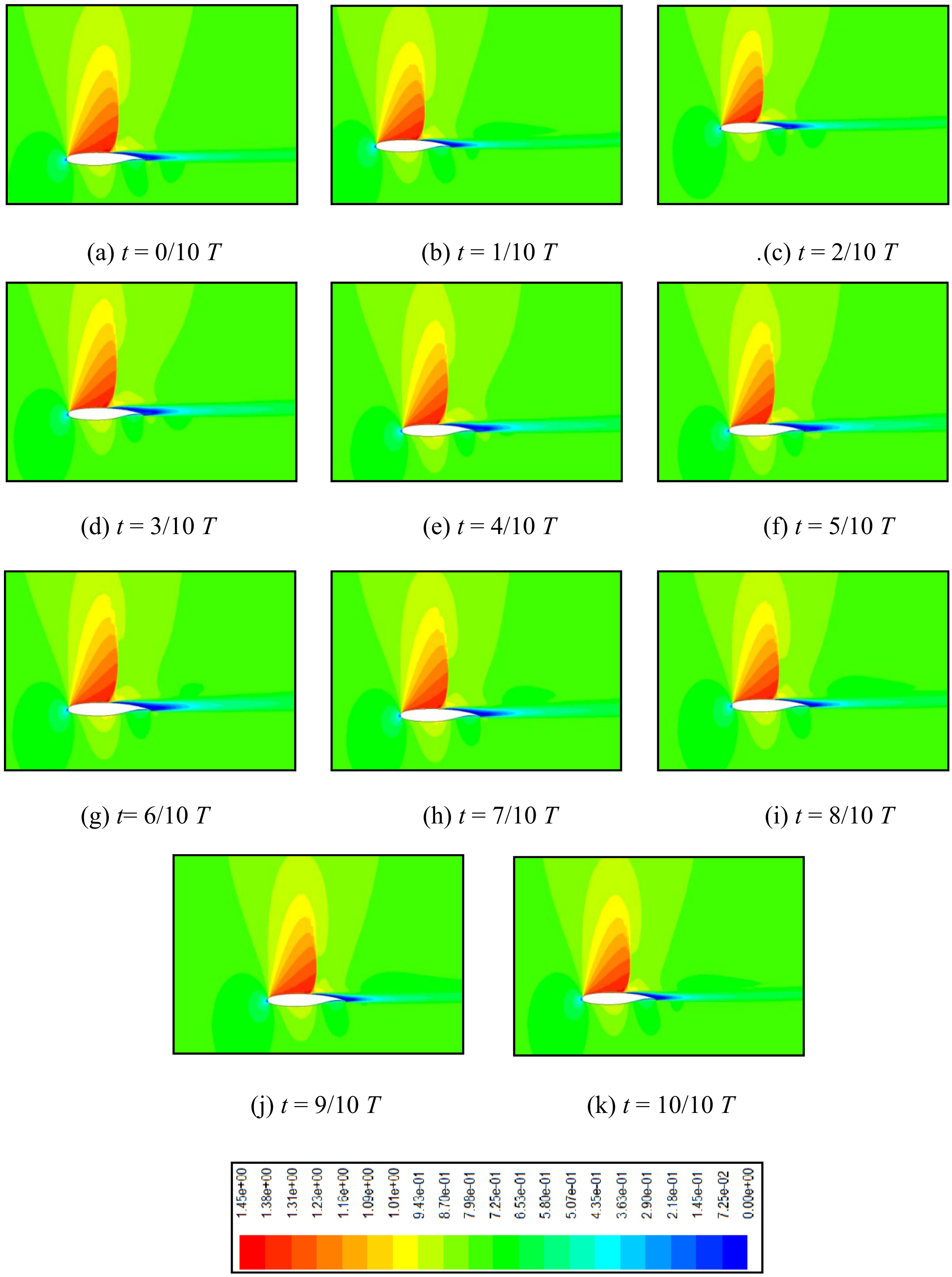

Figure 4.3 (a): Contours of Mach number (with filled) during one cycle of flow oscillation, for $M_\infty = 0.77$, $\alpha = 3°$.

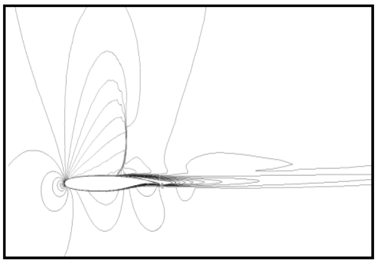

(a) $t = 0/10\ T$

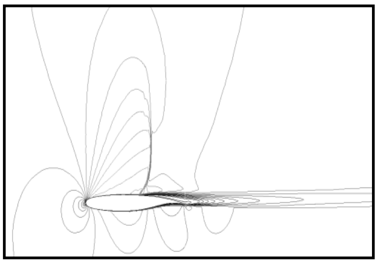

(b) $t = 1/10\ T$

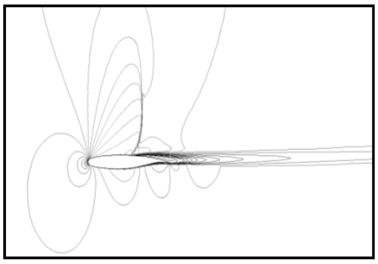

(c) $t = 2/10\ T$

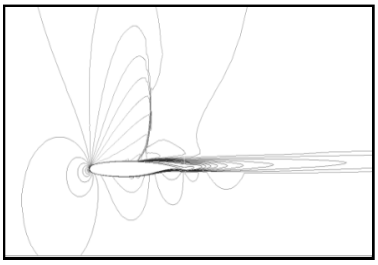

(d) $t = 3/10\ T$

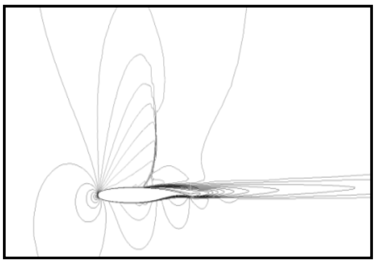

(e) $t = 4/10\ T$

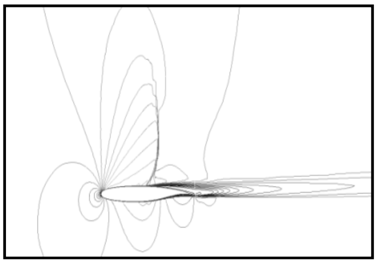

(f) $t = 5/10\ T$

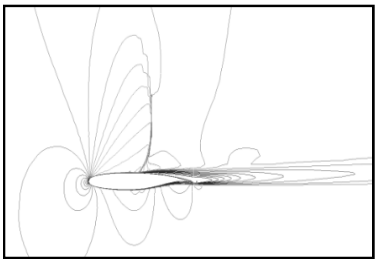

(g) $t = 6/10\ T$

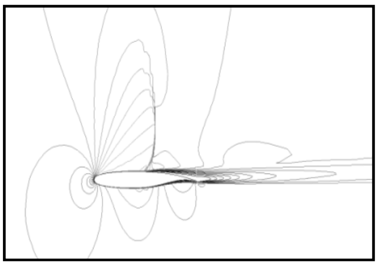

(h) $t = 7/10\ T$

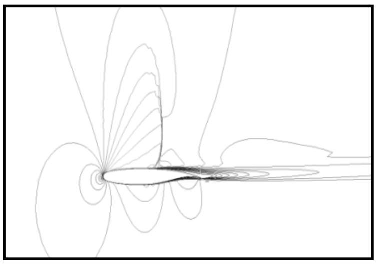

(i) $t = 8/10\ T$

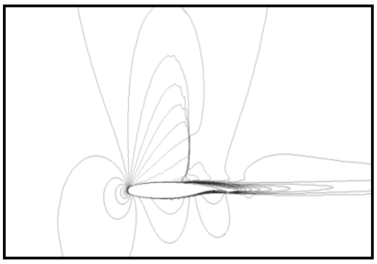

(j) $t = 9/10\ T$

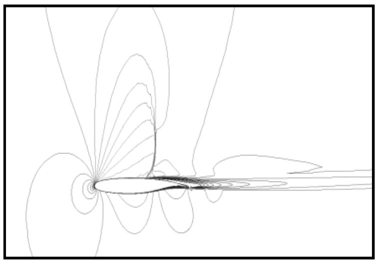

(k) $t = 10/10\ T$

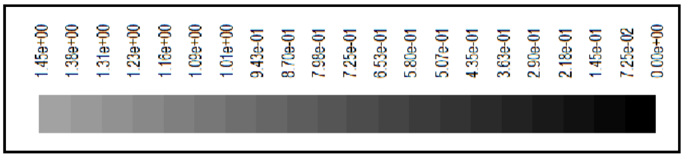

Figure 4.3 (b): Contours of Mach number (with line) during one cycle of flow oscillation, for $M_\infty = 0.77$, $\alpha = 3°$.

4.2.3 Case: Angle of Attack 4°

During this case following observations are found:

1. As seen from figure 4.4 (a) with same free stream Mach number 0.77 and α = 4° maximum local Mach number shifts from 1.42 to 1.50 which was found 1.45 for α = 3°. During one cycle oscillation period of flow cycle it is observed that local Mach number 1.50 is reached in front of shock wave from t = 0/10 T to t = 3/10 T time instances, from t = 4/10 T to t = 8/10 T time instances Mach number 1.42 and from t = 9/10 T to t = 10/10 T time instances local Mach number 1.50 is observed.

2. To find shock boundary layer interaction type proposed by Mundell and Mabey [59], the observations are; Type 1 shock – boundary layer interaction is detected from t = 0/10 T to t = 2/10 T, type 3 shock – boundary layer interaction is observed from t = 3/10 T to t = 6/10 T and again type 1shock – boundary layer interaction is noticed from t = 7/10 T to t = 10/10 T.

3. Attached flow region from t = 0/10 T to t = 2/10 T throughout the upper surface, separated flow region from t = 3/10 T to t = 6/10 T from shock position to trailing edge and again attached flow region from t = 7/10 T to t = 10/10 T all over the upper surface is observed.

4. During the separated flow region a bulge is observed (figure 4.4 (b)) which then forms a new vortex and becomes larger. A secondary vortex is also formed at the vicinity of trailing edge which coalesces and forms large separated flow region.

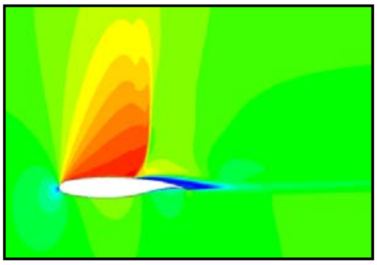

(a) $t = 0/10\ T$

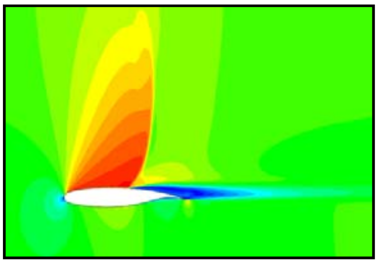

(b) $t = 1/10\ T$

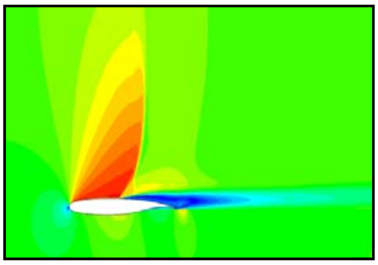

(c) $t = 2/10\ T$

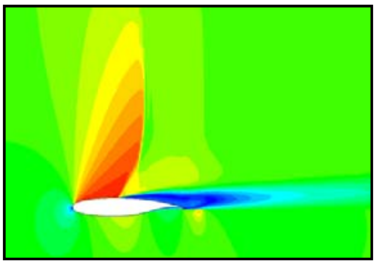

(d) $t = 3/10\ T$

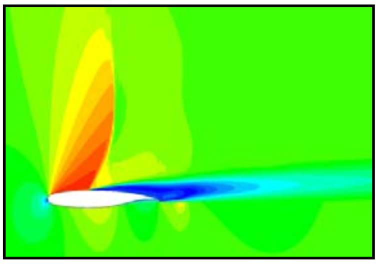

(e) $t = 4/10\ T$

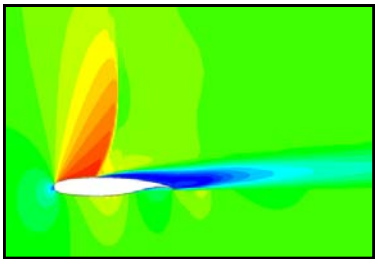

(f) $t = 5/10\ T$

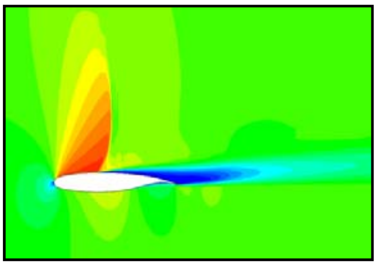

(g) $t = 6/10\ T$

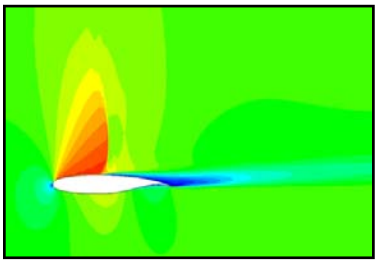

(h) $t = 7/10\ T$

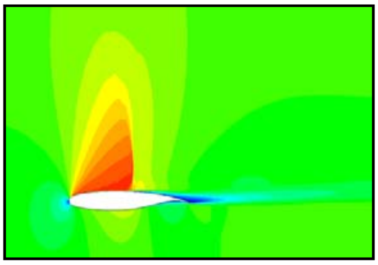

(i) $t = 8/10\ T$

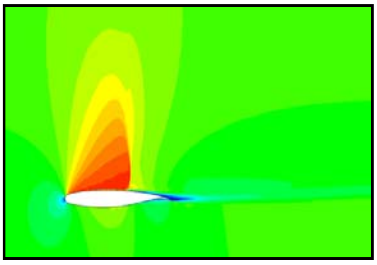

(j) $t = 9/10\ T$

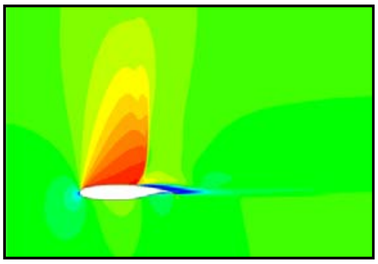

(k) $t = 10/10\ T$

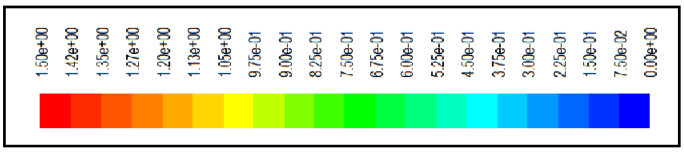

Figure 4.4 (a): Contours of Mach number (with filled) during one cycle of flow oscillation, for $M_\infty = 0.77$, $\alpha = 4°$.

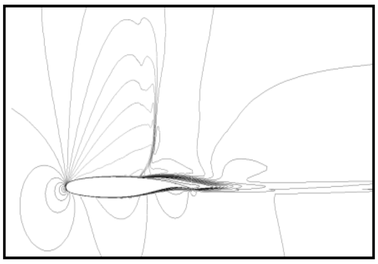

(a) $t = 0/10\ T$

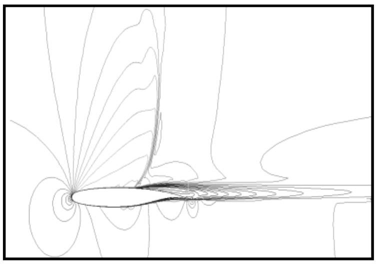

(b) $t = 1/10\ T$

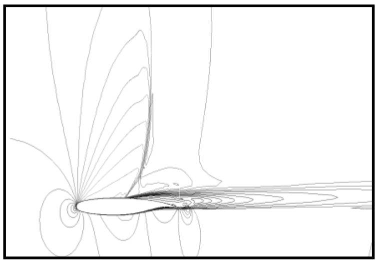

(c) $t = 2/10\ T$

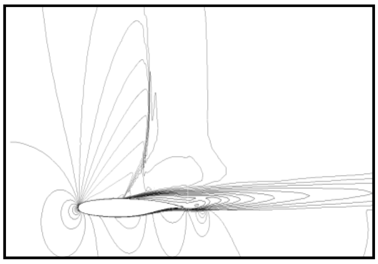

(d) $t= 3/10\ T$

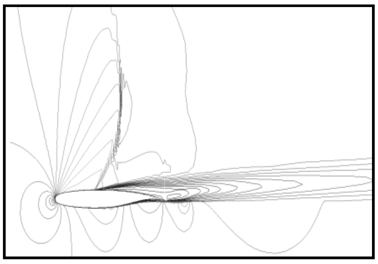

(e) $t = 4/10\ T$

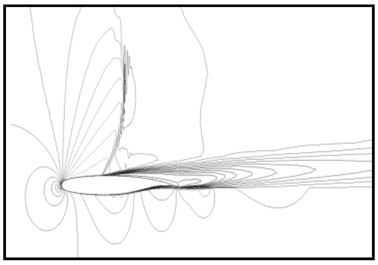

(f) $t = 5/10\ T$

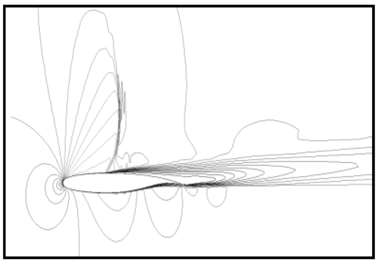

(g) $t = 6/10\ T$

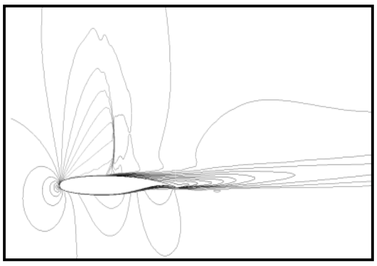

(h) $t = 7/10\ T$

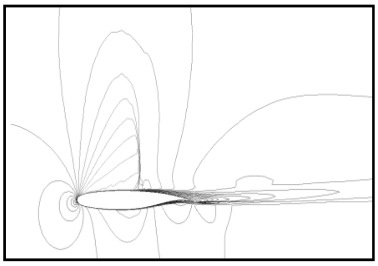

(i) $t = 8/10\ T$

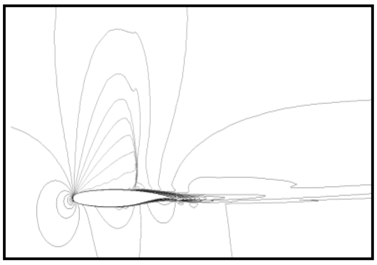

(j) $t = 9/10\ T$

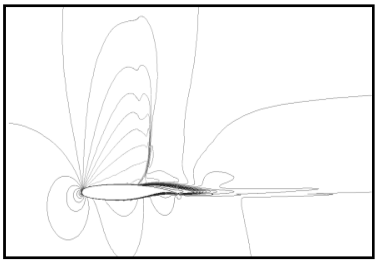

(k) $t = 10/10\ T$

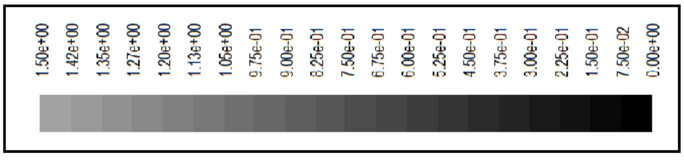

Figure 4.4 (b): Contours of Mach number (with line) during one cycle of flow oscillation, for M_∞= 0.77, $\alpha = 4°$.

4.2.4 Case: Angle of Attack 5°

During this case following observations are found:

1. From figure 4.5 (a) local Mach number 1.50 is reached in front of shock wave from t = 0/10 T to t = 5/10 T, from t = 6/10 T to t = 8/10 T Mach number 1.42 and from t = 9/10 T to t = 10/10 T Mach number 1.50 is observed.

2. Type 1 shock – boundary layer interaction is detected from t = 0/10 T and from t = 8/10 T to t = 10/10 T, type 2 shock – boundary layer interaction is observed from t = 1/10 T to t = 5/10 T and t = 7/10 T time instance again type 3shock – boundary layer interaction is noticed at t = 6/10 T proposed by Mundell and Mabey [59].

3. Attached flow region is found at t = 0/10 T time instance throughout the upper surface, separated flow region is observed from t = 1/10 T to t = 7/10 T time instance on shock position to trailing edge and again attached flow region from t = 8/10 T to t = 10/10 T all over the upper surface is observed.

4. For this case also during the separated flow region a bulge is observed (figure 4.5 (b)) which then forms a new vortex and becomes larger. A secondary vortex is also formed at the vicinity of trailing edge which coalesces and forms large separated flow region.

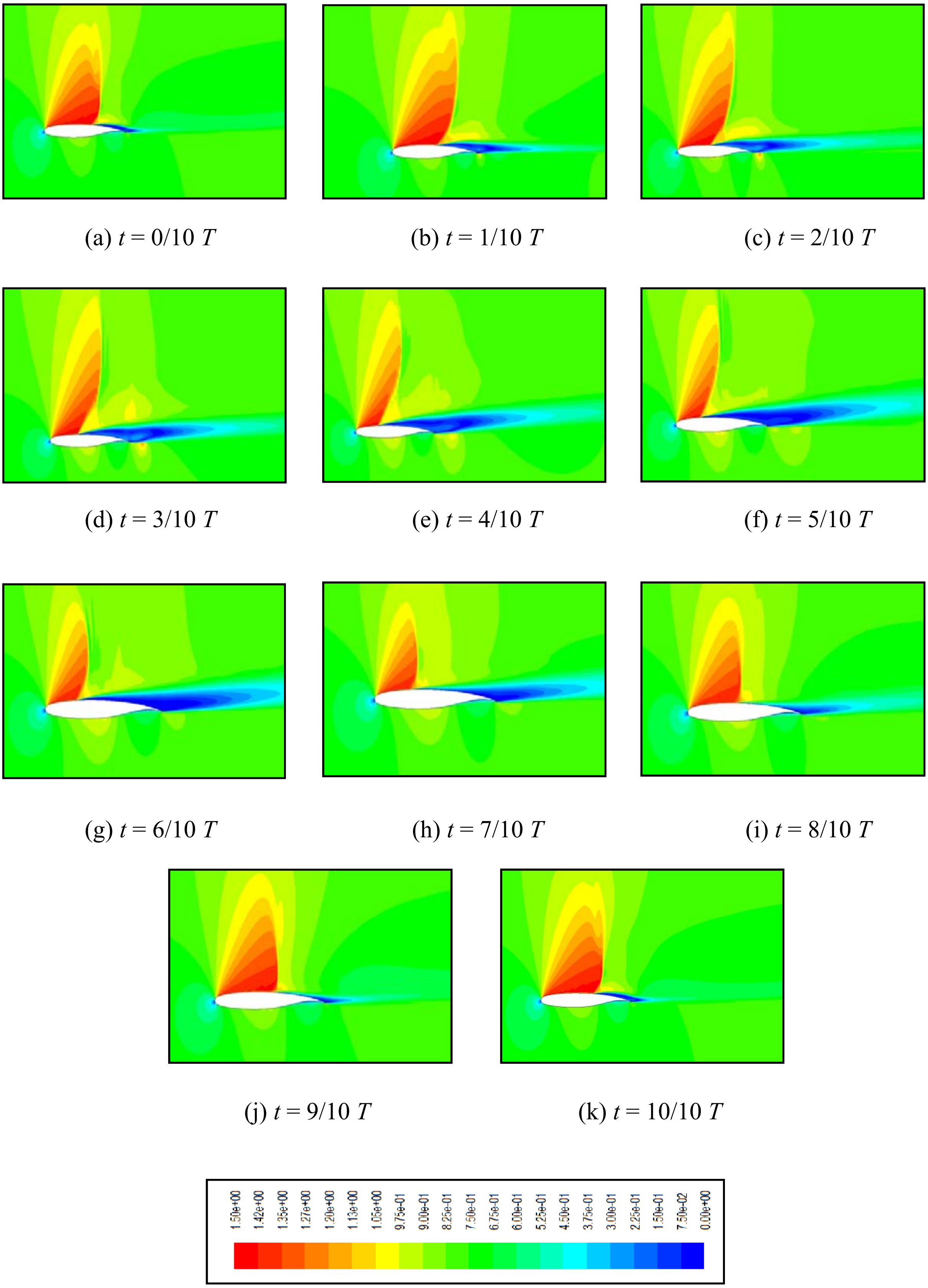

(a) $t = 0/10\ T$ (b) $t = 1/10\ T$ (c) $t = 2/10\ T$

(d) $t = 3/10\ T$ (e) $t = 4/10\ T$ (f) $t = 5/10\ T$

(g) $t = 6/10\ T$ (h) $t = 7/10\ T$ (i) $t = 8/10\ T$

(j) $t = 9/10\ T$ (k) $t = 10/10\ T$

Figure 4.5 (a): Contours of Mach number (with filled) during one cycle of flow oscillation, for $M_\infty = 0.77$, $\alpha = 5°$.

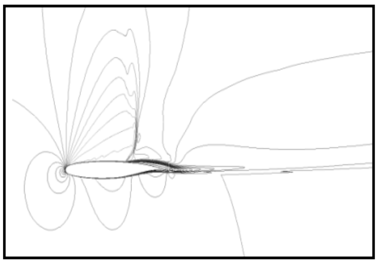
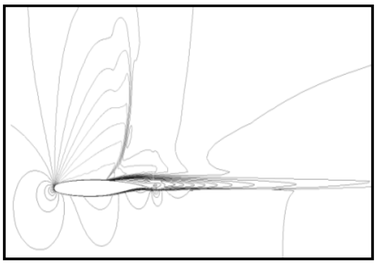
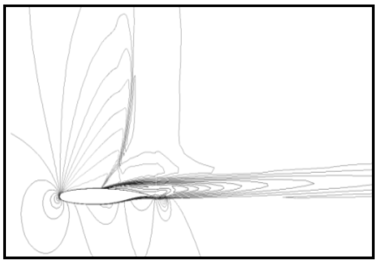

(a) t = 0/10 T (b) t = 1/10 T (c) t = 2/10 T

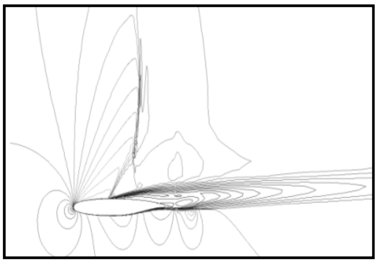
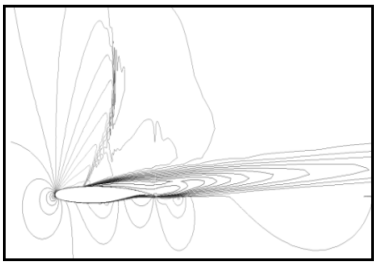
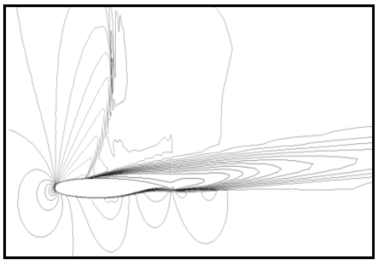

(d) t= 3/10 T (e) t = 4/10 T (f) t = 5/10 T

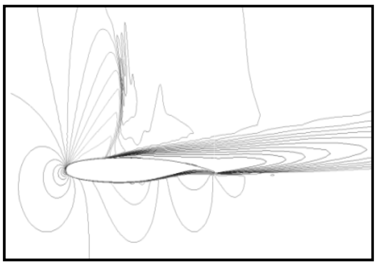
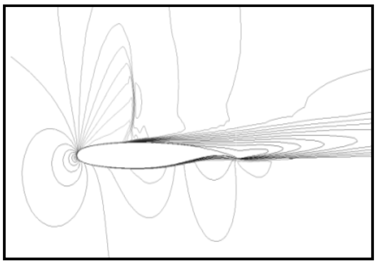
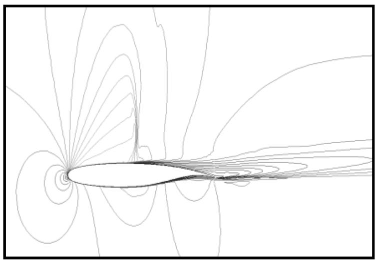

(g) t = 6/10 T (h) t = 7/10 T (i) t = 8/10 T

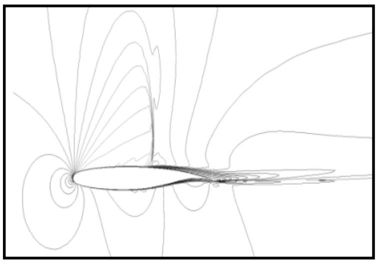
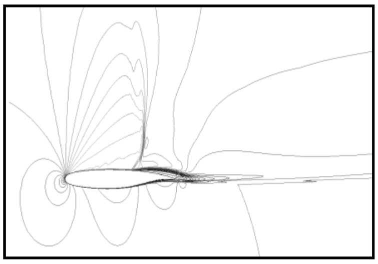

(j) t = 9/10 T (k) t = 10/10 T

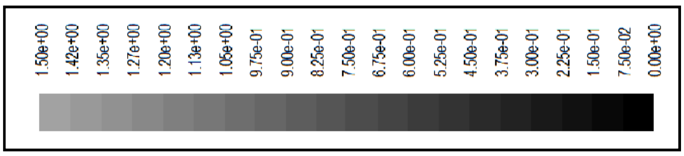

Figure 4.5 (b): Contours of Mach number (with line) during one cycle of flow oscillation, for M_{∞}= 0.77, α = 5°.

4.2.5 Case: Angle of Attack 6°

During this case following observations are found:

1. Local Mach number 1.55 is reached in front of shock wave (figure 4.6 (a)) from t = 0/10 T to t = 4/10 T time instance, from t = 5/10 T to t = 8/10 T time instance Mach number 1.47 is reached and from t = 9/10 T to t = 10/10 T time instance Mach number 1.55 is observed.

2. Type 1 shock – boundary layer interaction is detected at t = 0/10 T and from t = 9/10 T to t = 10/10 T time instance, type 2 shock – boundary layer interaction is observed from t = 1/10 T to t = 4/10 T time instance and from t = 7/10 T to t = 8/10 T time instance. Again type 3shock – boundary layer interaction is noticed at t = 5/10 T and t = 6/10 T time instance proposed by Mundell and Mabey [59].

3. Attached flow region is found at t = 0/10 T time instance throughout the upper surface, separated flow region from t = 1/10 T to t = 8/10 T time instance from shock position to trailing edge and again attached flow region from t = 9/10 T to t = 10/10 T time instance all over the upper surface is observed.

4. Similar to the previous case, during the separated flow region a bulge is observed (figure 4.6 (b)) which then forms a new vortex and becomes larger. A secondary vortex is also formed at the vicinity of trailing edge which coalesces and forms large separated flow region.

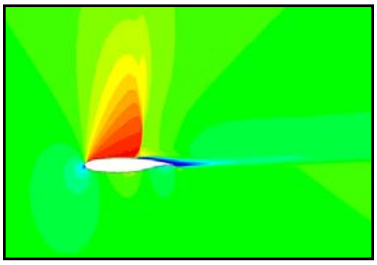

(a) t= 0/10 T

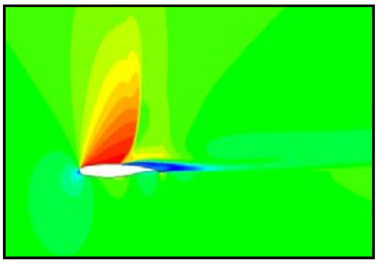

(b) t = 1/10 T

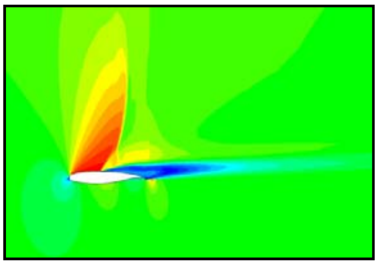

(c) t = 2/10 T

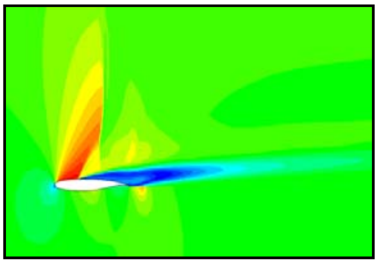

(d) t = 3/10 T

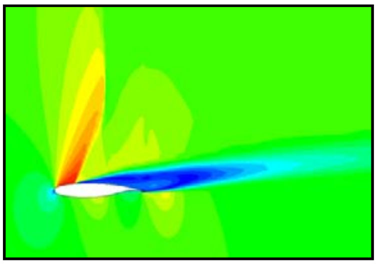

(e) t = 4/10 T

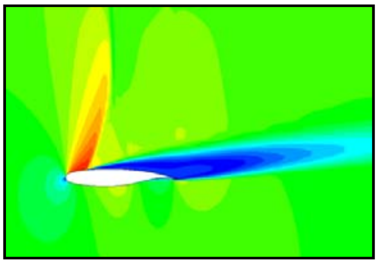

(f) t = 5/10 T

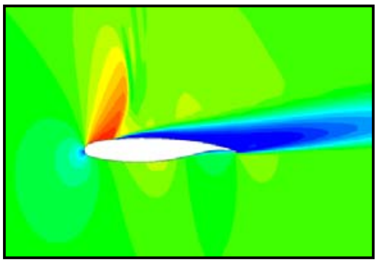

(g) t = 6/10 T

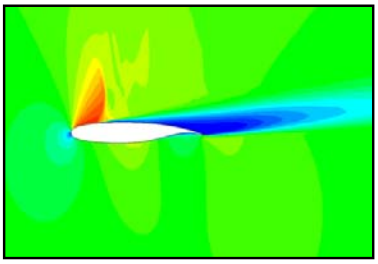

(h) t = 7/10 T

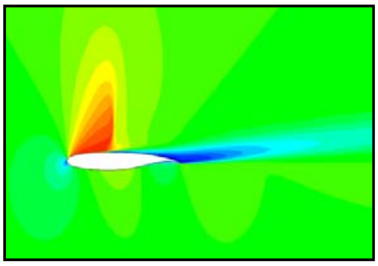

(i) t = 8/10 T

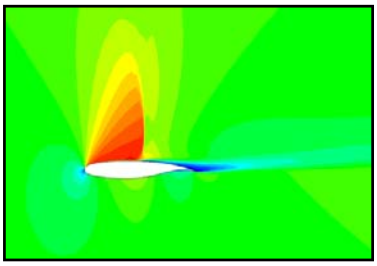

(j) t= 9/10 T

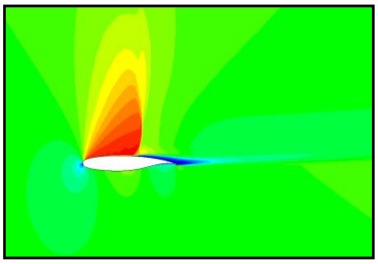

(k) t = 10/10 T

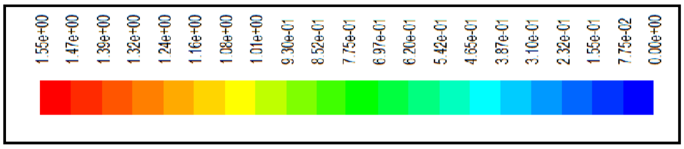

Figure 4.6 (a): Contours of Mach number (with filled) during one cycle of flow oscillation, for M_{∞} = 0.77, α = 6°.

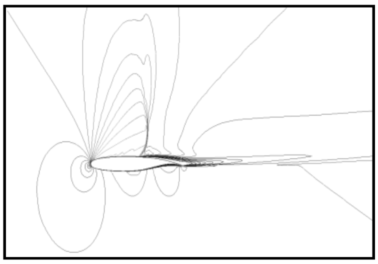

(a) t = 0/10 T

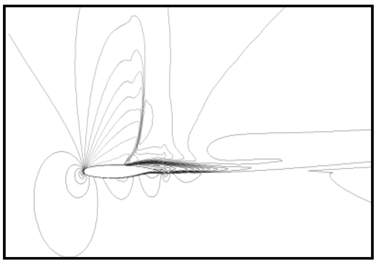

(b) t = 1/10 T

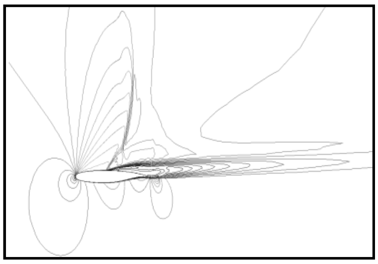

(c) t = 2/10 T

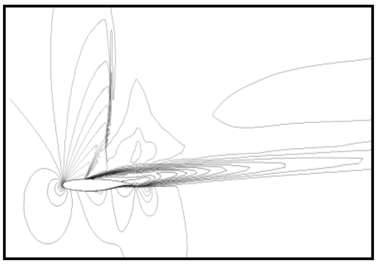

(d) t = 3/10 T

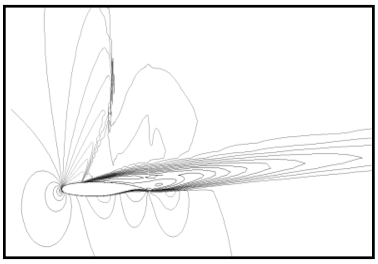

(e) t = 4/10 T

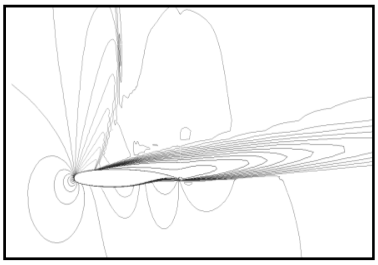

(f) t = 5/10 T

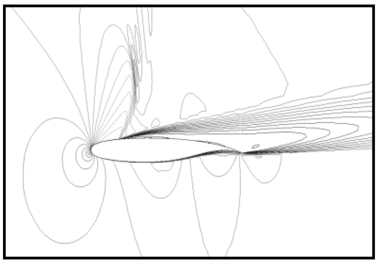

(g) t = 6/10 T

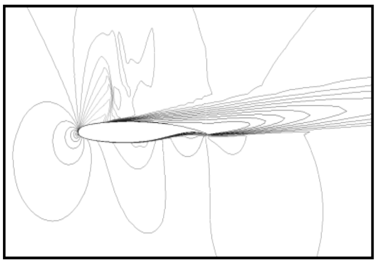

(h) t = 7/10 T

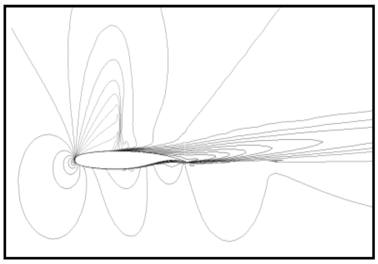

(i) t = 8/10 T

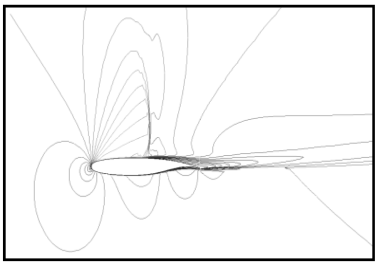

(j) t = 9/10 T

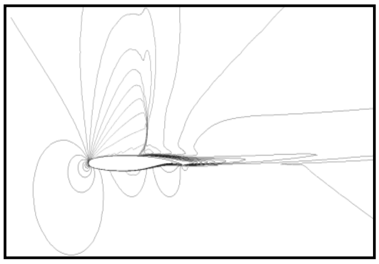

(k) t = 10/10 T

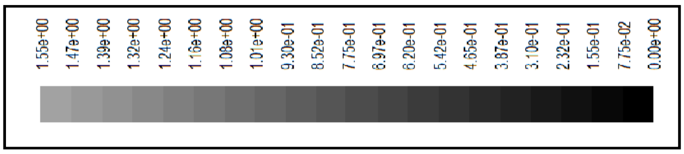

Figure 4.6 (b): Contours of Mach number (with line) during one cycle of flow oscillation, for $M_\infty = 0.77$, $\alpha = 6°$.

4.2.6 Case: Angle of Attack 7°

Following observations are found during this case:

1. Local Mach number 1.60 is reached (figure 4.7 (a)) in front of shock wave from t = 0/10 T to t = 2/10 T time instance, from t = 3/10 T to t = 8/10 T time instance Mach number 1.52 is reached and from t = 9/10 T to t = 10/10 T time instance Mach number 1.60 is observed.

2. Type 2 shock – boundary layer interaction is observed from t = 0/10 T to t = 3/10 T time instance and from t = 7/10 T to t = 10/10 T time instance. Again type 3shock – boundary layer interaction is noticed at t = 4/10 T to t = 6/10 T time instance proposed by Mundell and Mabey [59].

3. Fully separated flow region from t = 0/10 T to t = 10/10 T time instances all over the upper surface is observed.

4. For this situation also during the separated flow region a bulge is observed (figure 4.7 (b)) which then forms a new vortex and becomes larger. A secondary vortex is also formed at the vicinity of trailing edge which coalesces and forms large separated flow region.

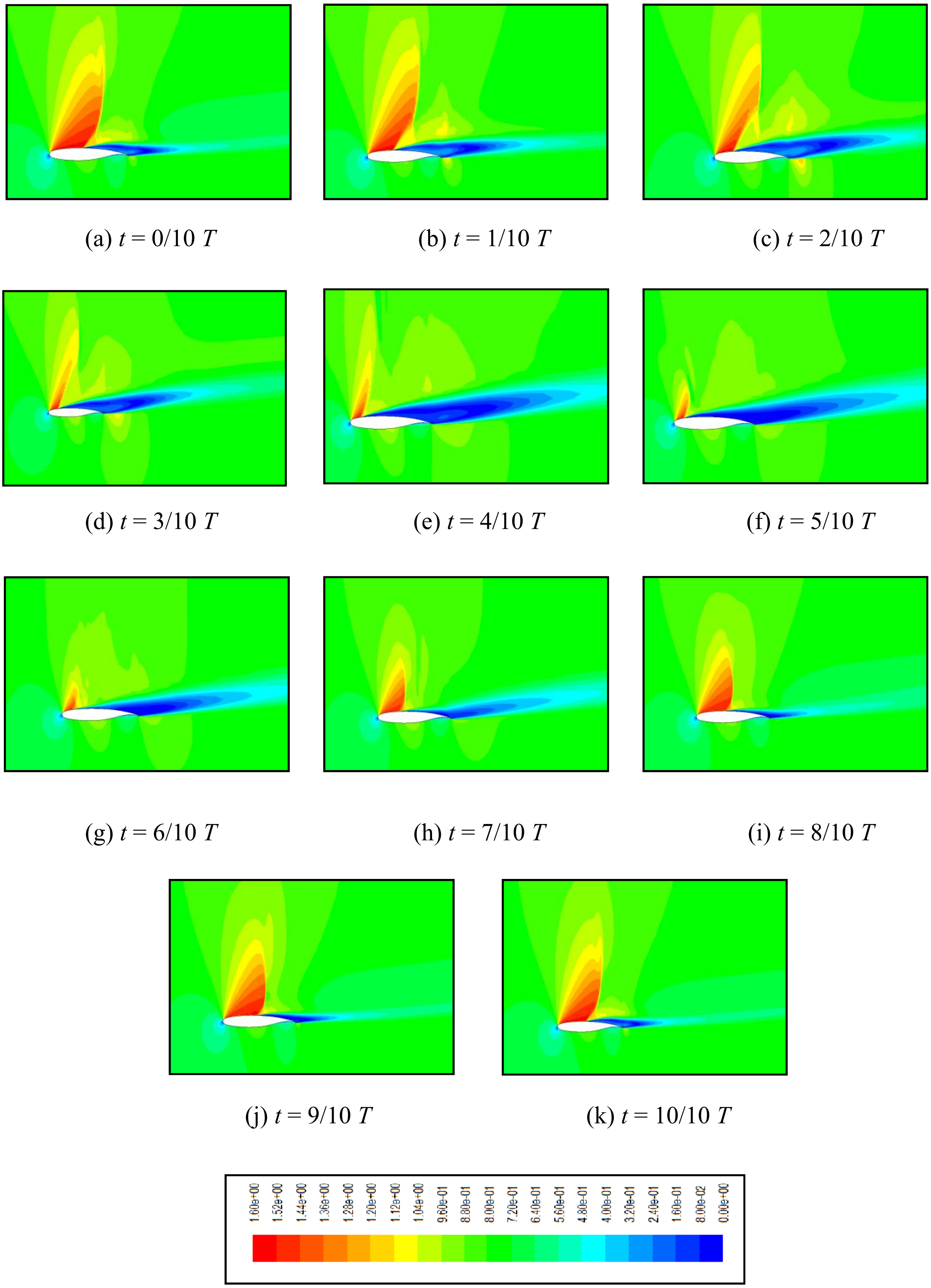

Figure 4.7 (a): Contours of Mach number (with filled) during one cycle of flow oscillation, for $M_\infty = 0.77$, $\alpha = 7°$.

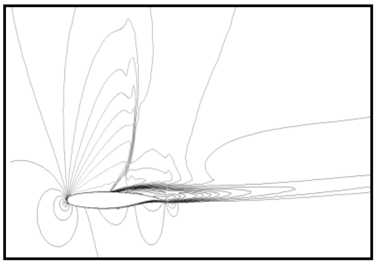

(a) t = 0/10 T

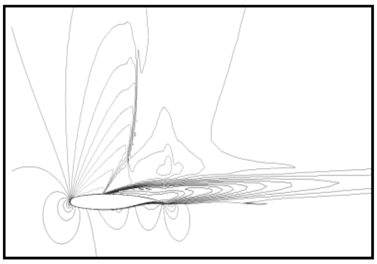

(b) t = 1/10 T

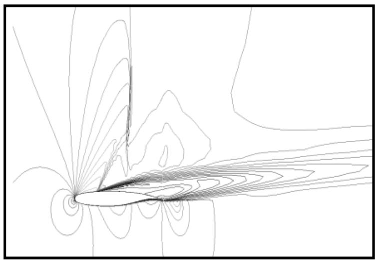

(c) t = 2/10 T

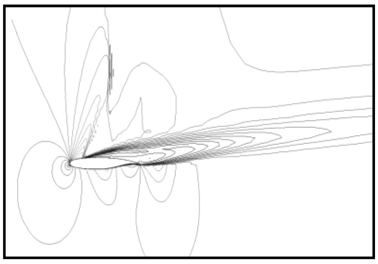

(d) t = 3/10 T

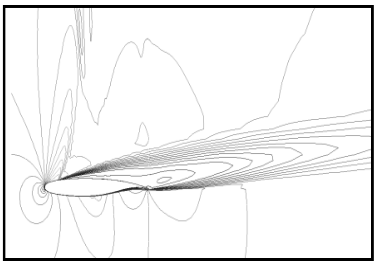

(e) t = 4/10 T

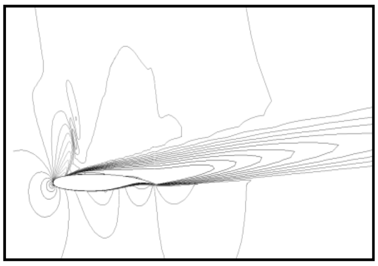

(f) t = 5/10 T

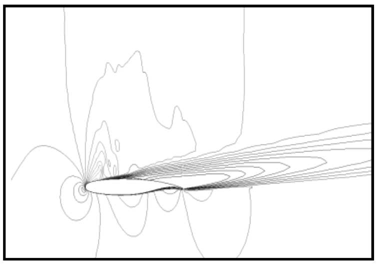

(g) t = 6/10 T

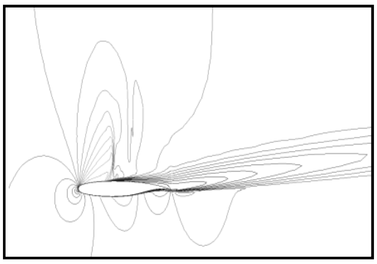

(h) t = 7/10 T

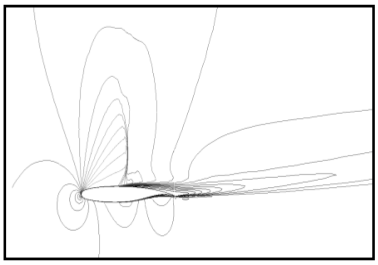

(i) t = 8/10 T

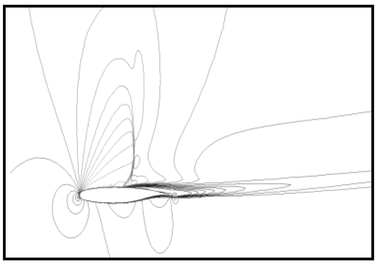

(j) t = 9/10 T

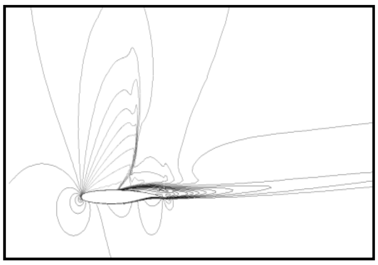

(k) t = 10/10 T

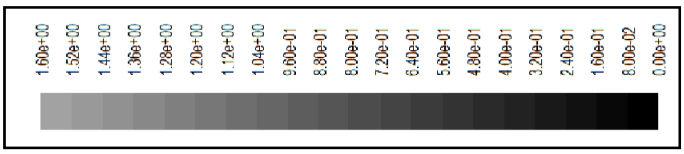

Figure 4.7 (b): Contours of Mach number (with line) during one cycle of flow oscillation, for $M_\infty = 0.77$, $\alpha = 7°$.

An overview for all of the cases are given below:

1. Shock oscillation occurs only on the upper surface of the airfoil.

2. t = 0/10 T corresponds to the time instance at which lift coefficient C_l is maximum which reduces to minimum and increases further during the sequential time instances and at t = 10/10 T it corresponds to maximum lift coefficient C_l.

3. The shock motion is clearly seen. Due to shock/boundary layer interaction large boundary layer separation occurs. The extension of separation region is time dependent.

4. The periodic motion of the shock leads to the development of a periodic wake. The downstream movement of the shock produces pressure waves that interact with the trailing edge and propagate upstream. The interaction of these waves with the shock leads to an energy transfer that sustains the shock motion.

5. At t = 0/10 T time instance shock strength is maximum which moves to upstream and reduces to minimum at downstream position. Shock strength increases further during the sequential time instances and moves downstream and at t = 10/10 T it corresponds to maximum shock strength.

4.3 Lift and Drag Coefficient

Comparing the C_l during one second time period for different angle of attack with same free stream Mach number 0.77 (figures 4.8), it was found that for angle of attack 2° no shock induced oscillation was observed in Mach contour diagram, hence no oscillation of lift coefficient is observed. From 3^{o} as the oscillation starts lift coefficient also fluctuates with low amplitude. For other increased angle of attack this oscillation take place with larger amplitude. For 3^{o} angle of attack it varies from 0.73 to 0.828 with a deviation of 0.049, for 4^{o} it varies from 0.632 to 1.02 with a deviation of 0.194. Again for 5^{o}, 6^{o} and 7^{o} it varies from 0.594 to 1.12, 0.558 to 1.165 and 0.519 to 1.144 with a deviation of 0.263, 0 303 and 0 313 respectively.

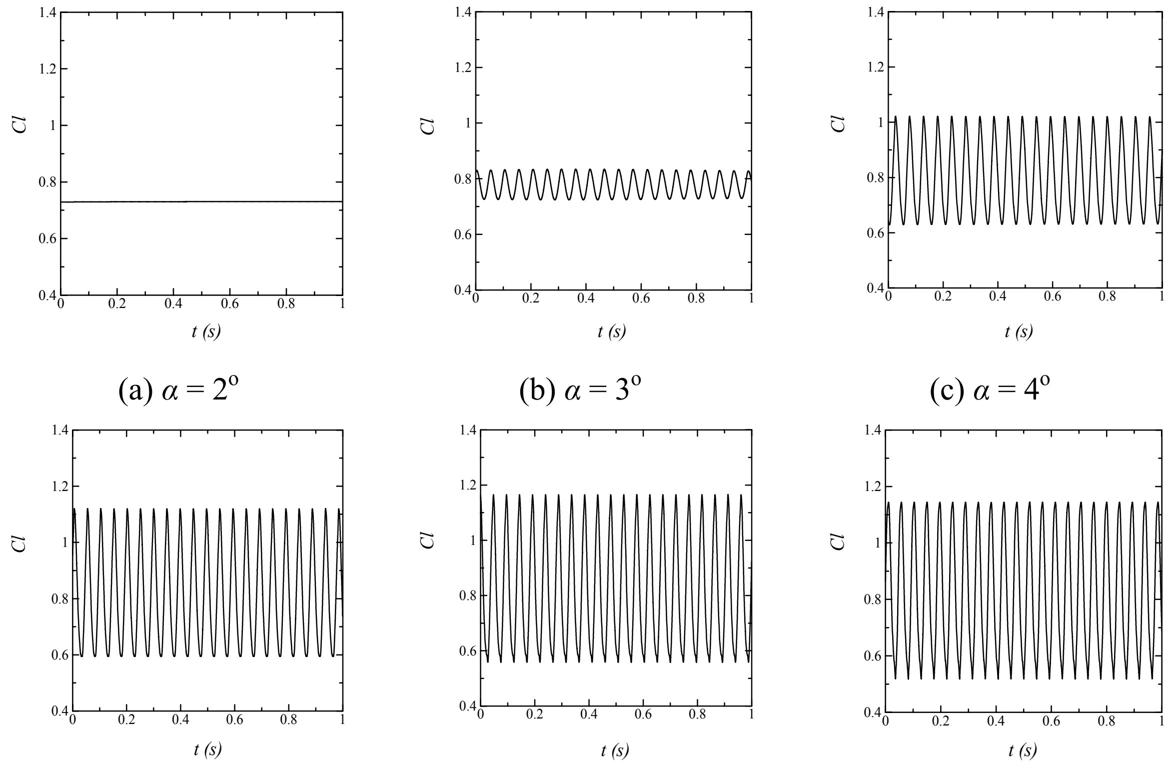

(a) $\alpha = 2^{o}$ (b) $\alpha = 3^{o}$ (c) $\alpha = 4^{o}$

(d) $\alpha = 5^{o}$ (e) $\alpha = 6^{o}$ (f) $\alpha = 7^{o}$

Figure 4.8: Evolution of lift coefficient C_l at $M_\infty = 0.77$; for (a) $\alpha = 2°$, (b) $\alpha = 3°$, (c) $\alpha = 4°$, (d) $\alpha = 5°$, (e) $\alpha = 6°$, (f) $\alpha = 7°$

Drag coefficient results in figure 4.9 also shows that for 2° angle of attack there is steady drag coefficient as there is no buffeting. During 3° angle of attack due to buffet unsteady drag coefficient with little amplitude is observed. Further angle of attack increment increases the fluctuation of drag coefficient. For 3° angle of attack C_d varies from 0.06 to 0.071 with a deviation of 0.005, for 4° it varies from 0.062 to 0.108 with a deviation of 0.023. Again for 5°, 6° and 7° it varies from 0.071 to 0.136, 0.083 to 0.16 and 0.094 to 0.175 with a deviation of 0.033, 0.039 and 0.041 respectively.

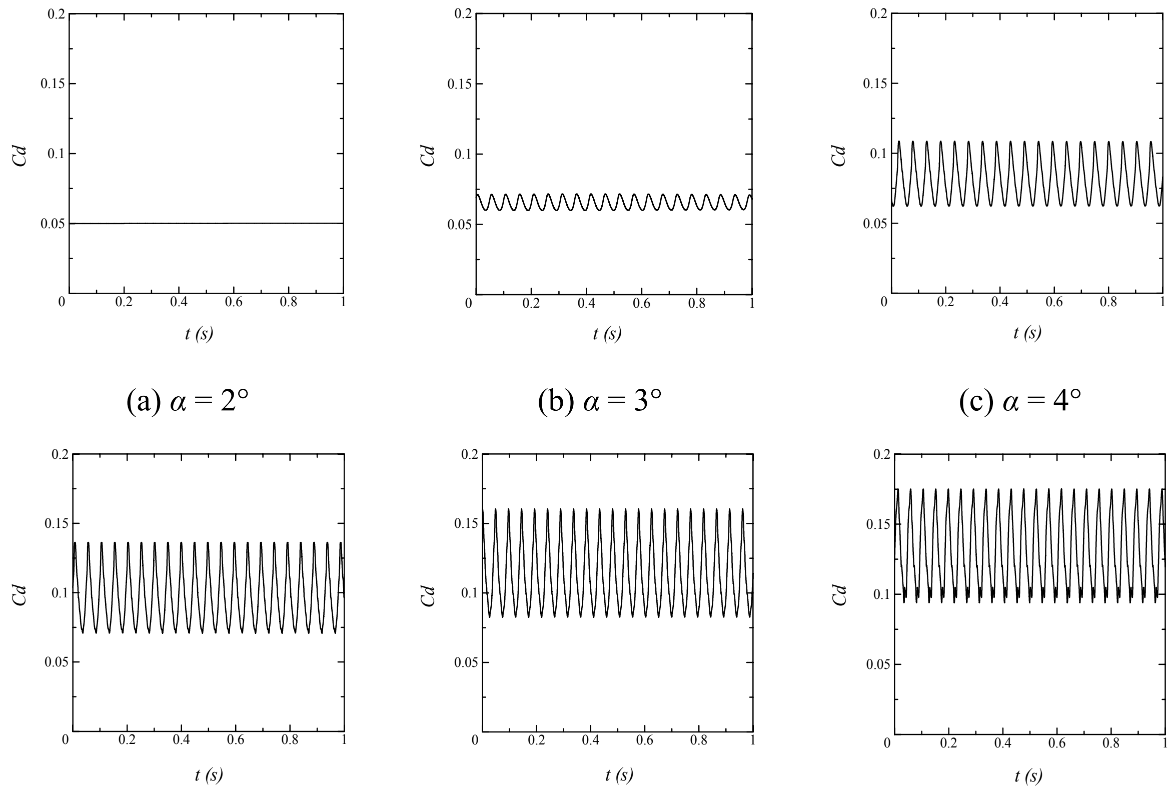

(a) $\alpha = 2°$ (b) $\alpha = 3°$ (c) $\alpha = 4°$

(d) $\alpha = 5°$ (e) $\alpha = 6°$ (f) $\alpha = 7°$

Figure 4.9: Evolution of drag coefficient C_d at $M_\infty = 0.77$; (a) $\alpha = 2°$, (b) $\alpha = 3°$, (c) $\alpha = 4°$, (d) $\alpha = 5°$, (e) $\alpha = 6°$, (f) $\alpha = 7°$

To understand the aerodynamic behavior with different angle of attack the parameters are presented in following table 4.1.

Table 4.1: Comparison of C_l and C_d with different angle of attack for M_∞= 0.77.

Angle of attack	Mean C_l	Deviation from Mean C_l	Mean C_d	Deviation from Mean C_d	Mean C_l/ Mean C_d
2°	0.73	0	0.05	0	14.6
3°	0.7787	0.0491	0.0657	0.0053	11.85
4°	0.826	0.1942	0.0854	0.023	9.672
5°	0.8571	0.2629	0.1036	0.0327	8.276
6°	0.8617	0.3035	0.1215	0.0389	7.091
7°	0.8313	0.3128	0.1345	0.0406	6.18

Due to shock buffeting phenomena there is no steady lift and drag coefficient, it will be convenient to compare this significant parameter by measuring the mean value.

From the above table if we compare the value of mean lift coefficient with increased angle of attack it is observed that from 2° to 6° Mean C_l is increased. However, for 7° value of Mean C_l moves below the value of 5° angle of attack due to huge loss of energy and lift force. Mean C_d value increases with increment of angle of attack of 7°. Deviation from Mean C_l and Mean C_d also shows increased deviation of C_l and C_d with increasing angle of attack.

Ratio of Mean C_l to Mean C_d shows that for steady state condition like for angle of attack 2° it was 14.6. Due to shock buffeting from 3° this value was decreased rather than increase. For other angle of attack it was continuously decreased and for 7° it was lowest.

4.4 Pressure Coefficient Distribution along the Airfoil

Pressure coefficient is a dimensionless number which describes a relative pressure throughout a flow field in fluid dynamics. It is represented as, $Cp = \frac{P - P\infty}{\frac{1}{2}\rho v_{\infty}^{2}}$. Every point in a fluid flow field has its unique pressure coefficient. Pressure coefficient has been represented graphically along the upper and lower surface of airfoil for angle of attack 2°, 3°, 4°, 5°, 6° and 7° with free stream Mach number 0.77.

According to Xiao et al. [25] there are two opposing effects of the shock moving upstream. The upstream movement of the shock, on a quasi steady basis, should lead to a reduction in the shock Mach number and shock induced separation. On a dynamic basis, the movement of the shock upstream should increase the velocity relative to the shock and the shock Mach number, leading to an increase in shock induced separation. The net effect during the upstream motion of shock appears to be that the shock strength slightly reduces and the flow remains separated. The suction side which is upper side of airfoil is composed of three main parts, the supersonic plateau, the spread compression due to the unsteady shock wave and the recompression zone. The pressure side which is the lower side of airfoil is characterized by the rear load caused by the specific airfoil curvature.

4.4.1 Case : Angle of Attack 2°

For 2° angle of attack (figure 4.10) the suction side is composed of two main parts, the supersonic plateau and the recompression zone, the spread compression zone is absent due to the steady shock wave. Supersonic plateau zone extends from leading edge to 56% of chord and the recompression zone extends to the rest of the airfoil surface up to trailing edge. Minimum value of C_p located before shock at 54.6% chord length with a value of -1.234.

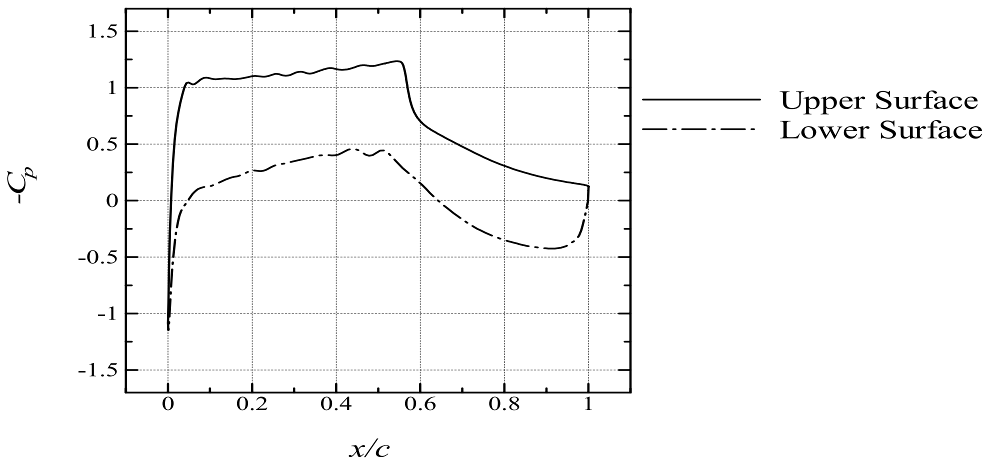

Figure 4.10: C_p distribution on upper and lower surface of airfoil for M_∞= 0.77, α = 2°

4.4.2 Case : Angle of Attack 3°

During one cycle of shock oscillation it is observed from C_p distribution curve (figure 4.11) that from t = 0/10 T time instance value of minimum C_p along upper surface is -1.2956 and it continues to increase. At last time step of forward shock oscillation i.e. t = 5/10 T value of C_p gains highest value along upper surface -1.2907. Due to weak buffeting this C_p value does not change significantly during one oscillation period. For 2° angle of attack value of highest C_p was -1. Which indicates that increased angle of attack decreases highest C_p value. This statement signifies increased lift coefficient with increased angle of attack

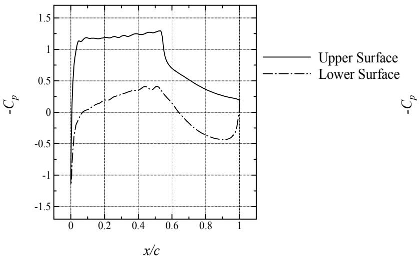

(a) $t = 0/10\ T$

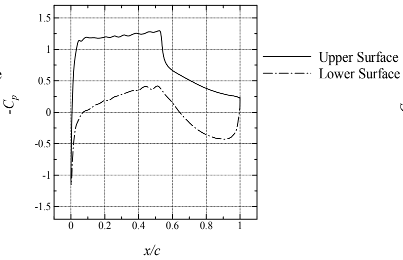

(b) $t = 1/10\ T$

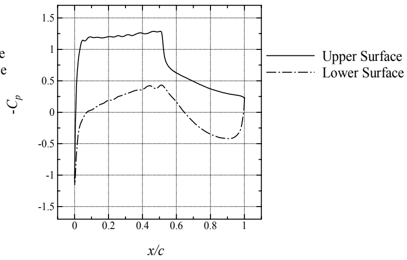

(c) $t = 2/10\ T$

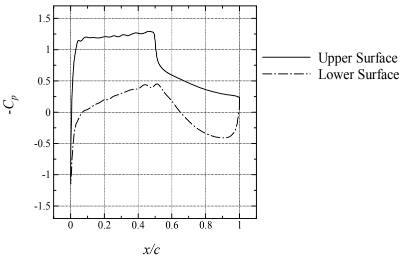

(d) $t = 3/10\ T$

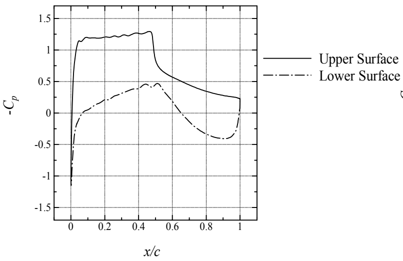

(e) $t = 4/10\ T$

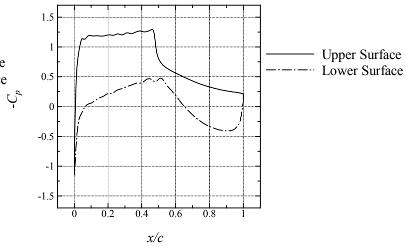

(f) $t = 5/10\ T$

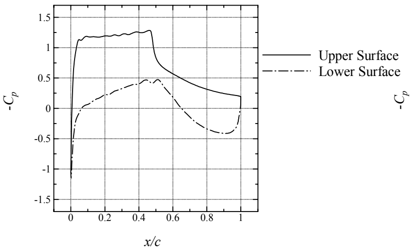

(g) $t = 6/10\ T$

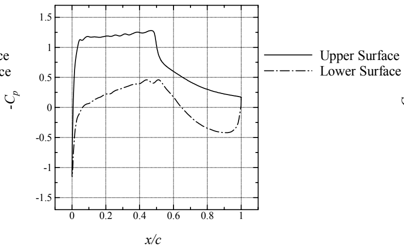

(h) $t = 7/10\ T$

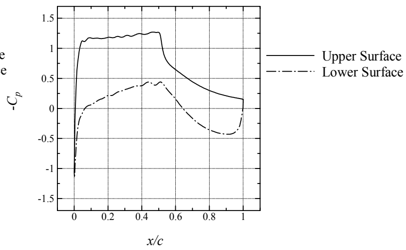

(i) $t = 8/10\ T$

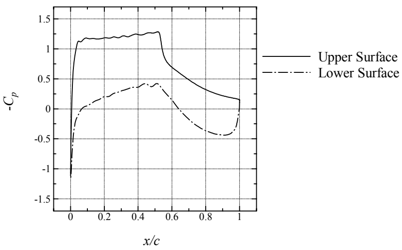

(j) $t = 9/10\ T$

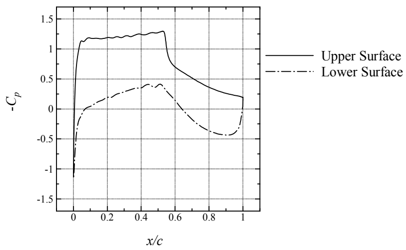

(k) $t = 10/10\ T$

Figure 4.11: C_p distribution during one cycle of flow oscillation, on upper and lower surface of airfoil for $M_\infty = 0.77$, $\alpha = 3°$.

4.4.3 Case : Angle of Attack 4°

During one cycle of shock oscillation it is observed from C_p distribution curve (figure 4.12) that from t = 0/10 T time instance value of minimum C_p along upper surface is -1.3738 and it continues to increase. At last time step of forward shock oscillation i.e. t = 5/10 T value of C_p gains highest value along upper surface -1.318.

Suction side is composed of three parts, the supersonic plateau, the spread compression due to the unsteady shock wave and the recompression zone. Due to forward movement of shock from t = 0/10 T to t = 5/10 T time instances supersonic plateau zone is reduced. This behavior effects on lowest lift coefficient of the cycle. After the rest cycle of oscillation from t = 6/10 T to t = 10/10 T time instances it again gains lowest C_p and increased supersonic plateau zone.

As the value of lift coefficient has a positive relationship between the areas covered by C_p distribution curve, the above figures show a good agreement with lift coefficient of different time instances.

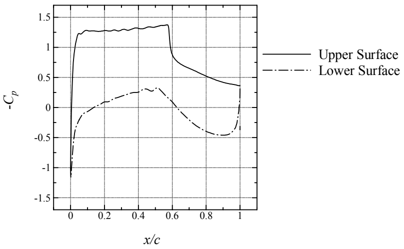

(a) $t = 0/10\ T$

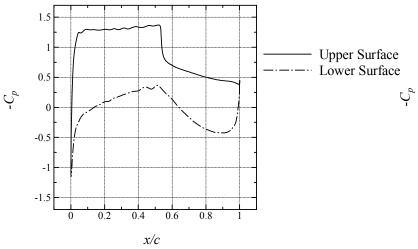

(b) $t = 1/10\ T$

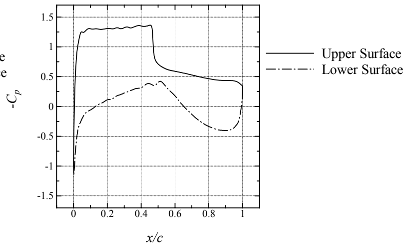

(c) $t = 2/10\ T$

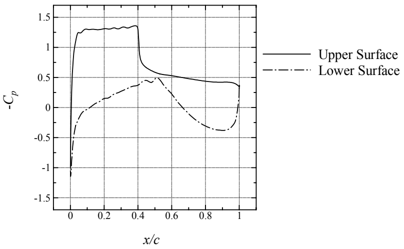

(d) $t = 3/10\ T$

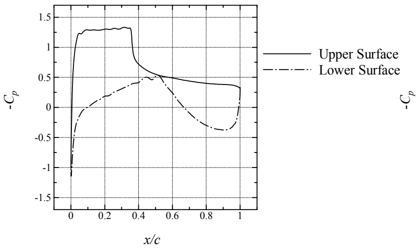

(e) $t = 4/10\ T$

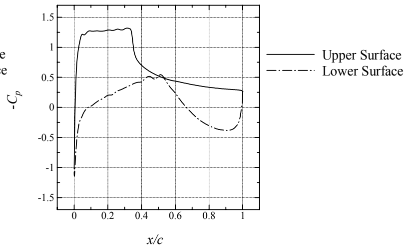

(f) $t = 5/10\ T$

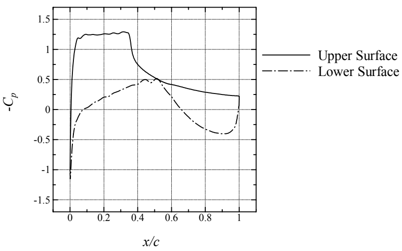

(g) $t= 6/10\ T$

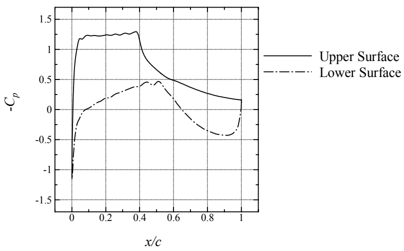

(h) $t = 7/10\ T$

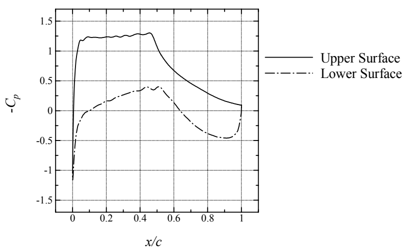

(i) $t = 8/10\ T$

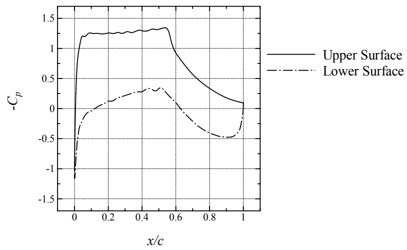

(j) $t = 9/10\ T$

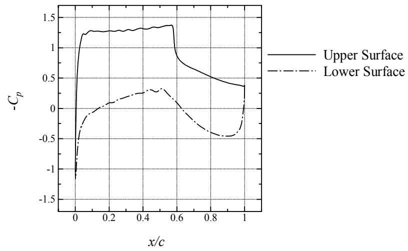

(k) $t = 10/10\ T$

Figure 4.12: C_p distribution during one cycle of flow oscillation*,* on upper and lower surface of airfoil for $M_\infty = 0.77$, $\alpha = 4°$.

4.4.4 Case : Angle of Attack 5°

During one cycle of shock oscillation it is observed from C_p distribution curve (figure 4.13) that from t = 0/10 T time instance value of minimum C_p along upper surface is -1.427 and it continues to increase. At last time step of forward shock oscillation i.e. t = 5/10 T value of C_p gains highest value along upper surface -1.37. For 4° angle of attack value of highest C_p was -1.3738 and -1.318 for t = 0/10 T and t = 5/10 T time step respectively. Which indicates that increased angle of attack decreases highest C_p value. This statement signifies increased lift coefficient with increased angle of attack

For this case also suction side is composed of three parts, the supersonic plateau, the spread compression due to the unsteady shock wave and the recompression zone. Due to forward movement of shock from t = 0/10 T to t = 5/10 T time instances supersonic plateau zone is reduced. This behavior effects on lowest lift coefficient of the cycle. After the rest cycle of oscillation from t = 6/10 T to t = 10/10 T time instances it again gains lowest C_p and increased supersonic plateau zone.

The above figures also show a good agreement between the value of lift coefficient and the area covered by C_p distribution curve for different time instances.

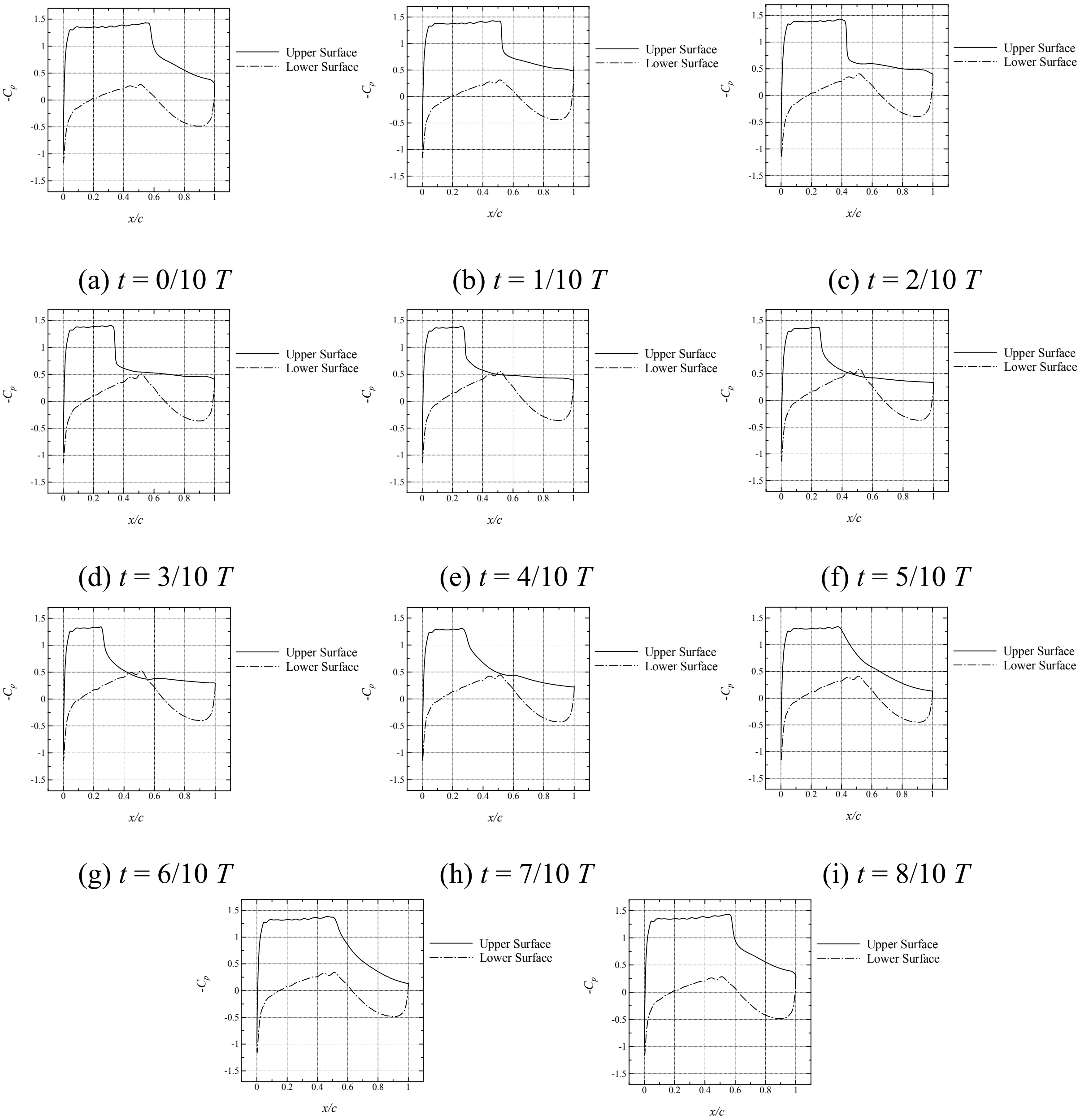

(a) $t = 0/10\ T$ (b) $t = 1/10\ T$ (c) $t = 2/10\ T$

(d) $t = 3/10\ T$ (e) $t = 4/10\ T$ (f) $t = 5/10\ T$

(g) $t = 6/10\ T$ (h) $t = 7/10\ T$ (i) $t = 8/10\ T$

(j) $t = 9/10\ T$ (k) $t = 10/10\ T$

Figure 4.13: C_p distribution during one cycle of flow oscillation, on upper and lower surface of airfoil for $M_\infty = 0.77$, $\alpha = 5°$.

4.4.5 Case : Angle of Attack 6°

During one cycle of shock oscillation it is observed from C_p distribution curve (figure 4.14) that from t = 0/10 T time instance value of minimum C_p along upper surface is -1.472and it continues to increase. At last time step of forward shock oscillation i.e. t = 5/10 T value of C_p gains highest value along upper surface -1.416. For 5° angle of attack value of highest C_p was -1.427and -1.37 for t = 0/10 T and t = 5/10 T time step respectively. Which indicates that increased angle of attack decreases highest C_p value. This statement signifies increased lift coefficient with increased angle of attack

Here also suction side is composed of three parts, the supersonic plateau, the spread compression due to the unsteady shock wave and the recompression zone. Due to forward movement of shock from t = 0/10 T to t = 5/10 T time instances supersonic plateau zone is reduced. This behavior effects on lowest lift coefficient of the cycle. After the rest cycle of oscillation from t = 6/10 T to t = 10/10 T time instances it again gains lowest C_p and increased supersonic plateau zone.

The above figures also show a good agreement between the value of lift coefficient and the area covered by C_p distribution curve for different time instances.

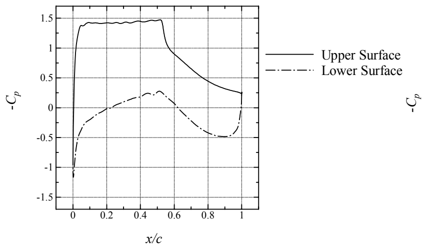

(a) $t = 0/10\ T$

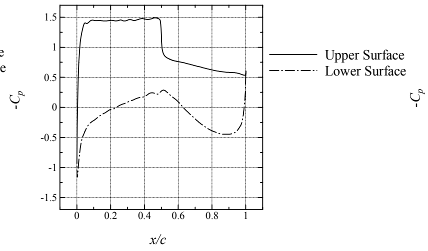

(b) $t = 1/10\ T$

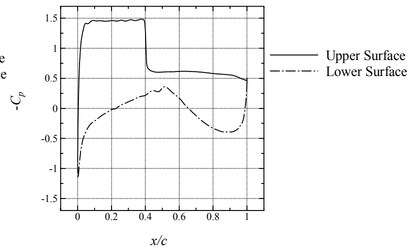

(c) $t = 2/10\ T$

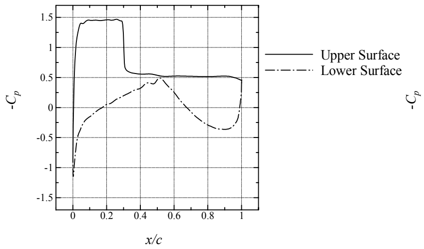

(d) $t= 3/10\ T$

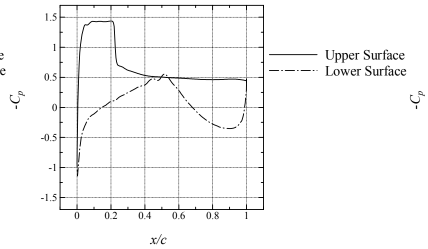

(e) $t = 4/10\ T$

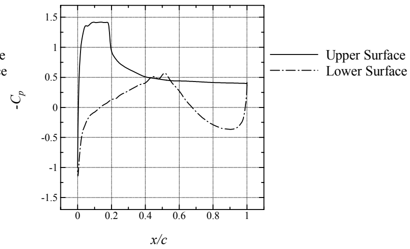

(f) $t = 5/10\ T$

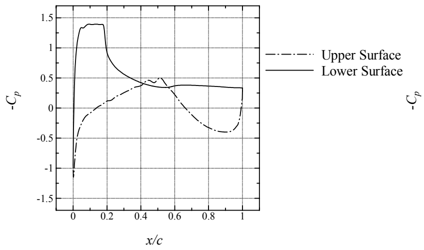

(g) $t = 6/10\ T$

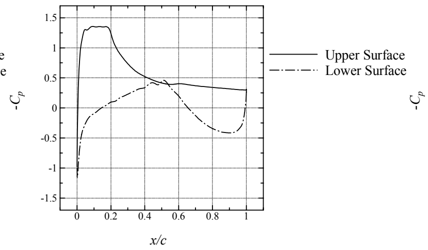

(h) $t = 7/10\ T$

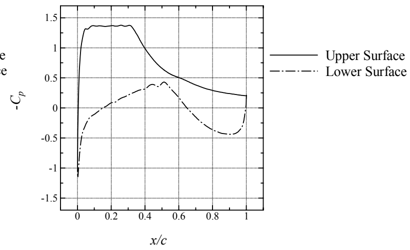

(i) $t = 8/10\ T$

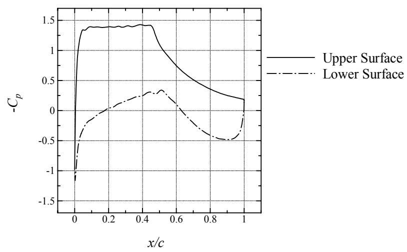

(j) $t = 9/10\ T$

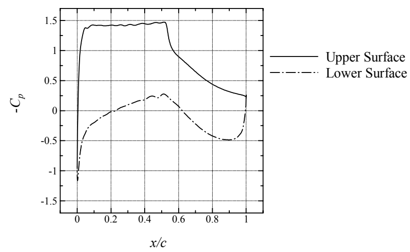

(k) $t = 10/10\ T$

Figure 4.14: C_p distribution during one cycle of flow oscillation, on upper and lower surface of airfoil for $M_\infty= 0.77$, $\alpha = 6°$.

4.4.6 Case : Angle of Attack 7°

During one cycle of shock oscillation it is observed from C_p distribution curve (figure 4.15) that from t = 0/10 T time instance value of minimum C_p along upper surface is -1.536 and it continues to increase. At last time step of forward shock oscillation i.e. t = 5/10 T time instance value of C_p gains highest value along upper surface -1.459. For 6° angle of attack value of highest C_p was -1.472 and -1.416 for t = 0/10 T and t = 5/10 T time step respectively. Which indicates that increased angle of attack decreases highest C_p value. This statement signifies increased lift coefficient with increased angle of attack

For this situation also suction side is composed of three parts, the supersonic plateau, the spread compression due to the unsteady shock wave and the recompression zone. Due to forward movement of shock from t = 0/10 T to t = 5/10 T time instances supersonic plateau zone is reduced. This behavior effects on lowest lift coefficient of the cycle. After the rest cycle of oscillation from t = 6/10 T to t = 10/10 T time instances it again gains lowest C_p and increased supersonic plateau zone.

For this case the above figures also show a good agreement between the value of lift coefficient and the area covered by C_p distribution curve for different time instances.

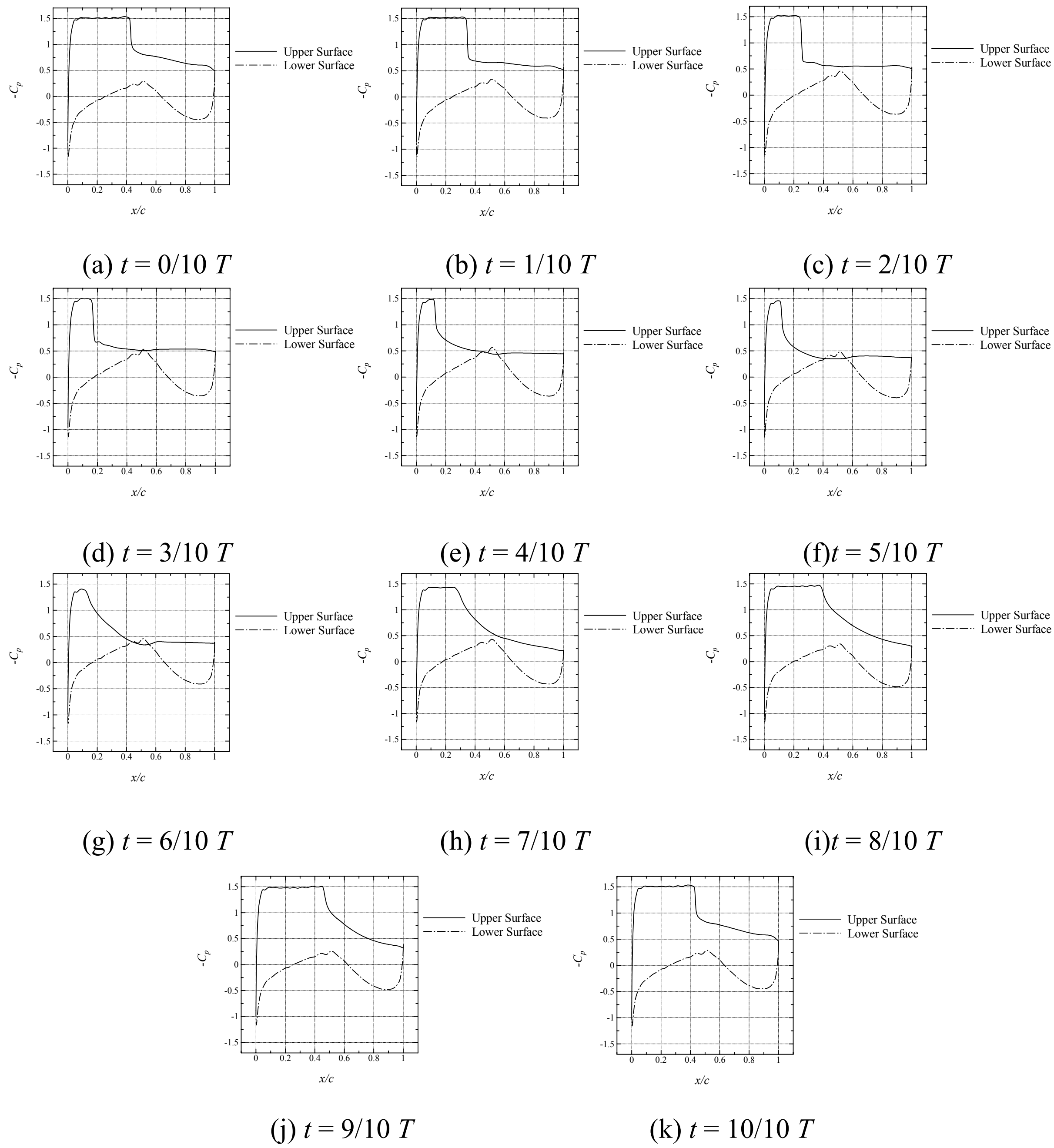

(a) t = 0/10 T (b) t = 1/10 T (c) t = 2/10 T

(d) t = 3/10 T (e) t = 4/10 T (f)t = 5/10 T

(g) t = 6/10 T (h) t = 7/10 T (i)t = 8/10 T

(j) t = 9/10 T (k) t = 10/10 T

Figure 4.15: C_p distribution during one cycle of flow oscillation, on upper and lower surface of airfoil for M_∞= 0.77, α = 7°.

4.5 Pressure History on Upper Surface of Airfoil

24 positions have been allocated along the upper surface of the airfoil. All static pressure (*P*) has been converted non-dimensional by dividing with atmospheric pressure (P_0). Non dimensional static pressure (P/P_0) through the positions have been represented graphically during 1second time period cycle.

4.5.1 Case : Angle of Attack 3°

Pressure history on upper surface of airfoil for 3° angle of attack is shown in figure 4.16. For angle of attack 3° mean value of dimensionless static pressure at leading edge is found 1.449 with 0.18% deviation from mean value which drops slowly below atmospheric pressure due to airfoil shape and creates low pressure region on upper surface of airfoil with low oscillation upto 45% of chord length. At 47.5% of chord location deviation of P/P_0 happens significantly which is 4.95 % of its mean value. At 52.5% of chord length deviation of P/P_0 from its mean value is 21.21% which is maximum for this case and this deviation decreases upto trailing edge. Frequency of oscillation is found 19.04 Hz.

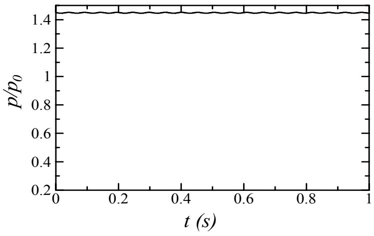

(a) $x/c = 0$

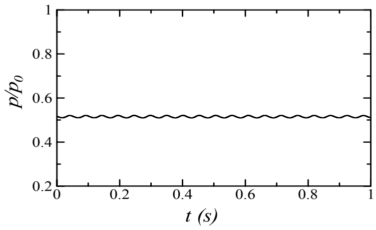

(b) $x/c = 0.1$

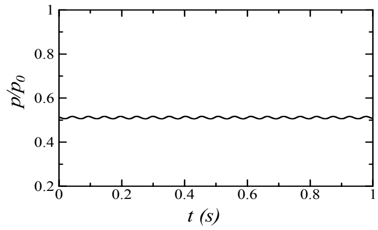

(c) $x/c = 0.2$

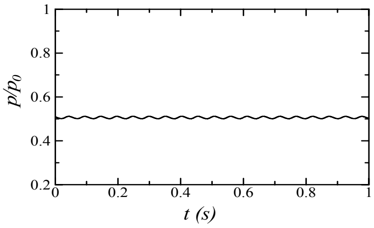

(d) $x/c = 0.25$

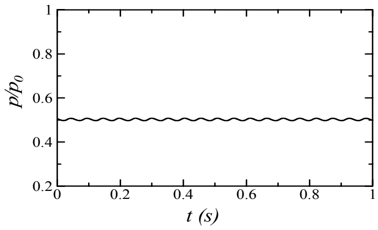

(e) $x/c = 0.3$

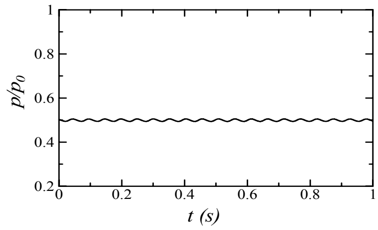

(f) $x/c = 0.325$

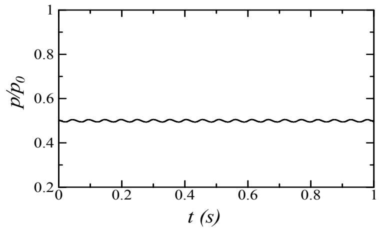

(g) $x/c = 0.35$

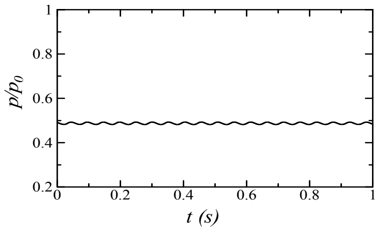

(h) $x/c = 0.375$

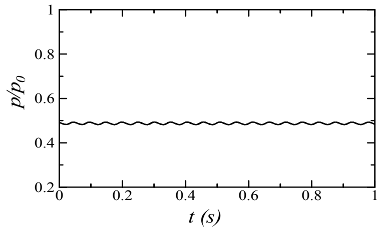

(i) $x/c = 0.4$

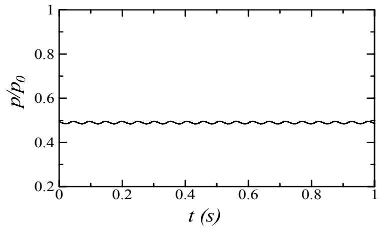

(j) $x/c = 0.425$

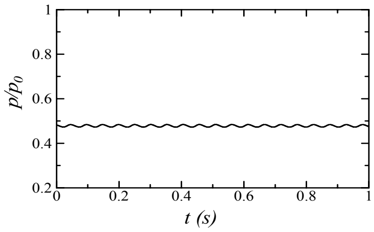

(k) $x/c = 0.45$

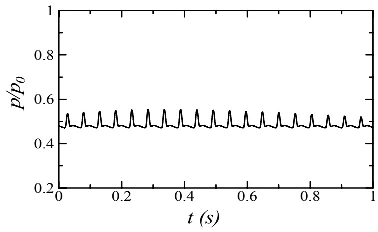

(l) $x/c = 0.475$

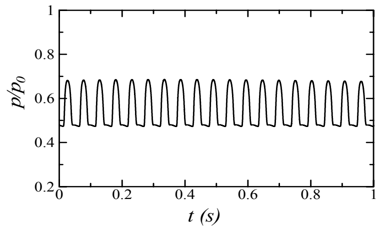

(m) $x/c = 0.5$

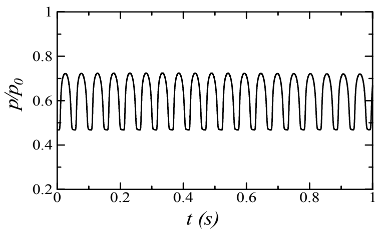

(n) $x/c = 0.525$

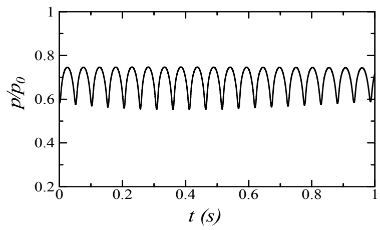

(o) $x/c = 0.55$

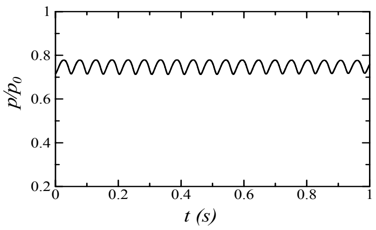

(p) x/c = 0.6

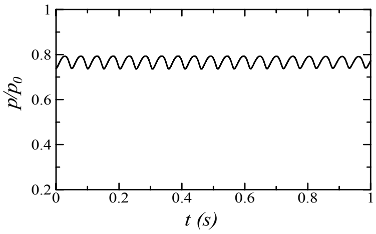

(q) x/c = 0.625

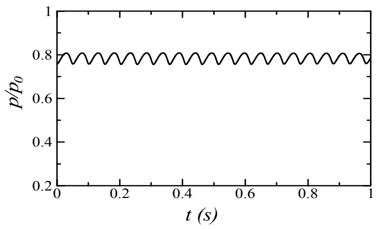

(r) x/c = 0.65

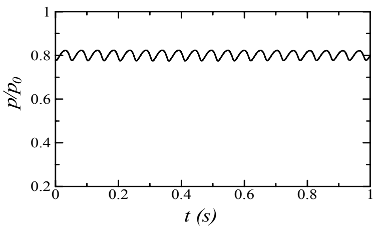

(s) x/c = 0.675

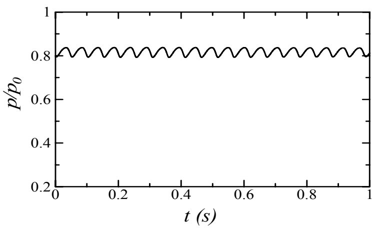

(t) x/c = 0.7

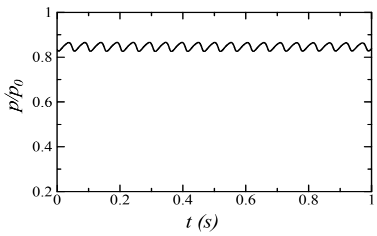

(u) x/c = 0.75

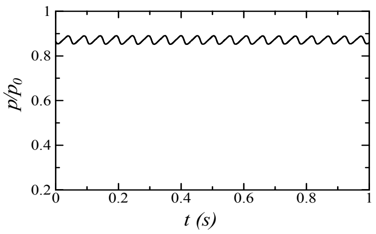

(v) x/c = 0.8

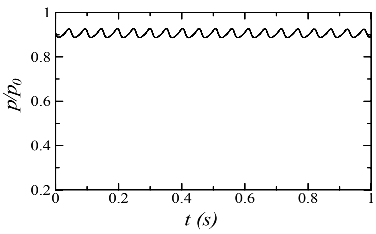

(w) x/c = 0.9

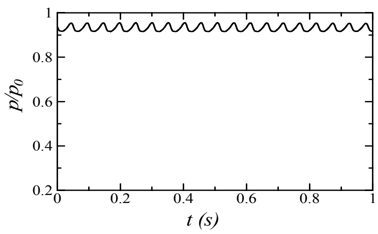

(x) x/c = 1

Figure 4.16: Non dimensional static pressure time histories at the upper surface of the airfoil for the conditions $M_\infty = 0.77$, $\alpha = 3°$along the positions (a) x/c = 0, (b) x/c = 0.1, (c) x/c = 0.2, (d) x/c = 0.25, (e) x/c = 0.3, (f) x/c = 0.325, (g) x/c = 0.35, (h) x/c = 0.375, (i) x/c = 0.4, (j) x/c = 0.425, (k) x/c = 0.45, (l) x/c = 0.475, (m) x/c = 0.5, (n) x/c = 0.525, (o) x/c = 0.55, (p) x/c = 0.6, (q) x/c = 0.625, (r) x/c = 0.65, (s) x/c = 0.675, (t) x/c = 0.7, (u) x/c = 0.75, (v) x/c = 0.8, (w) x/c = 0.9, (x) x/c = 1.

4.5.2 Case : Angle of Attack 4°

Pressure history on upper surface of airfoil for 4° angle of attack is shown in figure 4.17. For angle of attack 4° mean value of dimensionless static pressure at leading edge is found 1.433 with 0.65% deviation from mean value which drops slowly below atmospheric pressure due to airfoil shape and creates low pressure region on upper surface of airfoil with low oscillation upto 32.5% of chord length. At 35% of chord location deviation of P/P_0 happens significantly which is 12 % of its mean value. At 55% of chord length deviation of P/P_0 from its mean value is 30.63% which is maximum for this case and this deviation decreases upto trailing edge. Frequency of oscillation is found 19.31 Hz which was 19.04 Hz for 3° angle of attack. So, it is seen that due to increased angle of attack frequency of oscillation also increases.

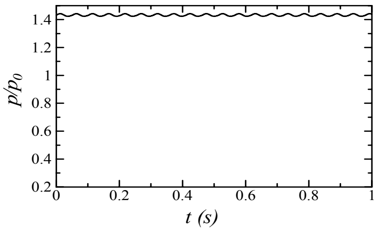

(a) $x/c = 0$

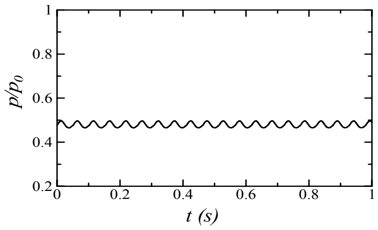

(b) $x/c = 0.1$

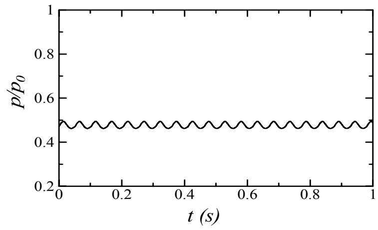

(c) $x/c = 0.2$

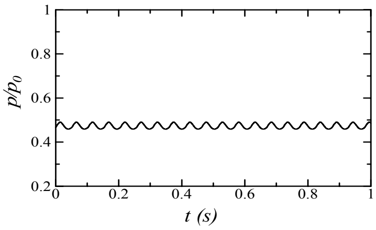

(d) x/c = 0.25

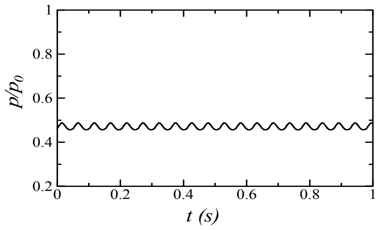

(e) $x/c = 0.3$

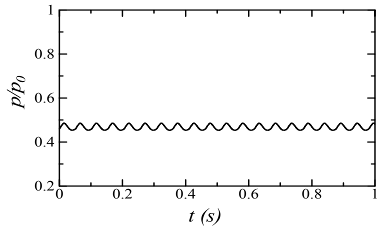

(f) $x/c = 0.325$

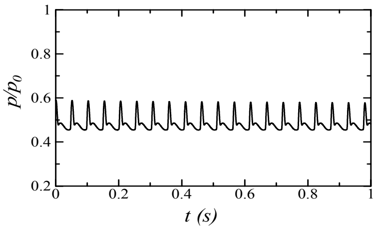

(g) $x/c = 0.35$

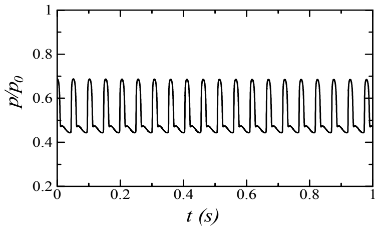

(h) $x/c = 0.375$

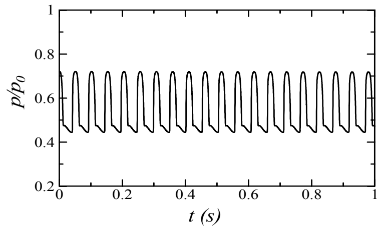

(i) $x/c = 0.4$

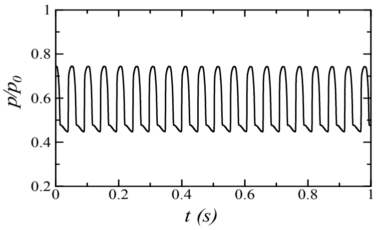

(j) $x/c = 0.425$

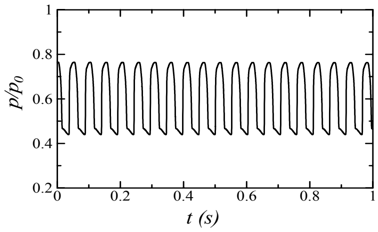

(k) $x/c = 0.45$

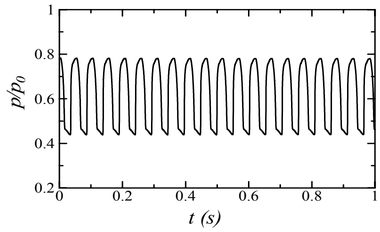

(l) $x/c = 0.475$

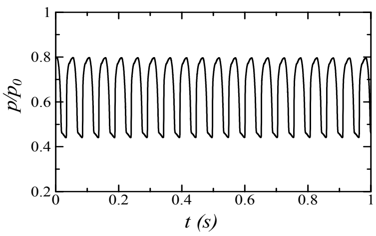

(m) $x/c = 0.5$

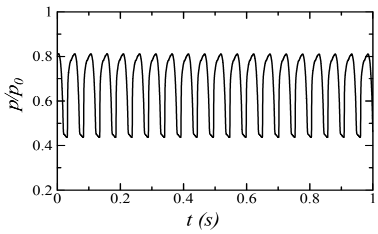

(n) $x/c = 0.525$

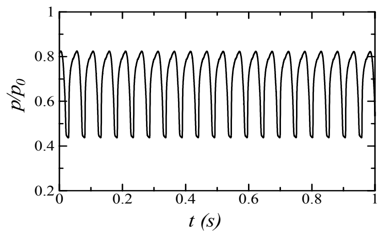

(o) $x/c = 0.55$

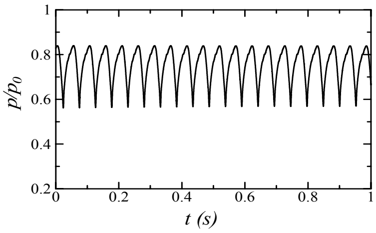

(p) x/c = 0.6

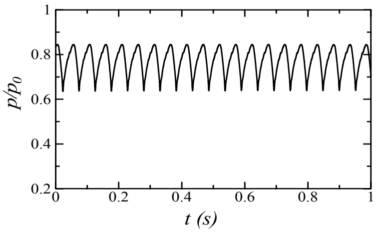

(q) x/c = 0.625

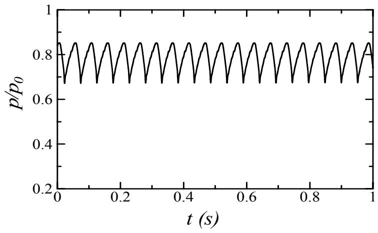

(r) x/c = 0.65

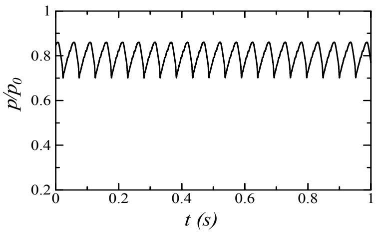

(s) x/c = 0.675

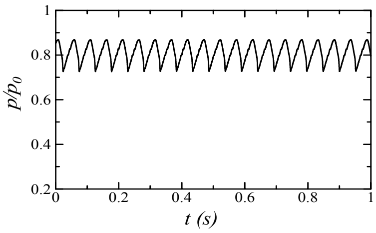

(t) x/c = 0.7

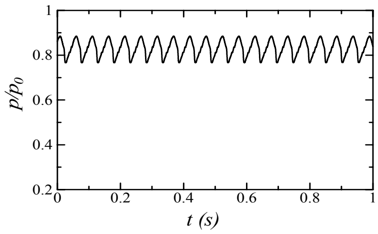

(u) x/c = 0.75

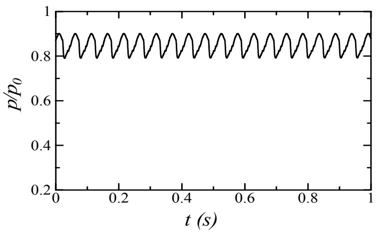

(v) x/c = 0.8

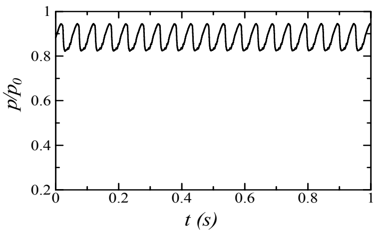

(w) x/c = 0.9

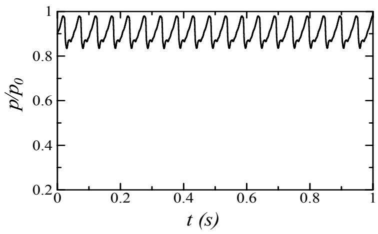

(x) x/c = 1

Figure 4.17: Non dimensional static pressure time histories at the upper surface of the airfoil for the conditions M_∞ = 0.77, α = 4°along the positions (a) x/c = 0, (b) x/c = 0.1, (c) x/c = 0.2, (d) x/c = 0.25, (e) x/c = 0.3, (f) x/c = 0.325, (g) x/c = 0.35, (h) x/c = 0.375, (i) x/c = 0.4, (j) x/c = 0.425, (k) x/c = 0.45, (l) x/c = 0.475, (m) x/c = 0.5, (n) x/c = 0.525, (o) x/c = 0.55, (p) x/c = 0.6, (q) x/c = 0.625, (r) x/c = 0.65, (s) x/c = 0.675, (t) x/c = 0.7, (u) x/c = 0.75, (v) x/c = 0.8, (w) x/c = 0.9, (x) x/c = 1.

4.5.3 Case : Angle of Attack 5°

Pressure history on upper surface of airfoil for 5° angle of attack is shown in figure 4.18. For angle of attack 5° mean value of dimensionless static pressure at leading edge is found 1.416 with 0.97% deviation from mean value which drops slowly below atmospheric pressure due to airfoil shape and creates low pressure region on upper surface of airfoil with low oscillation upto 25% of chord length. At 30% of chord location deviation of P/P_0 happens significantly which is 24.06 % of its mean value. At 55% of chord length deviation of P/P_0 from its mean value is 35.21% which is maximum for this case and this deviation decreases upto trailing edge. Frequency of oscillation is found 20.45 Hz which was 19.31 Hz for 4° angle of attack. In this case also due to increased angle of attack frequency of oscillation also increases.

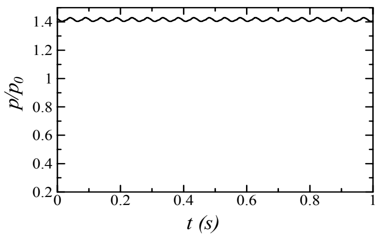

(a) x/c = 0

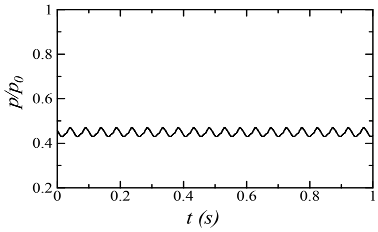

(b) x/c = 0.1

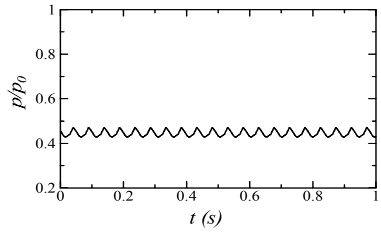

(c) x/c = 0.2

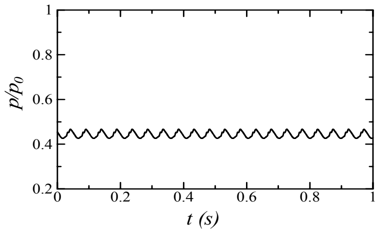

(d) x/c = 0.25

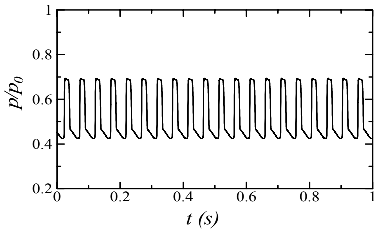

(e) x/c = 0.3

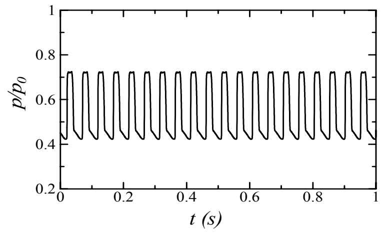

(f) x/c = 0.325

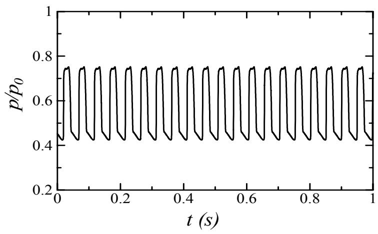

(g) x/c = 0.35

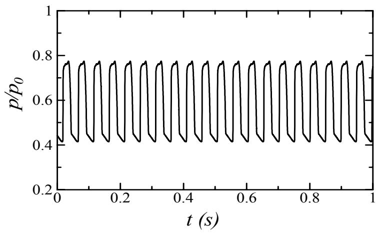

(h) x/c = 0.375

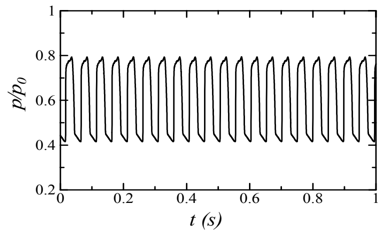

(i) x/c = 0.4

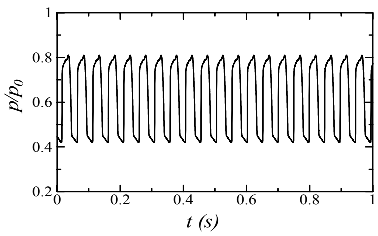

(j) x/c = 0.425

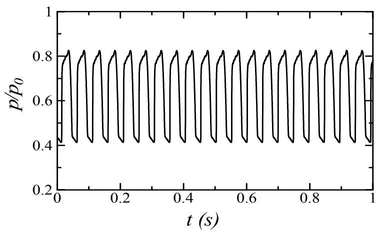

(k) x/c = 0.45

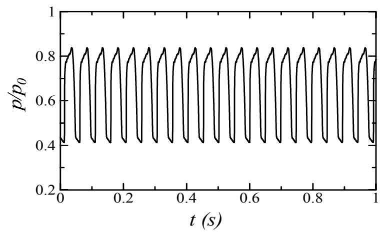

(l) x/c = 0.475

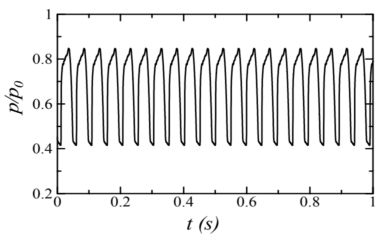

(m) x/c = 0.5

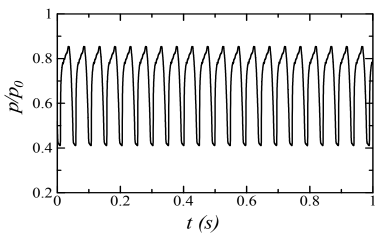

(n) x/c = 0.525

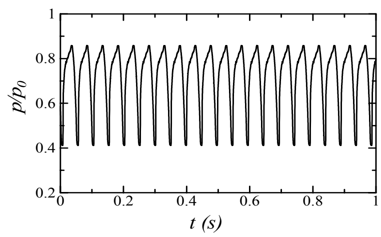

(o) x/c = 0.55

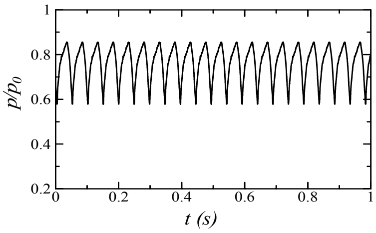

(p) x/c = 0.6

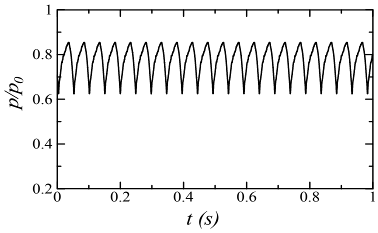

(q) x/c = 0.625

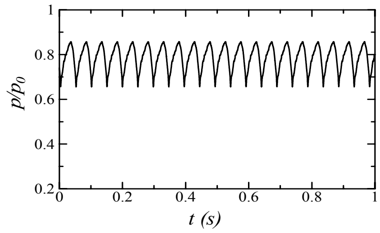

(r) x/c = 0.65

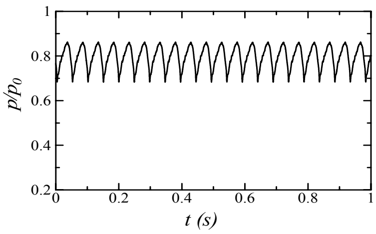

(s) x/c = 0.675

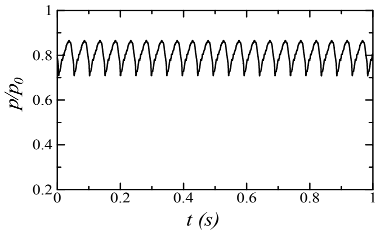

(t) x/c = 0.7

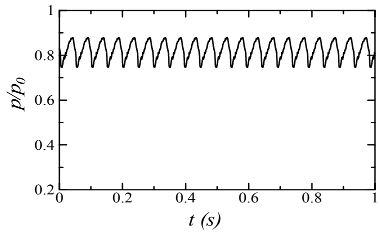

(u) x/c = 0.75

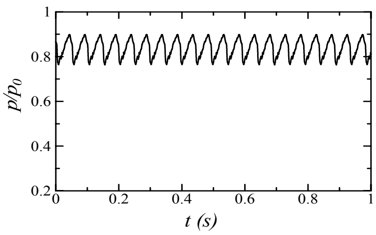

(v) x/c = 0.8

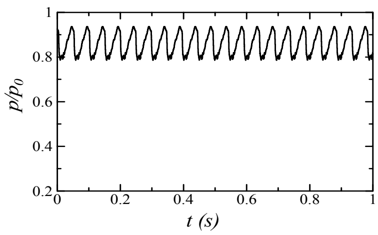

(w) x/c = 0.9

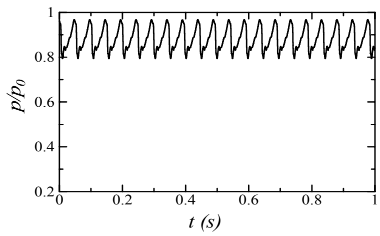

(x) x/c = 1

Figure 4.18: Non dimensional static pressure time histories at the upper surface of the airfoil for the conditions M_∞= 0.77, α = 5^{o} along the positions (a) x/c = 0, (b) x/c = 0.1, (c) x/c = 0.2, (d) x/c = 0.25, (e) x/c = 0.3, (f) x/c = 0.325, (g) x/c = 0.35, (h) x/c = 0.375, (i) x/c = 0.4, (j) x/c = 0.425, (k) x/c = 0.45, (l) x/c = 0.475, (m) x/c = 0.5, (n) x/c = 0.525, (o) x/c = 0.55, (p) x/c = 0.6, (q) x/c = 0.625, (r) x/c = 0.65, (s) x/c = 0.675, (t) x/c = 0.7, (u) x/c = 0.75, (v) x/c = 0.8, (w) x/c = 0.9, (x) x/c = 1.

4.5.4 Case : Angle of Attack 6°

Pressure history on upper surface of airfoil for 6° angle of attack is shown in figure 4.19. For angle of attack 6° mean value of dimensionless static pressure at leading edge is found 1.398 with 1.26% deviation from mean value which drops slowly below atmospheric pressure due to airfoil shape and creates low pressure region on upper surface of airfoil with low oscillation upto 10% of chord length. At 20% of chord location deviation of P/P_0 happens significantly which is 25.59 % of its mean value. At 52.5% of chord length deviation of P/P_0 from its mean value is 37.91% which is maximum for this case and this deviation decreases upto trailing edge. Frequency of oscillation is found 20.79 Hz which was 20.45 Hz for 5°angle of attack. In this case also due to increased angle of attack frequency of oscillation also increases.

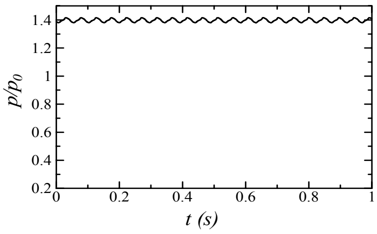

(a) x/c = 0

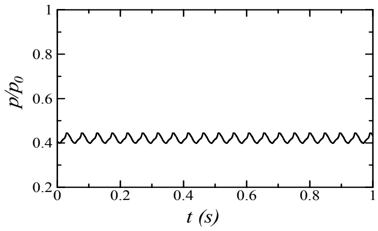

(b) x/c = 0.1

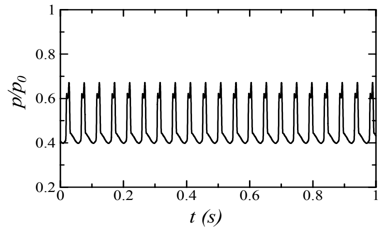

(c) x/c = 0.2

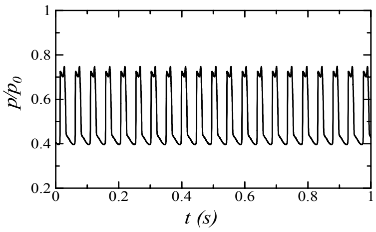

(d) x/c = 0.25

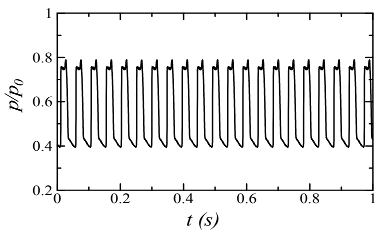

(e) x/c = 0.3

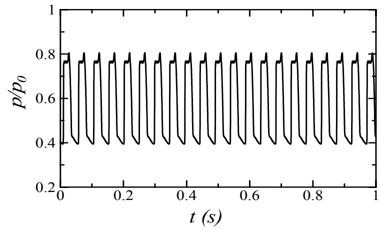

(f) x/c = 0.325

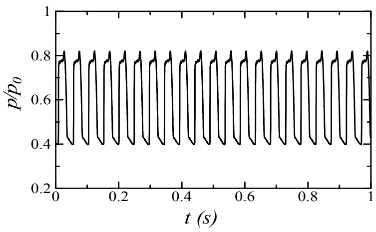

(g) x/c = 0.35

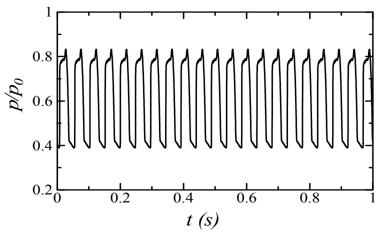

(h) x/c = 0.375

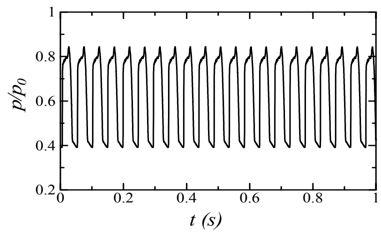

(i) x/c = 0.4

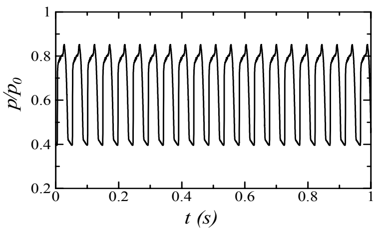

(j) x/c = 0.425

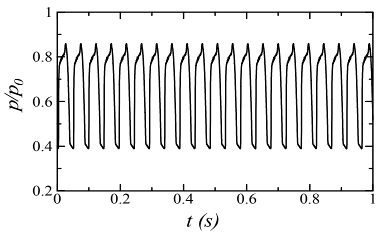

(k) x/c = 0.45

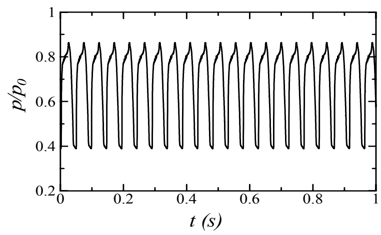

(l) x/c = 0.475

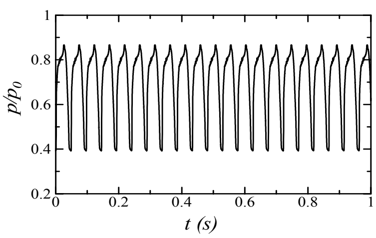

(m) x/c = 0.5

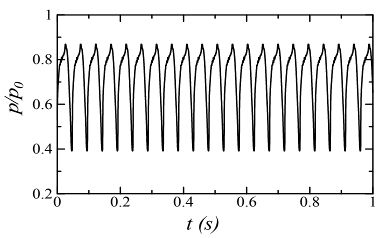

(n) x/c = 0.525

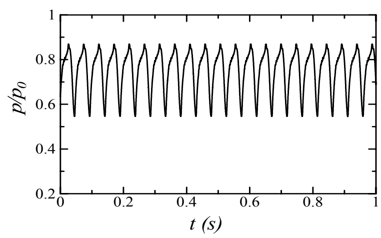

(o) x/c = 0.55

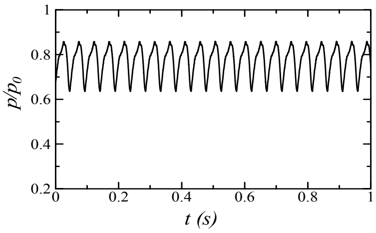

(p) x/c = 0.6

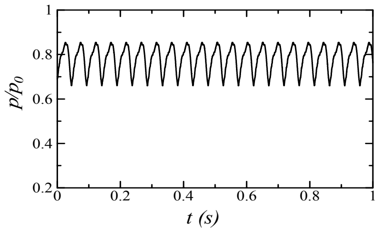

(q) x/c = 0.625

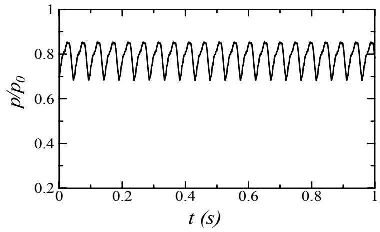

(r) x/c = 0.65

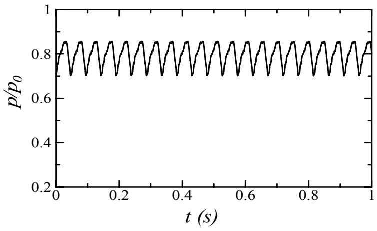

(s) x/c = 0.675

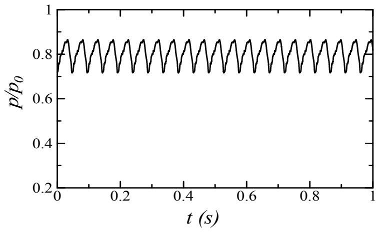

(t) x/c = 0.7

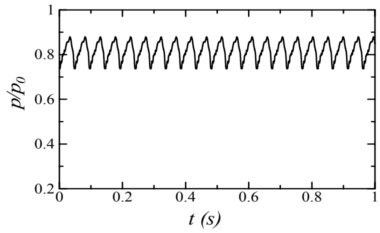

(u) x/c = 0.75

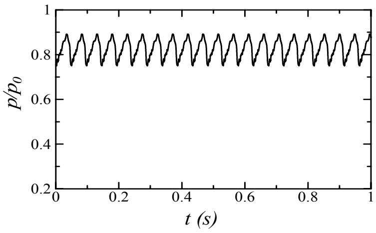

(v) x/c = 0.8

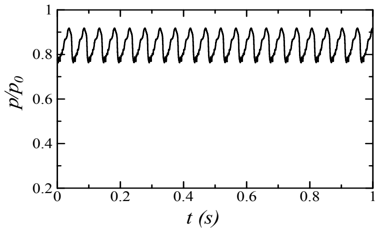

(w) x/c = 0.9

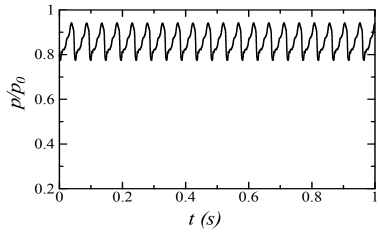

(x) x/c = 1

Figure 4.19: Non dimensional static pressure time histories at the upper surface of the airfoil for the conditions $M_\infty = 0.77$, $\alpha = 6°$ along the positions (a) x/c = 0, (b) x/c = 0.1, (c) x/c = 0.2, (d) x/c = 0.25, (e) x/c = 0.3, (f) x/c = 0.325, (g) x/c = 0.35, (h) x/c = 0.375, (i) x/c = 0.4, (j) x/c = 0.425, (k) x/c = 0.45, (l) x/c = 0.475, (m) x/c = 0.5, (n) x/c = 0.525, (o) x/c = 0.55, (p) x/c = 0.6, (q) x/c = 0.625, (r) x/c = 0.65, (s) x/c = 0.675, (t) x/c = 0.7, (u) x/c = 0.75, (v) x/c = 0.8, (w) x/c = 0.9, (x) x/c = 1.

4.5.5 Case : Angle of Attack 7°

Pressure history on upper surface of airfoil for 7° angle of attack is shown in figure 4.20. For angle of attack 7° mean value of dimensionless static pressure at leading edge is found 1.381 with 1.52% deviation from mean value which drops slowly below atmospheric pressure due to airfoil shape and creates low pressure region on upper surface of airfoil with low oscillation upto 10% of chord length. At 20% of chord location deviation of P/P_0 happens significantly which is 36.22 % of its mean value. At 37.5% of chord length deviation of P/P_0 from its mean value is 39.96% which is maximum for this case and this deviation decreases upto trailing edge. Frequency of oscillation is found 21.55 Hz which was 20.79 Hz for 5°angle of attack. In this case also due to increased angle of attack frequency of oscillation also increases.

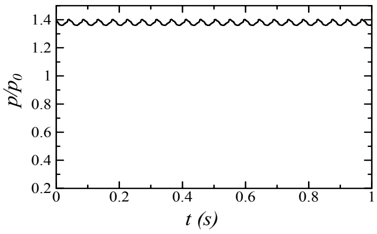

(a) $x/c = 0$

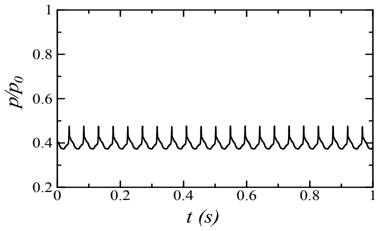

(b) $x/c = 0.1$

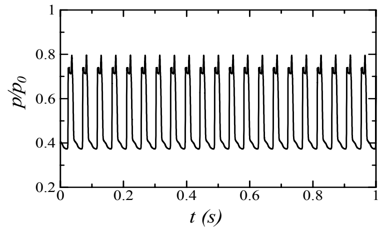

(c) $x/c = 0.2$

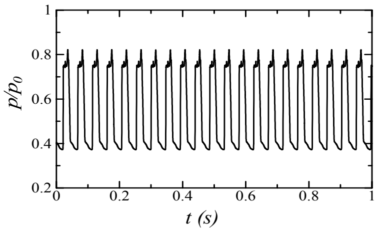

(d) $x/c = 0.25$

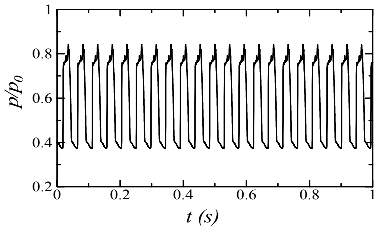

(e) $x/c = 0.3$

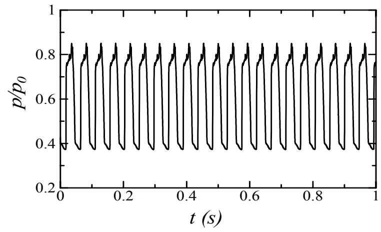

(f) $x/c = 0.325$

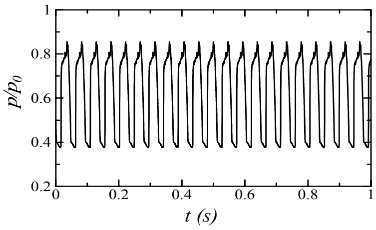

(g) $x/c = 0.35$

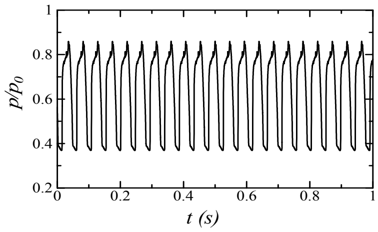

(h) $x/c = 0.375$

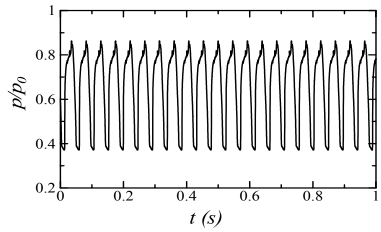

(i) $x/c = 0.4$

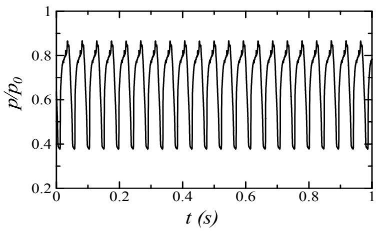

(j) $x/c = 0.425$

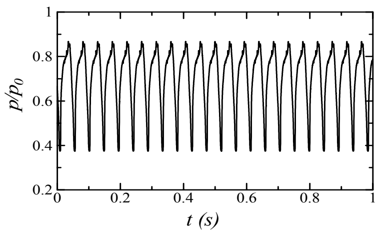

(k) $x/c = 0.45$

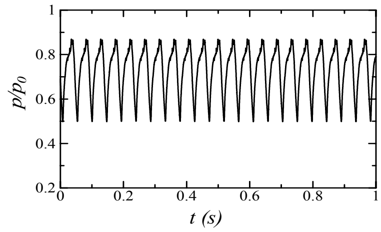

(l) $x/c = 0.475$

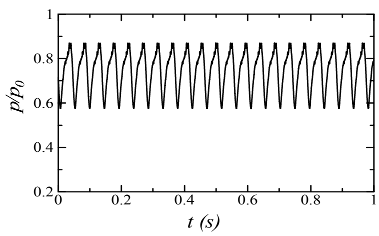

(m) $x/c = 0.5$

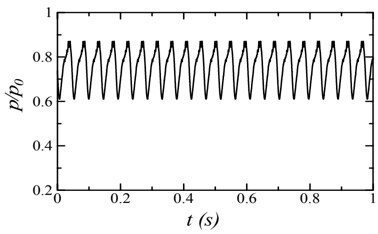

(n) $x/c = 0.525$

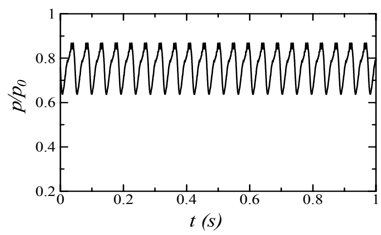

(o) $x/c = 0.55$

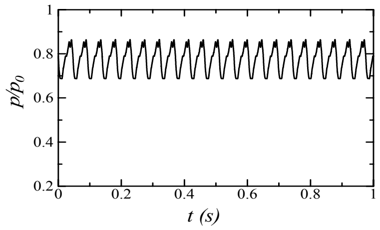

(p) $x/c = 0.6$

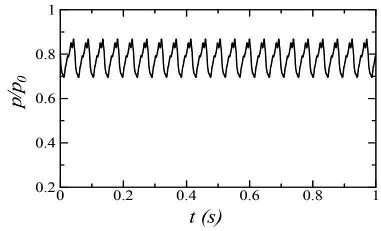

(q) $x/c = 0.625$

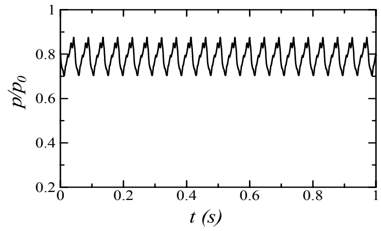

(r) $x/c = 0.65$

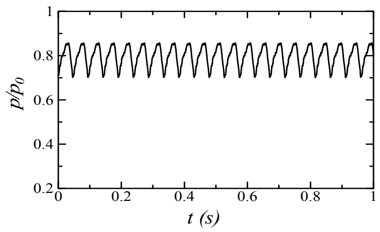

(s) $x/c = 0.675$

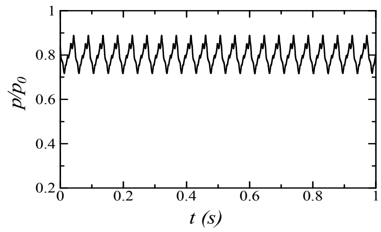

(t) $x/c = 0.7$

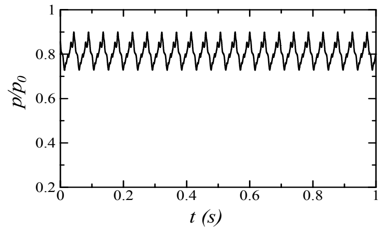

(u) $x/c = 0.75$

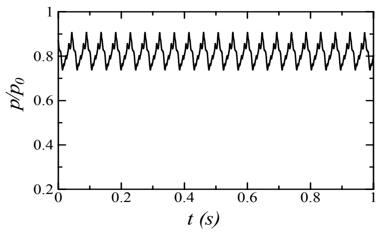

(v) $x/c = 0.8$

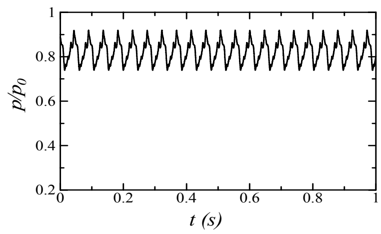

(w) $x/c = 0.9$

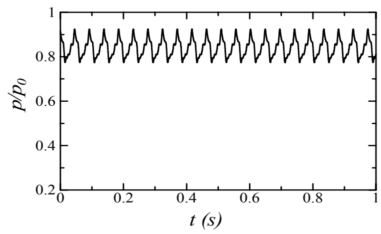

(x) $x/c = 1$

Figure 4.20: Non dimensional static pressure time histories at the upper surface of the airfoil for the conditions $M_\infty = 0.77$, $\alpha = 7°$ along the positions(a) $x/c = 0$, (b) $x/c = 0.1$, (c) $x/c = 0.2$, (d) $x/c = 0.25$, (e) $x/c = 0.3$, (f) $x/c = 0.325$, (g) $x/c = 0.35$, (h) $x/c = 0.375$, (i) $x/c = 0.4$, (j) $x/c = 0.425$, (k) $x/c = 0.45$, (l) $x/c = 0.475$, (m) $x/c = 0.5$, (n) $x/c = 0.525$, (o) $x/c = 0.55$, (p) $x/c = 0.6$, (q) $x/c = 0.625$, (r) $x/c = 0.65$, (s) $x/c = 0.675$, (t) $x/c = 0.7$, (u) $x/c = 0.75$, (v) $x/c = 0.8$, (w) $x/c = 0.9$, (x) $x/c = 1$.

To compare the frequency of oscillation for different angle of attack of the present study, a comparison table is given below:

Table 4.2: Comparison of frequency of oscillation with different angle of attack for M_∞ = 0.77.

Angle of attack	Frequency of oscillation (Hz)
3°	19.04
4°	19.31
5°	20.45
6°	20.79
7°	21.55

From the above table it is evident that with increased angle of attack frequency of oscillation of the shock wave on the upper surface of airfoil is also increased due to the higher intensity of oscillation. This behavior signifies higher fatigue load on airfoil surface during buffeting at higher angle of attack.

4.6 Root Mean Square of Pressure Distribution

Due to the unsteady phenomena of static pressure from the pressure history curve of airfoil upper surface, it has become essential to find out highest pressure prone area along the airfoil. For proper calculation root mean square of pressure is an effective one. The unsteady root mean square of pressure (RMS) oscillations are evaluated to identify intensified pressure position from 2° to 7° pitching condition. *Prms* is calculated as

$$Prms = \sqrt{\sum_{i=1}^{n} \frac{\left(Pi - \bar{P}\right)^2}{n}}\ , \text{ where } \bar{P} = \sum_{i=1}^{n} \frac{Pi}{n}$$

according to Hasan et al. [60]. The value of *Prms* is non-dimensionalized and plotted along chordwise location of airfoil which is shown in figure 4.21.

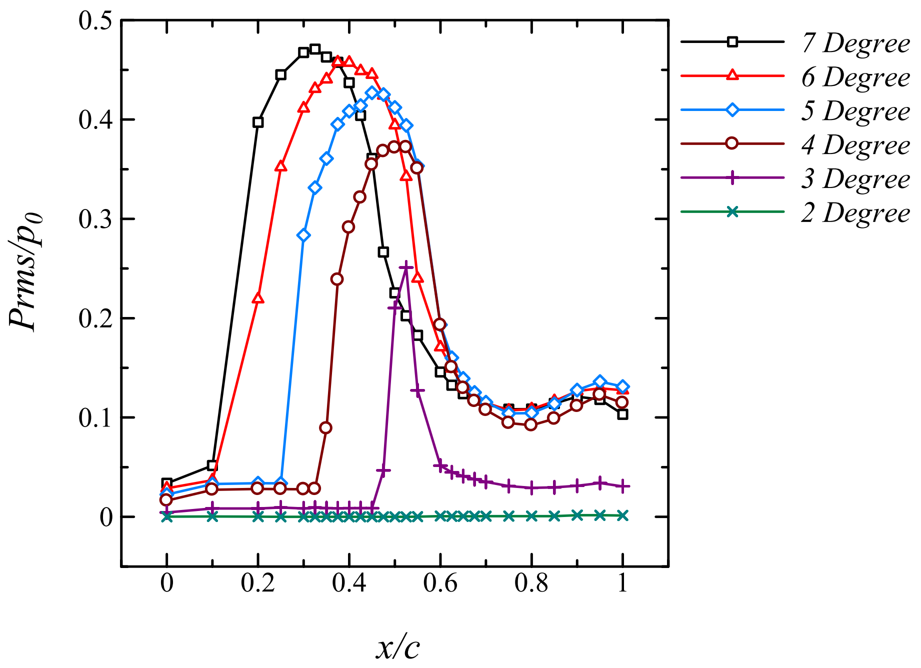

Figure 4.21: Non-dimensional root mean square of static pressure, $Prms/p_0$ distribution along the airfoil upper surface for different angles of attack and M_∞= 0.77.

As there is no shock oscillation for 2° of angle of attack, there is no *Prms* over the airfoil. It appears for 3° angle of attack from leading edge with a non dimensional constant value of 0.0085 upto 45% of chord position which indicates very low pressure oscillation around this region. After 45% of chord location there is sudden rise of $Prms/p_0$ having pick value of 0.251 at 52.5% chord location. This signifies large pressure fluctuation and intensity at this location. Further movement upto trailing edge shows sudden drop of $Prms/p_0$ at 60% chord location which decreases slowly ahead of 95% chord location. At 95% of chord location there is a tendency to sudden rise of $Prms/p_0$ is observed with a value of 0.034due to pressure fluctuation for the result of vortex formation at this separated flow region.

Further increase of angle of attack leads to forward movement of intensified position of airfoil along with the increment of $Prms/p_0$. For 4° angle of attack value of $Prms/p_0$ increases slowly upto 32.5% of airfoil with a value of 0.028. Behind this location $Prms/p_0$ value increases suddenly to 0.372 at 52.5% of chord position. This is the most pressure prone area for this case. With advancement upto trailing edge shows decrease of $Prms/p_0$ value ahead 95% of chord location. For this case also at 95% of chord location sudden rise of $Prms/p_0$ with a value of 0.123 is observed due to tendency of vortex formation which is not significant.

For 5° angle of attack a non dimensional value of *Prms* 0.033 is observed at 25% of chord position which indicates very low pressure oscillation around this region. After 25% of chord location there is sudden rise of $Prms/p_0$ having pick value of 0.427 at 45% chord location. This signifies large pressure fluctuation and intensity at this location. Further movement upto trailing edge shows sudden drop of $Prms/p_0$ at 62.5% chord location which decreases slowly ahead of 95% chord location. At 95% of chord location there is a tendency to sudden rise of $Prms/p_0$ is observed with a value of 0.136 due to pressure fluctuation for the result of vortex formation at this separated flow region.

Further increase of angle of attack leads to forward movement of intensified position of airfoil along with the increment of $Prms/p_0$. For 6° angle of attack value of $Prms/p_0$ increases slowly upto 10% of airfoil with a value of 0.037. Behind this location $Prms/p_0$ value increases suddenly to 0.457 at 37.5% of chord position. This is the most pressure prone area for this case. With advancement upto trailing edge shows decrease of $Prms/p_0$ value ahead 95% of chord location. For this case also at 95% of chord location sudden rise of $Prms/p_0$ having value of 0.129 is observed due to vortex formation.

For 7° angle of attack a non dimensional value of *Prms* 0.051 is observed at 10% of chord position which indicates low pressure oscillation at this region. After 10% of chord location there is sudden rise of $Prms/p_0$ having pick value of 0.47 at 32.5% chord location. This signifies large pressure fluctuation and intensity at this location. Further movement upto trailing edge shows sudden drop of $Prms/p_0$ at 60% chord location which decreases slowly ahead of 90% chord location. At 90% of chord location there is a tendency to sudden rise of $Prms/p_0$ is observed with a value of 0.118 due to pressure fluctuation for the result of vortex formation at this separated flow region.

At last we can draw at overview that for 3°, 4°, 5°, 6° and 7° angle of attack most shock intensified areas are located at 52.5%, 52.5%, 45%, 37.5% and 32.5% of chord length respectively which is significant parameter to control shock buffet.

4.7 Shock position

The non-dimensional static pressure distribution at different time instances along upper wall during one period is shown. Shock location is seen from the same figure where due to shock wave static pressure jump is observed. As no buffeting is observed for 2° angle of attack shock location is in a steady condition throughout time space. But for 3°, 4°, 5°, 6° and 7° angle of attack shock location moves periodically. During t = 0/10 T time step shock position is rear side of airfoil as time progress shock moves to forward side. At half time of the cycle shock location is most forward side and becomes weaker. Shock moves to rear side during the last half cycle.

4.7.1 Case : Angle of Attack 2°

For this case as no shock buffet is observed, shock wave occurs in a steady state condition throughout time progress. Shock location is observed at about 56% of chord location of airfoil (figure 4.22).

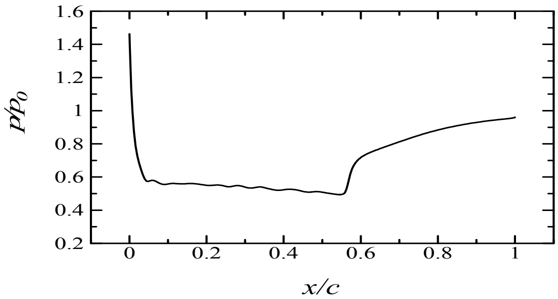

Figure 4.22: Shock wave location along the upper surface for $M_\infty = 0.77$, $\alpha = 2°$

4.7.2 Case : Angle of Attack 3°

From graph of non-dimensional static pressure distribution over chord (figure 4.23).it is found that from t = 0/10 T to t = 5/10 T time instances shock occurs at about 53.4%, 52%, 50%, 48%, 47% and 46.5% of chord length respectively. During the rest half cycle the shocks occur on the same chord length So, it can be concluded that the width of shock movement is limited to 46~54% of chord length.

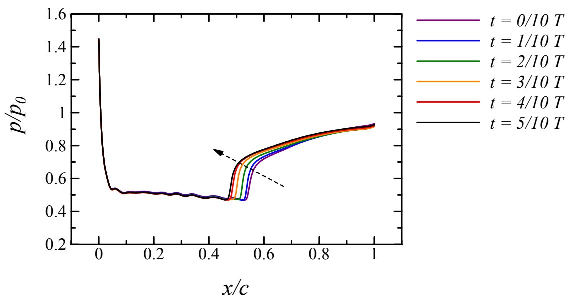

(a)

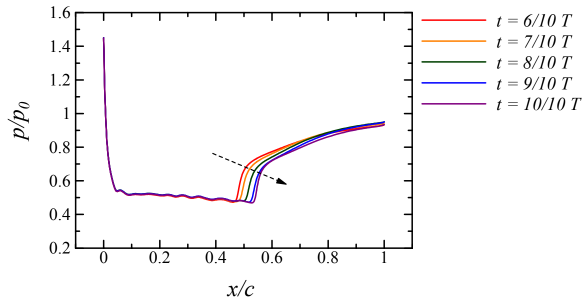

(b)

Figure 4.23: Unsteady shock wave movement during (a) 1st half cycle, (b) 2nd half cycle; of an oscillation along the upper surface for $M_\infty = 0.77$, $\alpha = 3°$

4.7.3 Case : Angle of Attack 4°

From the graph of non-dimensional static pressure distribution over chord shown in figure 4.24 it is observed that from t = 0/10 T to t = 5/10 T time instances shock occurs at about 57.8%, 53%, 46.4%, 40%, 35.8% and 34.2% of chord length respectively. During the rest half cycle the shocks occur on the same chord length. So, it can be concluded that the width of shock movement is limited to 34~58% of chord length. This shock movement zone is considered for control purpose of unsteady shock.

During 3° angle of attack this zone was limited to 46~54% of chord length. This data signifies that unsteady shock wave move forward or shock wave occurs early due to increased angle of attack.

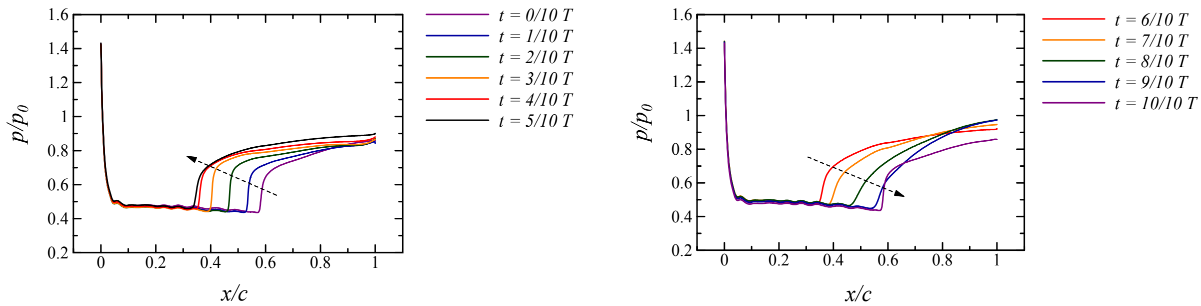

(a) (b)

Figure 4.24: Unsteady shock wave movement during (a) 1st half cycle, (b) 2nd half cycle; of an oscillation along the upper surface for the conditions M_∞= 0.77, α = 4°

4.7.4 Case : Angle of Attack 5°

From graph of non-dimensional static pressure distribution over chord (figure 4.25) it is found that from t = 0/10 T to t = 5/10 T time instances shock occurs at about 56.9%, 51.7%, 42.9%, 33.4%, 27.7% and 25.03% of chord length respectively. During the rest half cycle from t = 6/10 T to t = 10/10 T time instances shock appears 25%, 26.7%, 38.8%, 51.3% and 56.9% of chord length respectively. So, it can be concluded that the width of shock movement is limited to 25~57% of chord length.

For 4° angle of attack it was limited to 34~58% of chord length. This behavior also signifies that shock occurs early position prior to 4° angle of attack and shock oscillation region also expands.

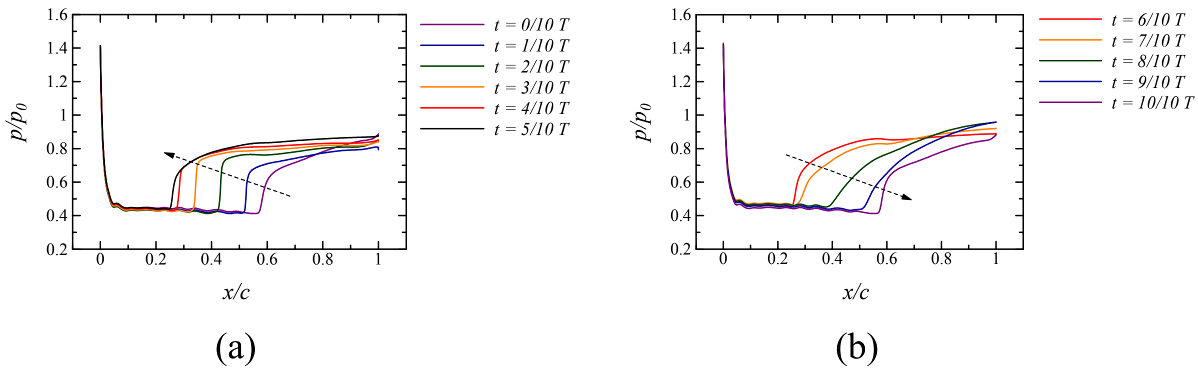

Figure 4.25: Unsteady shock wave movement during (a) 1st half cycle, (b) 2nd half cycle; of an oscillation along the upper surface for the conditions $M_\infty = 0.77$, $\alpha = 5°$

4.7.5 Case : Angle of Attack 6°

From graph of non-dimensional static pressure distribution over chord (figure 4.26) it is found that from t = 0/10 T to t = 5/10 T time instances shock occurs at about 53%, 49.5%, 39.5%, 29.2%, 21.4% and 18.4% of chord length respectively. During the rest half cycle the shocks occur on the same chord length. So, it can be concluded that the width of shock movement is limited to 34~58% of chord length. The width of shock movement is limited to 18~53% of chord length.

For 5° angle of attack it was limited to 25~57% of chord length. This phenomenon of 6° angle of attack also signifies the similar behavior that shock occurs early position prior to 5° angle of attack. Also shock oscillation region for this case is wider than 5° angle of attack.

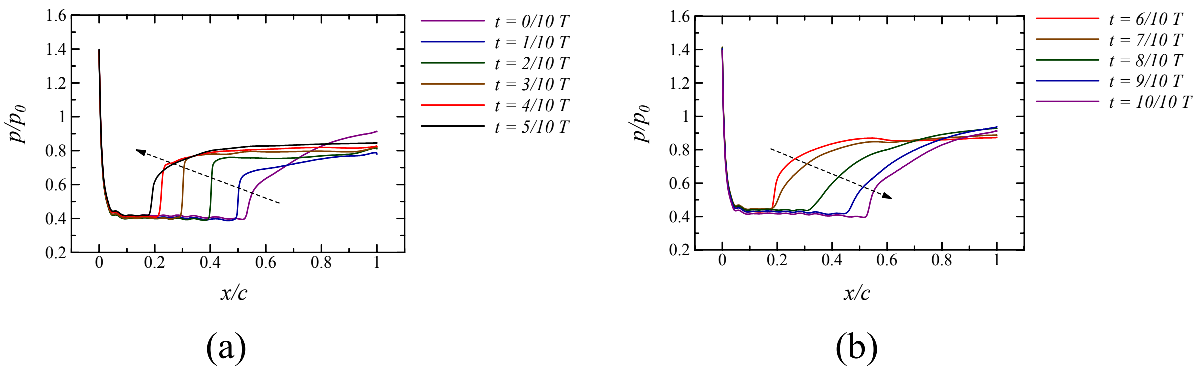

Figure 4.26: Unsteady shock wave movement during (a) 1st half cycle, (b) 2nd half cycle; of an oscillation along the upper surface for the conditions $M_\infty = 0.77$, $\alpha = 6°$

4.7.6 Case : Angle of Attack 7°

From graph of non-dimensional static pressure distribution over chord (figure 4.27) it is found that from t = 0/10 T to t = 5/10 T time instances shock occurs at about 41.8%, 33.9%, 24.3%, 16%, 12.2% and 10% of chord length respectively. During the rest half cycle from t = 6/10 T to t = 10/10 T time instances shock appears 12.2%, 26.7%, 38.1%, 45.1% and 42.5% of chord length respectively. So, it can be concluded that the width of shock movement is limited t 10~46% of chord length.

For 6° angle of attack it was limited to 18~53% of chord length. This behavior of 7° angle of attack also signifies that shock occurs early position prior to 6° angle of attack.

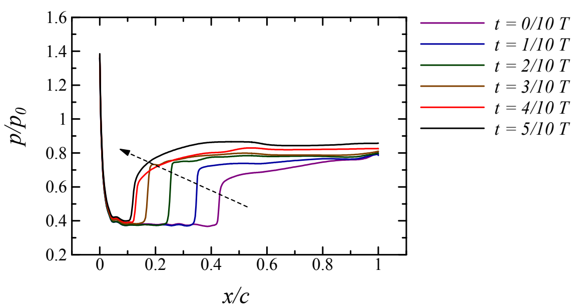

(a)

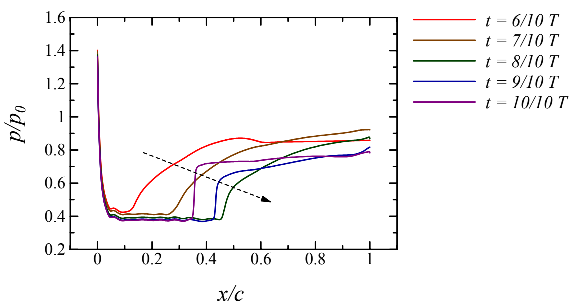

(b)

Figure 4.27: Unsteady shock wave movement during (a) 1st half cycle, (b) 2nd half cycle; of an oscillation along the upper surface for the conditions M_∞= 0.77, α = 7°

4.8 Shock control with bump

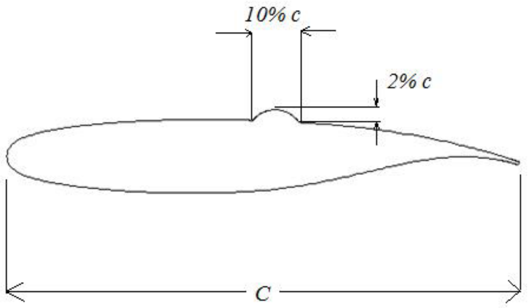

Figure 4.28: Bump geometry and shape on airfoil.

In order to control shock buffet a passive control technique 'Shock Control Bump' is drawn in a preprocessing tool and observed the aerodynamic behavior on airfoil numerically. The bump shape is like 'semi-circular' whose height is 2% of airfoil chord and length is 10% of airfoil chord (figure 4.28). Bump location was placed in such a way that its peak point is located on that location where non-dimensional root mean square of pressure value is highest. Following table 4.2 shows the bump location on airfoil for different angle of attack.

Table 4.3: Location and width of bump with different angle of attack for M_∞= 0.77

Angle of attack	Forward location of bump in (%) of chord	Rearward location of bump in (%) of chord	Length of bump in (%) of chord
3°	48	58	10
4°	48	58	10
5°	40	50	10
6°	35	45	10
7°	27	37	10

4.8.1 Mach contour

To control shock buffet over supercritical airfoil bump is introduced and observed its effectiveness. For same free stream Mach number and different angle of attack bump was positioned at different location of airfoil by investigating mean shock wave position and shock wave movement. Though bump shape and size has different affectivity on controlling shock buffet, bump with similar shape and size was used to compare the shock control behavior by moving there position according to shock intensity with different angle of attack.

To control shock buffet for $M_\infty = 0.77$ and $\alpha = 3°$ a semi circular bump is created at 48-57% of chord length over the airfoil as mean shock location was found at 52.5% of chord length and shock movement was identified on 46-54% of chord length. By fixing same solving parameters as that was fixed in without bump condition its shock behavior was numerically analyzed. At this case no shock buffet was observed (figure 4.29). From Mach contour with bump over the airfoil normal shock wave is observed twice. One for airfoil itself where 1.24 local Mach number is reached and another one over the bump where local Mach number 1.16 is reached which acts as small airfoil surface itself. Without bump condition maximum local Mach number was 1.45. So, it can be concluded that for 3° shock induced oscillation was controlled and local Mach number was also reduced by introducing bump.

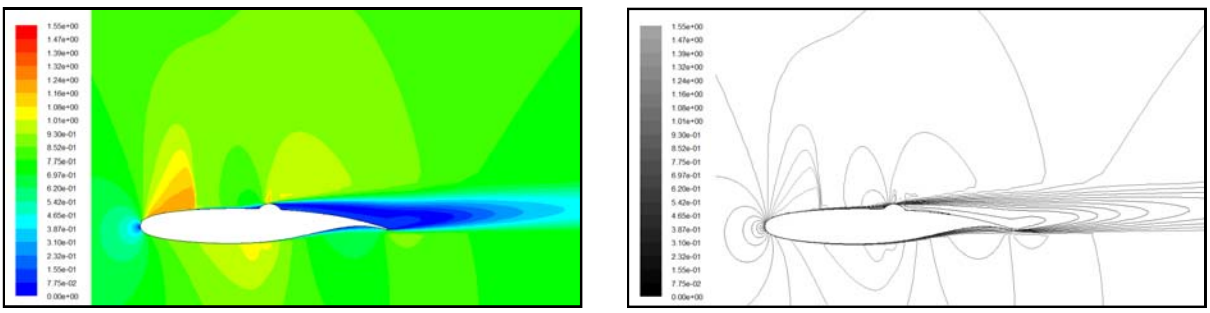

Figure 4.29: Contours of Mach number with bump for $M_\infty = 0.77$, $\alpha = 3°$.

To control shock buffet for 4° angle of attack with similar bump shape and size positioned at 48-57% chord length as mean shock was found at 52.5% of chord length and shock movement was limited to 34~58%. At this case Lamda type shock was observed with maximum local Mach number1.39 is reached in front of shock and shock became steady (figure 4.30). Another small shock with maximum local Mach number 1.16 is observed. At this case shock induced flow separation is observed. Without bump maximum local Mach number was between 1.42 to 1.50. For this case also shock was controlled and maximum local Mach number was reduced by introducing bump.

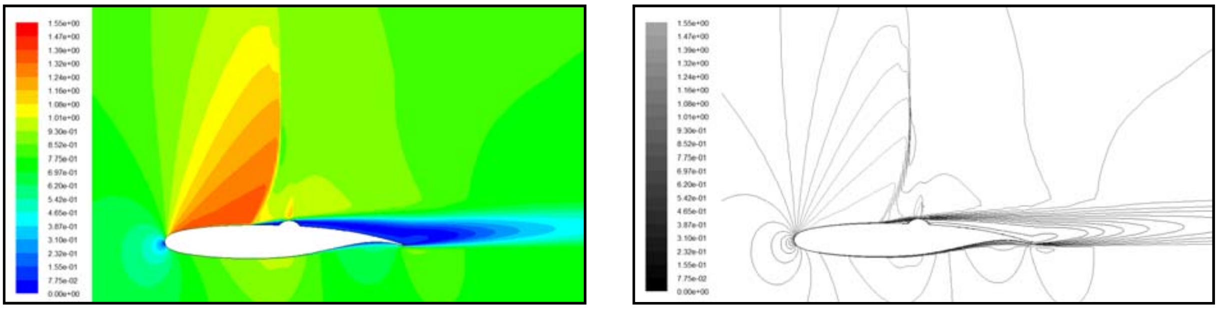

Figure 4.30: Contours of Mach number with bump for $M_\infty = 0.77$, $\alpha = 4°$.

During 5° angle of attack similar bump was positioned 40-50% of chord length as mean shock was calculated at 45% of chord length and shock movement was limited to 25~57% of chord length. For this case normal shock became steady with maximum local Mach number 1.32 (figure 4.31). Another normal shock with maximum local Mach number1.24 is observed around bump. During unsteady condition without bump maximum local Mach number was between 1.42 to 1.50. Shock induced flow separation is found downstream of shock.

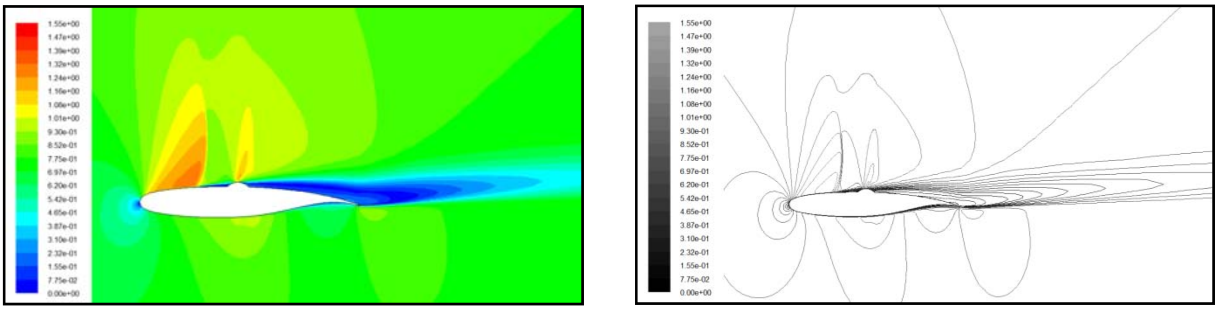

Figure 4.31: Contours of Mach number with bump for $M_\infty = 0.77$, $\alpha = 5°$.

For 6° angle of attack with similar bump Mach contour is observed in figure 4.32. At this case bump was positioned at 35-45% of chord length as mean shock was found at 37.5% of chord length with shock oscillation range of 18~53% of chord length. After numerically computation normal shock with no buffeting was observed. Maximum local Mach number reached to 1.47 and another shock with 1.24 Mach number was observed around bump. This small shock wave has a significant interaction with main shock wave. For unsteady condition it was between Mach number1.47 to 1.55. At this case, though the shock was controlled by introducing bump maximum local Mach number could not be reduced. Shock induced flow separation is observed here.

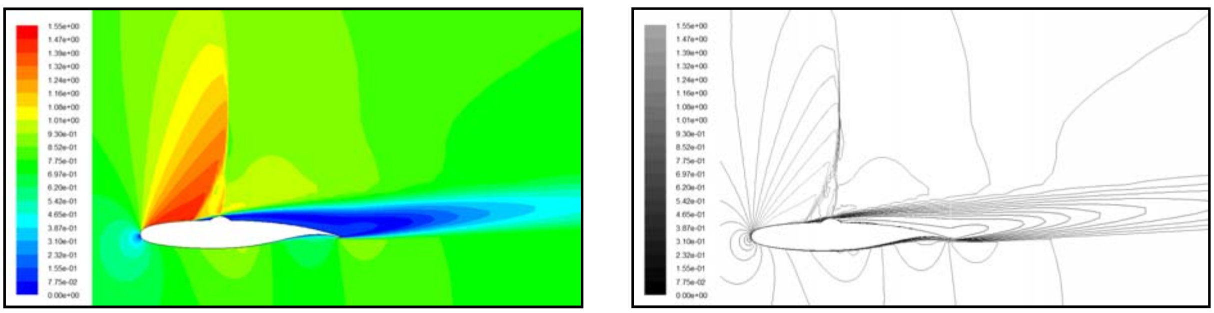

Figure 4.32: Contours of Mach number with bump for $M_\infty = 0.77$, $\alpha = 6°$.

At 7° angle of attack with bump of same size and shape the Mach contour is observed in figure 4.33. Bump was positioned at 27-38% of chord as mean shock was found at 32.5% of chord length and shock movement was between 10~46% of chord length. After numerical analysis steady shock was found with maximum local Mach number 1.55 and another normal shock wave with 1.24 maximum local Mach number around bump. During buffeting this was between 152-1.60. So, the shock oscillation is controlled with bump but no help to reduce maximum local Mach number. Shock induced flow separation is observed at this case.

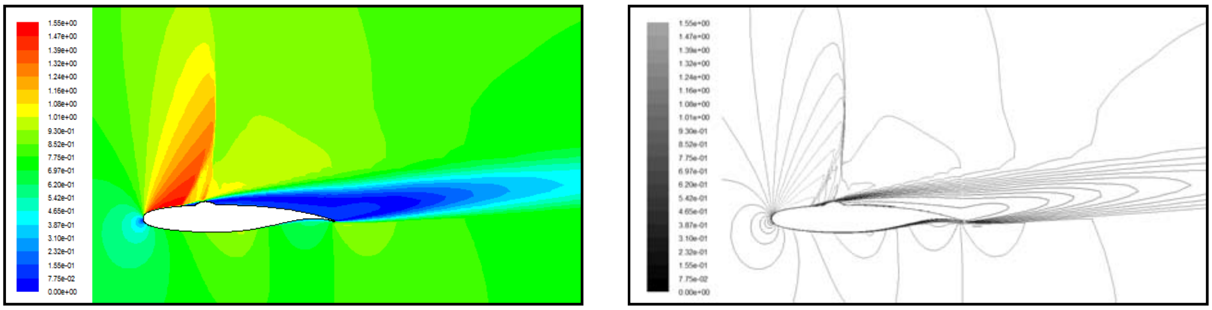

Figure 4.33: Contours of Mach number with bump for $M_{\infty} = 0.77$, $\alpha = 7°$.

From the above situations and figures it is found that shock movement becomes stable due to the insertion of bump in shock movement region over airfoil surface. The flow physics regarding the stability of shock wave due to insertion of a bump is due to the pressure wave which is generated from the shock wave is hindered by the bump of airfoil during the oscillatory motion of shock wave.

4.8.2 Lift and drag coefficient

Figure 4.34 shows lift coefficients with bump on airfoil for 1*s* time period for different angle of attack. Steady lift coefficient is observed which indicates that the shock induced oscillation has been stopped for the exiting flow condition. Value of mean lift coefficients without bump for angle of attack 3° to 7° respectively were 0 778, 0.825, 0.857, 0.861 and 0.831which then reduced to 0.322, 0.709, 0.631, 0.778 and 0.785 for inserting bump. In all the cases value of lift coefficient becomes lower with bump insertion than without bump condition of airfoil. These values of lift coefficients are dependent on the bump position, size and dimension.

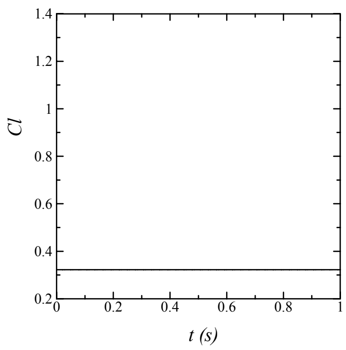

(a) $\alpha = 3°$

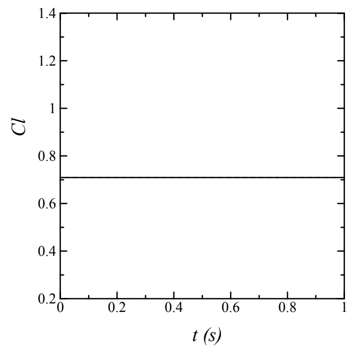

(b) $\alpha = 4°$

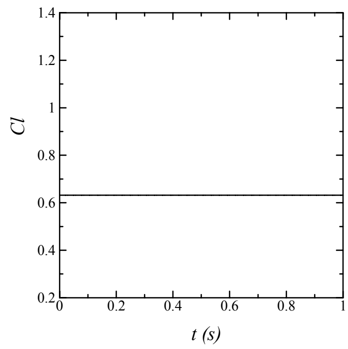

(c) $\alpha = 5°$

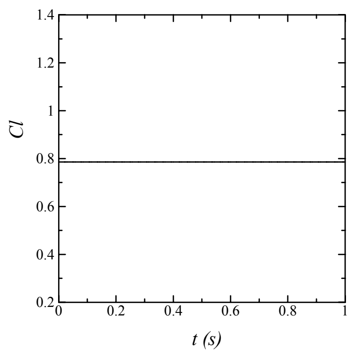

(d) $\alpha = 6°$

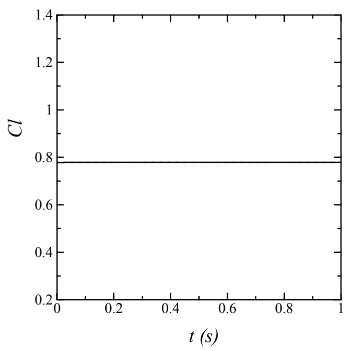

(e) $\alpha = 7°$.

Figure 4.34: Evolution of lift coefficient C_l with bump at $M_\infty = .77$; (a) $\alpha = 3°$, (b) $\alpha = 4°$, (c) $\alpha = 5°$, (d) $\alpha = 6°$, (e) $\alpha = 7°$.

Value of drag coefficient after inserting bump becomes steady (figure 4.35) with value of 0.066, 0.087, 0.124, 0.126 and 0.138 whose mean value were 0.065, 0.085, 0.103, 0.121 and 0.134 respectively without bump for 3°, 4°, 5°, 6° & 7° angle of attack respectively. This value is also dependent with bump position.

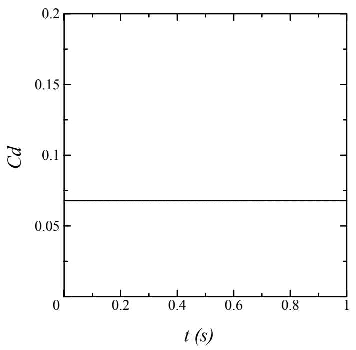

(a) $\alpha = 3°$

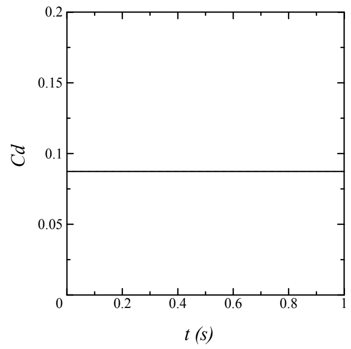

(b) $\alpha = 4°$

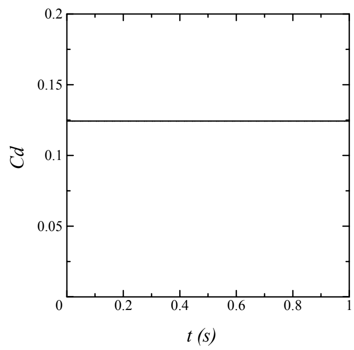

(c) $\alpha = 5°$,

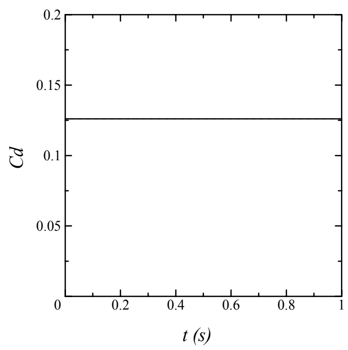

(d) $\alpha = 6°$

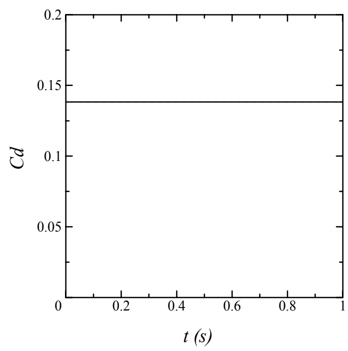

(e) $\alpha = 7°$.

Figure 4.35: Evolution of drag coefficient C_d with bump at $M_\infty = .77$; (a) $\alpha = 3°$, (b) $\alpha = 4°$, (c) $\alpha = 5°$, (d) $\alpha = 6°$, (e) $\alpha = 7°$.

To compare the lift coefficient and drag coefficient without bump and bump for different angle of attack of the present study, a comparison table is given below:

Table 4.4: Comparison of C_l and C_d without bump and with bump for different angle of attack at M_∞= 0.77.

	Without bump			With bump		
Angle of Attack	Mean C_l	Mean C_d	Mean C_l / Mean C_d	C_l	C_d	C_l / C_d
3°	0.778	0.065	11.850	0.322	0.066	4.754
4°	0.825	0.085	9.671	0.709	0.087	8.149
5°	0.857	0.103	8.275	0.631	0.124	5.082
6°	0.861	0.121	7.091	0.778	0.126	6.175
7°	0.831	0.134	6.179	0.785	0.138	5.688

From the table it is observed that ratio of lift to drag coefficient becomes lower with bump in comparison with airfoil without bump from 3° to 7° angle of attack. It is also observed that ratio of lift to drag coefficient value with bump condition is abrupt due to the use of same bump size irrespective of angles of attack and shock intensity.

4.8.3 Pressure coefficient

Maximum value of C_p along upper surface for 3°, 4°, 5°, 6° and 7° with bump condition are found -1.02, -1.28, -1.17, -1.42 and -1.47 respectively (figure 4.36).

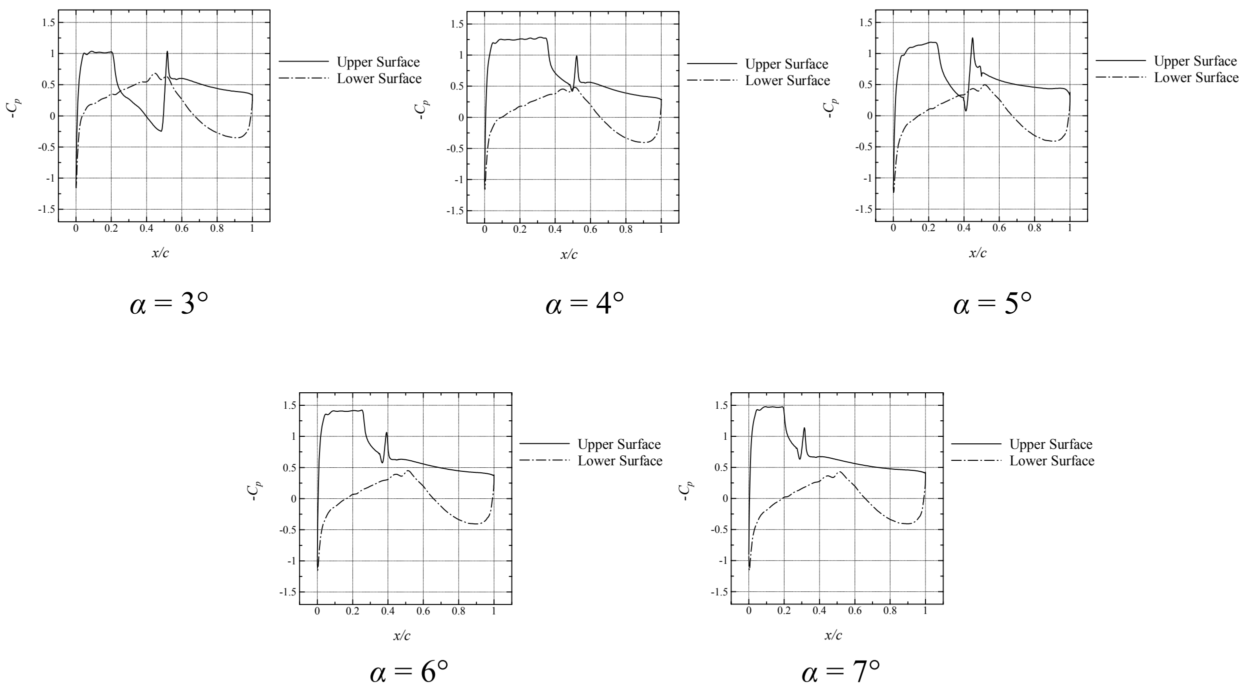

Figure 4.36: C_p distribution on upper and lower surface of airfoil with bump for $M_\infty = 0.77$, $\alpha = 3°$, $\alpha = 4°$, $\alpha = 5°$, $\alpha = 6°$and $\alpha = 7°$

4.8.4 Shock location

Shock wave location with bump on airfoil for different angle of attack is presented in figure 4.37. Shock location for 3°, 4°, 5°, 6° and 7° with bump condition are 20.4%, 35%, 24.3%, 25.5% and 19.4% respectively. Again, a small shock due to bump is observed around bump, continuous pressure rises up to shock wave and sudden pressure drop just behind the bump. This behavior of shock location can be controlled by proper bump shape and dimension according to shock behavior.

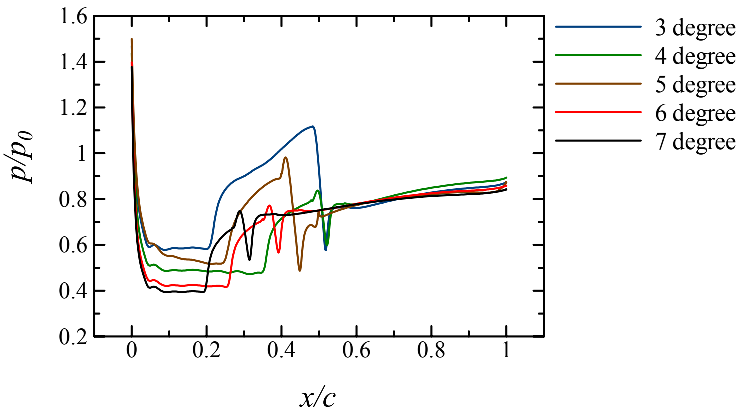

Figure 4.37: Steady shock wave location on upper surface of airfoil with bump for $M_\infty = 0.77$, $\alpha = 3°$, $\alpha = 4°$, $\alpha = 5°$, $\alpha = 6°$and $\alpha = 7°$

CHAPTER 5

CONCLUSION AND RECOMMENDATION

5.1 Conclusion

The present study has given some numerical observations regarding buffeting phenomena of NASA SC(2)-0714 supercritical airfoil from angle of attack 2° to 7° for Mach number 0.77.

- From observation of Mach contour it is found that at 2° angle of attack no buffeting occurs whereas buffeting commences from 3° angle of attack to 7°. During this buffet onset region shock induction becomes intense with gradual increment of angle of attack with higher local Mach number, lift & drag coefficient fluctuation and shock induced boundary layer separation This fluctuating higher local Mach number and shock creates fatigue thermal stress and fatigue load on aircraft structure.
- Also from mean lift to drag coefficient ratio it is evident that higher angle of attack during the buffet onset produces lower lift to drag coefficient which is a reverse phenomena of normal aerodynamic behavior on airfoil.
- Pressure history of airfoil upper surface point shows higher pressure variation around shock region. As the angle of attack is increased this fluctuation becomes higher with increased frequency of oscillation.
- Angle of attack increment also effects on the shock movement region which shows that higher angle of attack produces shock movement on a wider region.
- A passive means of buffet control device like bump was introduced at mean shock wave position of airfoil to control shock induced oscillation and numerically observed its effectiveness resulting steady shock for all angle of attack.

- With bump insertion, ratio of lift to drag coefficient becomes lower with bump in comparison with airfoil without bump from 3° to 7° angle of attack.

All of these observations from this paper contribute to design a supercritical airfoil with increased efficiency, higher speed and better structural & thermal strength.

5.2 Recommendation

Following recommendations are suggested for further work regarding similar topics:

- In order to get more effective results numerically with similar study, 3D computation can be done.
- The same computation can be done for various Mach number and angle of attack to study the aerodynamic behavior for that condition and control its effectiveness.
- The computation can be performed with more accurate turbulence model like large eddy simulations (LES) and direct numerical simulations (DNS) which is more effective than RANS based SST k-ω model.
- In this investigation it was not possible to identify the detrimental effect of shock load on aircraft structure as this computational process was limited only to fluid dynamics. Further improved computational method which can solve fluid dynamics and structural analysis can be applied to get physical behavior.
- Bump shape and size that was introduced can be changed to get more efficient aerodynamic behavior on airfoil.
- For effective control of buffet bump was introduced at different position at different angle of attack. To maintain higher speed at different angle of attack without buffeting a new mechanism may be invented where the bump will shift according to angle of attack.

REFERENCE

[1] Lee, B. H. K., "Self-sustained shock oscillations on airfoils at transonic speeds", *Progress in Aerospace Sciences*, 37 (2), 147-196, 2001.

[2] Becker, B., Reyer, M., Swoboda, M., "Steady and unsteady numerical investigation of transitional shock-boundary layer interaction on a fan blade", *Aerospace Science and Technology*, 11, 507-517, 2007.

[3] Lee, B. H. K., "Oscillatory Shock Motion Caused by Transonic Shock Boundary-Layer Interaction" *AIAA*, VOL. 28, NO. 5, 942-944, 1989.

[4] Patzold, M. "Numerical optimization of finite shock control bumps" *.AIAA,* 2006-1054, 2006.

[5] William Milholen II E Lewis R. "On the application of contour bumps for transonic drag reduction". *AIAA,* 2005-0462, 2005.

[6] Roos, F. W. and Riddle, D. R., "Measurements of Surface Pressure and Wake Flow Fluctuations in the Flowfield of a Whitcomb Supercritical Airfoil," NASA TN D-8443, Aug. 1977.

[7] Mabey, D. G., "Oscillatory Flows from Shock-Induced Separations on Biconvex Aerofoils of Varying Thickness in Ventilated Wind Tunnels," AGARD CP-296, Sept. 1980.

[8] Lee, B. H. K. and Ohman, L. H., "Unsteady Pressures and Forces During Transonic Buffeting of a Supercritical Airfoil," *Journal of Aircraft,* Vol. 21, June 1984, pp. 439-441.

[9] Seegmiller, H. L., Marvin, J. G., and Levy, L. L. Jr., "Steady and Unsteady Transonic Flow," *AIAA* Paper 78-160, Jan. 1978.

[10] Girodroux-Lavigne, P. and Le Balleur, J. C., "Unsteady Viscous-Inviscid Interaction Method and Computation of Buffeting Over Airfoils,'' Joint IMA/SMAI Conf. on Computational Methods in Aeronautical Fluid Dynamics, Univ. of Reading, MA, April 6-8, 1987.

[11] Gilan, M. A., "Navier-Stokes simulations of self-excited shock induced oscillations", *AIAA*-95-1809, June 1995

[12] Rumsey, C. L., Sanetrick, M. D., Biedron, R. T., Melson, N. D., Parlette, E. B. "Efficiency and accuracy of time-accurate turbulent Navier-Stokes computations, Proc. 13th *AIAA Applied Aerodynamics Conf.*, June 1995,pp. 1-5, Also *AIAA*-95-1835.

[13] McDevitt, J.B., Levy, L. L., and Deiwert, G. S., "Transonic flow about a thick

circular-arc airfoil," *AIAA Journal*, Col. 14, No. 5, 603-613, 1976.

[14] Singh, J. P., "Estimation of shock-induced buffet onset", *ACTA Mechanica*, 151, pp: 245-253, 2001.

[15] Kandula, M. and Wilcox, D. C. "An Examination of k-w Turbulence Model for Boundary Layers, Free Shear Layers and Separated Flows". *AIAA*-95-2317, June 1995.

[16] Velichko, S. A.; and Lifshitz, Yu. B. "Numerical Simulation of Viscous Transonic Flows Over an Airfoil. Theor. & Comput. Fluid Dyn", vol. 7, pp. 189-206, 1995.

[17] Harris, C. D. "Two-Dimensional Aerodynamic Characteristics of the NACA 0012 Airfoil in the Langley 8 Foot Transonic Pressure Tunnel". NASA TM-81927, 1981.

[18] Girodroux-Lavigne, P.; and Le Balleur, J. C. "Time-Consistent Computation of Transonic Buffet Over Airfoils". *ONERA* TP-1988-97, 1988.

[19] Edwards, John W. "Transonic Shock Oscillations Calculated With a New Interactive Boundary Layer Coupling Method" *AIAA*-93-0777, Jan. 1993.

[20] McDevitt, John B.; and Okuno, Arthur F. "Static and Dynamic Pressure Measurements on a NACA 0012 Airfoil in the Ames High Reynolds Number Facility". NASA TP-2485, 1985.

[21] Bartels, Robert E. "Interactive Boundary Layer Computations Using the Improved k-ω Turbulence Model. Numerical Methods in Laminar and Turbulent Flow", Volume 9, Part 1, C. Taylor and P.Durbetaki, eds., Pineridge Press, pp. 561-572, 1995

[22] Batina, John T. "Unsteady Transonic Small-Disturbance Theory Including Entropy and Vorticity Effects". J. Aircr. , vol. 26, pp. 531-538, June 1989

[23] Thiery, M., and Coustols, E., "Numerical Prediction of Shock Induced Oscillations Over a 2D Airfoil: Influence of Turbulence Modeling and Test Section Walls", *International Journal of Heat and Fluid Flow*, 27, 661-670, 2006.

[24] Alshabu, A., Hermes, V., Klioutchnikov, I., and Olivier, H., "Experimental and Numerical Investigation of Unsteady Transonic Airfoil Flow", *Notes on Numerical Fluid Mechanics and Multidisciplinary Design,* Vol. 109, pp. 137-151, 2010. DOI: 10.1007/978-3-642-04088-7_6.

[25] Xiao, Q., Tsai, H. M., and Liu, F., "Numerical Study of Transonic Buffet on a Supercritical Airfoil", *AIAA Journal*, Vol. 44, No. 3, PP. 620-628, 2006.

[26] Bartels, Robert E; and Edwards, John W. "Cryogenic Tunnel Pressure Measurements on a Supercritical Airfoil for Several Shock Buffet Conditions.

NASA TM-110272, 1997.

[27] Hirose, Naoki; and Miwa, Hitoshi: “Computational and Experimental Research on Buffet Phenomena of Transonic Airfoils” NAL-TR-996T, Sept. 1988.

[28] Deiwert, George S. “Finite Difference Simulation of Unsteady Interactive Flows. Computational Methods in Viscous Flows| Volume 3: Recent Advances in Numerical Methods in Fluids”, W. G. Habash, ed., Pineridge Press, 1984, pp. 281-308.

[29] Bartels, R. E., “Computation of Shock Buffet Onset for Conventional and Supercritical Airfoil,” *AIAA Paper* 97-0833, Jan. 1997.

[30] Rivers, M. B., and Wahls, R. A., “Comparison of Computational and Experimental Results for a Supercritical Airfoil” *NASA Technical Memorandum* 4601 November 1994

[31] Furlano, F., “Comportment des Mod´eles de Turbulence pour les ´ EcoulementsD´ecoll´es en Entr´ee de Tremblement,” Ph.D. Dissertation, Dept. of Fluid Mechanics, Ecole Nationale Sup´erieure de l’A´eronautique et de l’Espace, Toulouse, France, March 2001.

[32] Caruelle, B., “Simulations d’ ´ Ecoulements Instationnaires Turbulents an A´erodynamique: Application `a la Pr´ediction du Ph´enom`ene de Tremblement,” Ph.D. Dissertation, Dept. of Fluid Mechanics, Inst. National Polytechnique de Toulouse, Toulouse, France, Oct. 2000.

[33] Bartels, R. E., “Computation of Shock Buffet Onset for Conventional and Supercritical Airfoil,” *AIAA Paper* 97-0833, Jan. 1997.

[34] Brunet, V., “Computational Study of Buffet Phenomenon,” *AIAA Paper* 2003-3679, June 2003.

[35] Kotapati-Apparao, R. B., Squires, K. D., and Forsythe, J. R., “Prediction of the Flow over an Airfoil at Maximum Lift,” *AIAA Paper* 2004-0259, Jan. 2004.

[36] Fan, T. C., Xiao, J. R., Edwards, J. R., and Baurle, R. A., “Hybrid LES/RANS Simulation of a Shock Wave/Boundary Layer Interaction,” *AIAA Paper* 2002-0431, Jan. 2002.

[37] Deck, S., “Numerical Simulation of Transonic Buffet over a Supercritical Airfoil”, *AIAA journal* Vol. 43, No. 7, July 2005

[38] Stanewsky E. “Adaptive wing and flow control technology” *Progress in Aerospace Sciences* 37, 583–667, 2001.

[39] Stanewsky, E., Delery, J., de Matteis PP, Fulker, J., Doe, R.,EUROSHOCK II- “Drag reduction by shock and boundary layer control”, EUROSHOCK II Final Technical Report, TR BRPR-95-76/1, 1999, and Synthesis Report TR BRPR-95-76/2,1999 [to be published in Notes on Numerical Fluid Mechanics. Berlin:

Springer,2001]

[40] Greenblatt, D., Paschal, K. B., Yao, C. S., Harris, J., “Experimental Investigation of Separation Control Part 1: Baseline and steady suction”, *AIAA Journal*, 44, 2820-2830, 2006.

[41] Greenblatt, D., Paschal, K. B., Yao, C. S., Harris, J., “Experimental Investigation of Separation Control Part 2: Zero mass-flux oscillatory blowing”, *AIAA Journal*, 44, 2831-2839, 2006.

[42] Djayapertapa, L. and Allen, C. B. “Simulation of transonic flutter and active shockwave control International” Journal of Numerical Methods for Heat & Fluid Flow Vol. 14 No. 4, pp. 413-443, 2004

[43] Qin. N., Zhu. Y., Shaw. S.T. “Numerical study of active shock control for transonic aerodynamics International” *Journal of Numerical Methods for Heat & Fluid Flow* Vol. 14 No. 4, pp. 444-466, 2004.

[44] Li, J., Lee, c, H., Jia, L., Li, X., “Numerical study on flow control by micro-blowing”, 47th AIAA Aerospace Sciences Meeting Including the New Horizons Forum and Aerospace Exposition, Orlando, Florida, *AIAA paper* 2009-779, 2009.

[45] Qin, N., Wong, W.S., Moigne, A. L., “Three-dimensional contour bumps for transonic wing drag reduction”, *Proceedings of the Institution of Mechanical Engineers, IMechE-Part G: Journal of Aerospace Engineering,* 222, 619-629, 2008.

[46] Hasan, A.B.M. Toufique, Matsuo, S., Setoguchi, T., and Kim, H.-D., “Transonic Moist Air Flow around a Circular Arc Blade with Bump”, *Journal of Thermal Science*, 18, 325-331, 2009.

[47] Hasan, A.B.M. Toufique, Matsuo, S., Setoguchi, T., and Kim, H.-D., “Control of Transonic Flow with Non-equilibrium Condensation around a Circular Arc Blade using Bump”, *International Journal of Turbo and Jet Engines,* 26, 33-49,2009.

[48] Stanewsky, E., Delery, J. ,Fulker, L., Matteis, P. de.“Drag reductionby shock and boundary layer control”, in: Results of The Project EUROSHOCKII, in: Notes On Numerical Fluid Mechanics And Multidisciplinary Design, Springer, 80,2001.

[49] Stanewsky, E., “Adaptive wing and flow control technology”, *Progress in Aerospace Sciences,*37 583–667,2001.

[50] Smith, A.N., Babinsky, H., Dhanasekaran, P.C., Savill, A.M., Dawes, W.N. “Computational investigation of groove controlled shock wave/ boundary layer interaction”, in: 41st Aerospace Sciences Meeting & Exhibit, *AIAA*-2003-446 Paper, Reno, NV, 2003.

[51] Hanselka, H., Bein, Th., Breitbach, E. “An adaptive spoiler to control the transonic shock”, *Smart Material Structures* 9 141–148, 2000.

[52] Wagner, S., Wadehn, W., Fokin, D., Sommerer, A., Lutz, Th., Pritschow, G. “Structural concepts and aerodynamic design of shock control bump”, in ICAS Congress, Toronto, Canada, 2002.

[53] Holden, H., A., Smith, A., N., Babinsky, H. “Shock/ boundary layer interaction control using 3D bumps”, in: CEAS Aerospace Aerodynamics Research Conference, Cambridge, UK, 2002.

[54] Qin, N., Monet, D., Shaw, S.T. “3D bumps for transonic wing shock control and drag reduction”, in: CEAS Aerospace Aerodynamics Research Conference, Cambridge, UK, 2002.

[55] Rosemann, H., Richter, K., Birkemeyer, J et al. “Application of a 3d shock control bump on a transport aircraft configuration”. ONERA-DLR Congress, Toulouse, June, 2003

[56] Qin N., Zhu Y., and Ashill, PR., “CFD Study of Shock Control at Cranfield”, 2105.1-2105.9, *ICAS* 2000 congress

[57] Yun, T., PeiQing, L. & PeiHua, F. “Shock control bump parametric research on supercritical airfoil” SCIENCE CHINA Technological Sciences Vol.54 No.11: 2935–2944, November 2011

[58] Bartels, Robert E., and Edwards, John W., “Cryogenic Tunnel Pressure Measuremnts on a Supercritical Airfoil for Several Shock Buffer Conditions”, *NASA TM-110272,* 1997.

[59] Mundell ARG, Mabey DG. Pressure fluctuation caused by transonic shock/ boundary-layer interaction. *Aeronaut J,* Aug/Sept 1986; pp 274-281.

[60] Hasan, A.B.M. Toufique., Matsuo, S., Setoguchi, T., and Islam, A.K.M. Sadrul, “Effects of Condensing Moist Air on Shock Induced Oscillation around an Airfoil in Transonic Internal Flows”, *International Journal of Mechanical Sciences,* 1-11, 2011.